uOttawa

L'Université canadienne
Canada's university

FACULTÉ DES ÉTUDES SUPÉRIEURES ET POSTOCTORALES

uOttawa

L'Université canadienne
Canada's university

FACULTY OF GRADUATE AND POSDOCTORAL STUDIES

Kristian A. Ewen
AUTEUR DE LA THÈSE / AUTHOR OF THESIS

M.A.Sc. (Mechanical Engineering)
GRADE / DEGREE

Department of Mechanical Engineering
FACULTÉ, ÉCOLE, DÉPARTEMENT / FACULTY, SCHOOL, DEPARTMENT

Ductility in FRP Rods for Concrete Reinforcement by Interfacial Shearing

TITRE DE LA THÈSE / TITLE OF THESIS

M. Munro
DIRECTEUR (DIRECTRICE) DE LA THÈSE / THESIS SUPERVISOR

A. Fahim
CO-DIRECTEUR (CO-DIRECTRICE) DE LA THÈSE / THESIS CO-SUPERVISOR

EXAMINATEURS (EXAMINATRICES) DE LA THÈSE / THESIS EXAMINERS

N. Naguib

P. Straznicky

Gary W. Slater
LE DOYEN DE LA FACULTÉ DES ÉTUDES SUPÉRIEURES ET POSTDOCTORALES /
DEAN OF THE FACULTY OF GRADUATE AND POSTDOCORAL STUDIES

DUCTILITY IN **FRP** RODS FOR CONCRETE REINFORCEMENT BY INTERFACIAL SHEARING

Kristian A. J. Ewen

A Report submitted to the Faculty of Graduate and Postdoctoral Studies in partial fufillment of requirements for the degree of

MASTER OF APPLIED SCIENCE

Mechanical Engineering

Ottawa-Carleton Institute for Mechanical and Aerospace Engineering
Faculty of Engineering
University of Ottawa

Your file Votre référence
ISBN: 978-0-494-18492-9
Our file Notre référence
ISBN: 978-0-494-18492-9

Abstract

Non-corrosive reinforcement of concrete provides great potential for reducing life cycle costs (LCC) of highway infrastructure (bridge decks and columns, light-standards, dividers) and concrete structures near water (piers, retaining walls, platforms). This is especially important in areas where salts are common (cold weather road salting, coastal regions) and is achieved by extending the life of structures and the period between major repairs. Costs of infrastructure rehabilitation due to corrosion of reinforcement are estimated to be $1.2 billion dollars in Ontario in the next few years, and up to 40% of all annual infrastructure costs in the province of Quebec.

Efforts to reduce the frequency of repair and replacement of ageing structures include using epoxy coating of the reinforcing bar (rebar), cathodic protection, alternate types of steel and fibre reinforced polymer (FRP) rebar. Of these, FRP rebar appears to be the most promising. The limitation of FRP rebar is the low maximum strain and linear behaviour up to failure. Prior attempts at increasing the ductility and producing non-linear behaviour have had limited success. Maximum strain remains limited to that of the highest strain fibres available. Pseudo-ductility has been achieved by combining multiple fibre types having different material properties.

The work described in this thesis focussed on non-traditional methods for achieving ductility in FRP rebars by taking advantage of the frictional interface of two materials. Two methods were tested. The first employed a solid inner-core with an over-wrap cut at regular intervals and relied on the rebar pulling out of the concrete at sustained load. Rods were tested in concrete beams under bending loads. Sustained load was achieved for significant pull-out. The second method combined continuous fibres with discontinuous meso-rods wherein the continuous fibres provide initial stiffness and maximum strength and the discontinuous meso-rods provide high-ductility via fibre pull-out. A concept model using aligned short steel fibres was manufactured and tested. Load-displacement behaviour showed substantial local elongation. Prototype models using carbon fibres were manufactured and tested. Specimens showed evidence of fibre pull-out. Future specimens should employ an intermediate material with a controlled and repeatable shear strength for the interface.

Acknowledgements

The collaboration and support required towards the completion of this thesis was extensive. Appreciation for the roles they played in this pursuit belongs to the following:

To my primary advisor, Dr. Mike Munro, for the direction, guidance, enthusiasm, and optimism ; to my co-advisor, Dr. Atef Fahim, for always providing alternative viewpoints and making things interesting;

To Jason Carey: colleague, mentor and friend whom offered much advice (too often ignored) and assistance; and especially for introducing me to the other side of graduate studies - graduate community life with the GSAÉD - a far more fascinating and enriching experience than I had anticipated and one I will carry with me eternally.

To Dr. John Gardner and Majeed of the Civil Engineering Department for support and guidance with all things concrete.; to Leo Denner for endless assistance and instruction on all things electrical in nature; to the staff of the Mechanical Engineering machine shop: Brent Cotter, Arnie Loewen, & James for producing much of the equipment and specimens required for successful testing.

To Cagri Arayanci for being party to great successes and witness to failures (and for the magnitude of questions that helped me gain focus again!); Mark Deziel and Matt Bogues-Crowe for assistance with a variety of tasks, and to César de la Rosa for providing the information and original research from which this project grew.

To my companion and friend, Ann Fournier for being the first to hear about the frustrations and put it *all* into perspective, and for putting the smile back on my face when necessary.

To my family: my sister, Val for keeping me informed about the outside world and inspiring certain things in me, my father Beverly for encouragement.

Finally, thanks go especially to my mother, Janet (Mom!) for every type of support imaginable, surpassing that which was necessary by immeasurable degree. Thanks, Mom!

Table of Contents

List of Figures

List of Tables

Acronyms

FRP	Fibre Reinforced Polymer
AFRP	Aramid FRP
CFRP	Carbon FRP
GFRP	Glass FRP
LVDT	Linear Variable Displacement Transducer
ROM	Rule of mixtures
ACI	American Concrete Institute
ISS	Interfacial Shear Stress
RT	Room temperature
PTFE	Polytetrafluoroethylene
FHWA	Federal Highway Administration

Nomenclature

Symbol	*Definition*
V_f	Fibre volume fraction
V_m	Matrix volume fraction
E_C	Elastic tensile modulus of a composite
E_f	Elastic tensile modulus of a fibre
E_m	Elastic tensile modulus of a matrix
σ	Ultimate tensile strength of the composite
σ'_m	Tensile strength of the matrix at the fibre failure strain.
τ	Interfacial shear stress
l_c	Fibre critical length
l_e	Embedded length of fibre or rod
Δ	Displacement of embedded fibre or rod
ϕ	Fibre or rod diameter
η_l	Fibre efficiency in short-fibre composites
ρ_f	Mass density of fibres
Tex	Weight, in grams, per 1000m of a fibre tow
$X_{m-r/rebar}$	Contribution of property 'X' of meso-rods in rebar
$X_{f,m-r}$	Contribution of property 'X' of fibres within the meso-rods

Chapter 1: Introduction

Fibre reinforced polymers (FRPs) are being deployed in civil engineering infrastructure applications with increasing frequency as engineers become familiar and comfortable with the benefits, usage and limitations of these materials.

While FRPs have revolutionised the aerospace and automotive industries, primarily based on excellent specific strength (the strength per unit weight) and specific stiffness that reduce the cost of transportation, civil engineering applications have their own unique requirements including high resistance to harsh artificial and natural environments. The primary role of the engineer is to balance safety with economy; where infrastructure is concerned, this has meant the use of steel in the reinforcement of concrete bridges, roads, retaining walls and other structures in the form of reinforcing bars (rebars). Concrete is a brittle material and has very low tensile strength, thus requiring a complementary material with high tensile strength; steel has for years met this need. It is simple to produce, widely available, relatively inexpensive, easy to handle and highly ductile, but it is also highly susceptible to corrosion. Corrosion of steel rebars results in a decrease in tensile strength as well as a decrease in the shear bond between steel and concrete, thus reducing its efficacy as a complementary material for reinforcing.

Many approaches have been taken to protect rebars from exposure to the harsh conditions such as electrolytes (water plus de-icing or oceanic salts) and seasonal variations in precipitation and temperature. Low porosity concrete, epoxy coating of both the steel rebar and the concrete, and concrete additives such as fly-ash have been employed with limited success, but rough handling during installation and cyclic loading, among other factors, still lead to exposed reinforcement and the eventual infiltration of damaging alkalis. Where exposure to alkalis is unavoidable, other methods have been used, including alloy steels, discontinuous polymer fibres, and cathodic protection.

1.1 General problem definition

Corrosion of steel rebars in concrete is hazardous, visually unattractive, and costly. It is hazardous because of the loss of structural integrity as the reinforcement decays. It is visually unattractive as expansion of the reinforcement surface during corrosion causes spalling,

delamination, cracking and staining of the concrete. It is costly due to the degree of effort required to replace affected reinforcement, to the disruption of the use of the ailing structure and to the environmental cleanup required after rehabilitation. In one example, the Province of Quebec spends half of its very large annual maintenance budget on repair of bridges that have experienced deterioration due to steel corrosion [1]. In 2000, the United States Federal Highway Administration (FHWA) reported that over 170,000 of all steel and reinforced concrete bridges in the US were "structurally deficient or functionally obsolete" [2] mainly due to corrosion. Similarly, the National Research Council of Canada Institute for Research in Construction (NRC IRC) reported that nearly 40% of Canada's bridges are in a state of disrepair requiring rehabilitation or total replacement [3]. Razaqpur [4] estimates repair costs of $1.2 billion for bridges in the Province of Ontario over a period of less than five years. A long term solution is required to minimise costs without sacrificing safety.

1.2 Research approach

FRPs have the potential to replace steel in its entirety where appropriate. FRPs are susceptible to a small variety of physical and chemical degradation, e.g., moisture absorption, ultra violet light and alkalinity, however these have been proven easy to control.

The principal concern for the use of FRP reinforcement is the ductility (maximum permanent plastic deformation) of FRP rebar. While strong, stiff, lightweight and tough, FRP rebars are almost purely elastic. That is to say as the load is increased up to the point of failure, no permanent deformation occurs. A great deal of research has been undertaken to produce ductile, or pseudo-ductile FRP rebar with an elastic modulus and strength of steel, but with limited success. Some improvements have resulted from the mixing, or hybridization, of several types of fibres but the ductility remains limited to that of the maximum fibre ductility.

Because civil engineers are generally concerned with the macromechanical behaviour of materials, the micromechanical behaviours have not been explored for solutions to poor FRP rebar ductility. This research work aims to address the lack of ductility and characteristics of FRP rebars for concrete applications. The short term goal is to establish a group of viable solutions for approximating ductility in rebars by investigating different designs and design parameters. The long

term goal of the work is the use of the information gathered for the development of quality product suitable for use in the field. Sliding friction is investigated as a primary mechanism for approximating ductility. Two approaches have been specifically researched. The first approach is based on a model of continuous/discontinuous hybrid rod applying the concept of short-fibre pull-out. The second approach is based on the concept of the relative sliding of a solid inner core with respect to a discontinuous over-wrap using a controlled shear interface.

1.3 Thesis outline

In the following Chapter the rationale for the use of FRPs in construction based on durability and long term costs will be discussed. Examples of applications that would benefit from the use of FRP rebar, and several examples currently applying them are presented. Prior attempts at improving FRP rebar ductility will be discussed. Methods for developing ductility in other composites and how they may be applied to FRP rebar will be introduced and detailed. The results of tests by de la Rosa [5] were re-evaluated and the results of the re-evaluation are discussed in Chapter 3. An overview of short-fibre composite theory is then presented in Chapter 4. The theory and the re-evaluation of de la Rosa's results [5] are utilised to develop the two methods based on friction to achieve ductility and are described in Chapter 5. Design, manufacturing and testing of proof-of-concept models are then detailed.

Chapter 6 details the manufacturing and testing of concrete beams reinforced with one of two proposed methods for achieving pseudo-ductile FRP rods. A discussion of the merits of the two methods, including comparison of material and other properties, is provided in Chapter 7. A summary of the conclusions from each section is given in Chapter 8. Finally, several recommendations for further research and improvements on the product development are given in Chapter 9.

Chapter 2: Literature Review

2.1 Principle of reinforcement

The need for reinforcement of concrete stems from the low tensile strength of the material. Concrete is selected for use in construction for its low cost, availability, formability, and high compressive strength, typically 30-40 MPa for general use and approximately 90 MPa for high-strength concrete. This high compressive strength contrasts its low tensile strength – approximately 10% of the compressive strength. The most common solution to this deficiency is the use of steel rods embedded in the concrete in zones of tension. This practice is used to prevent transverse expansion of axially compressed structures (e.g., support columns) and on the underside of beams or slabs subject to bending loads (e.g., bridge decks, floors in general) to prevent catastrophic collapse.

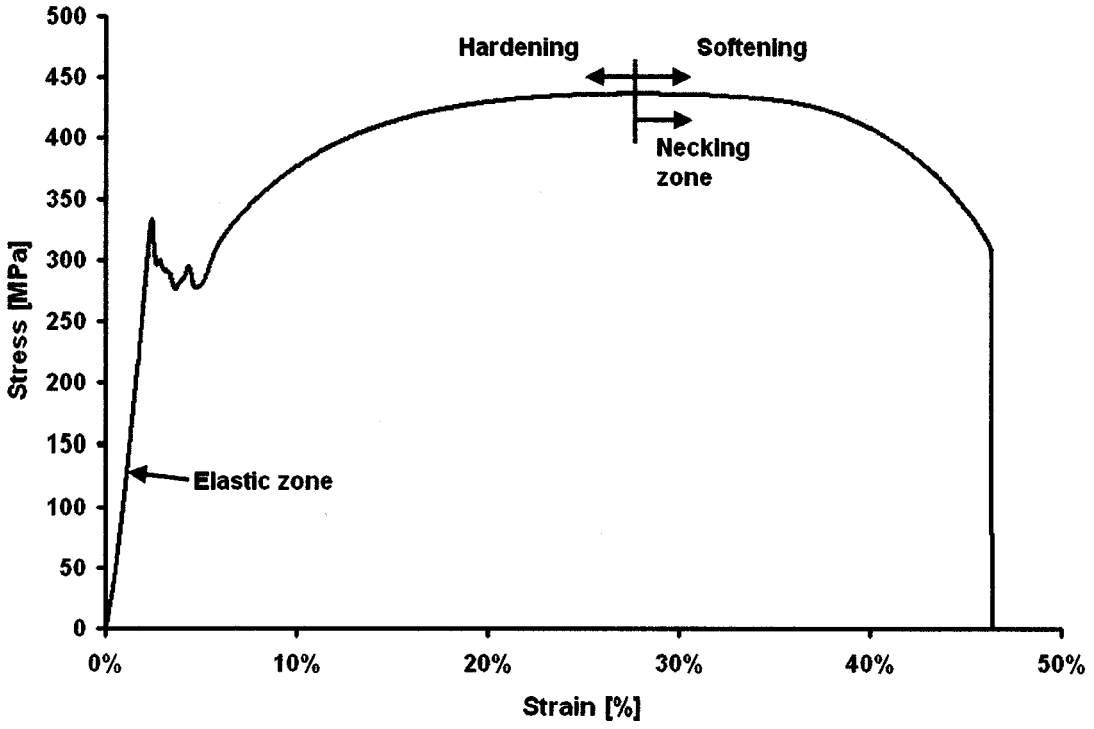

Figure 2.1: Typical stress-strain curve for a ductile, low-carbon steel.

Steel is favoured by civil engineers as the choice reinforcement material for many of the same reasons as concrete is chosen for foundation construction; namely cost, availability and formability. However, in contrast to the low tensile strength of concrete, steel may carry stresses of 400-600 MPa for regular steel and up to 1000 MPa for high strength steel without sustaining any permanent deformation. Furthermore, it can carry even higher loads as it elongates to approximately 18% of its original length [6]. These features are critical to large load-bearing structures; the high strength allows for small amounts of steel for reinforcement [7] for service loads, and the high elongation (ductility) produces a gradual failure under constant loading (Figures 2.1 & 2.2) providing ample warning of potentially catastrophic failure. The tensile behaviour of a given steel is also highly repeatable.

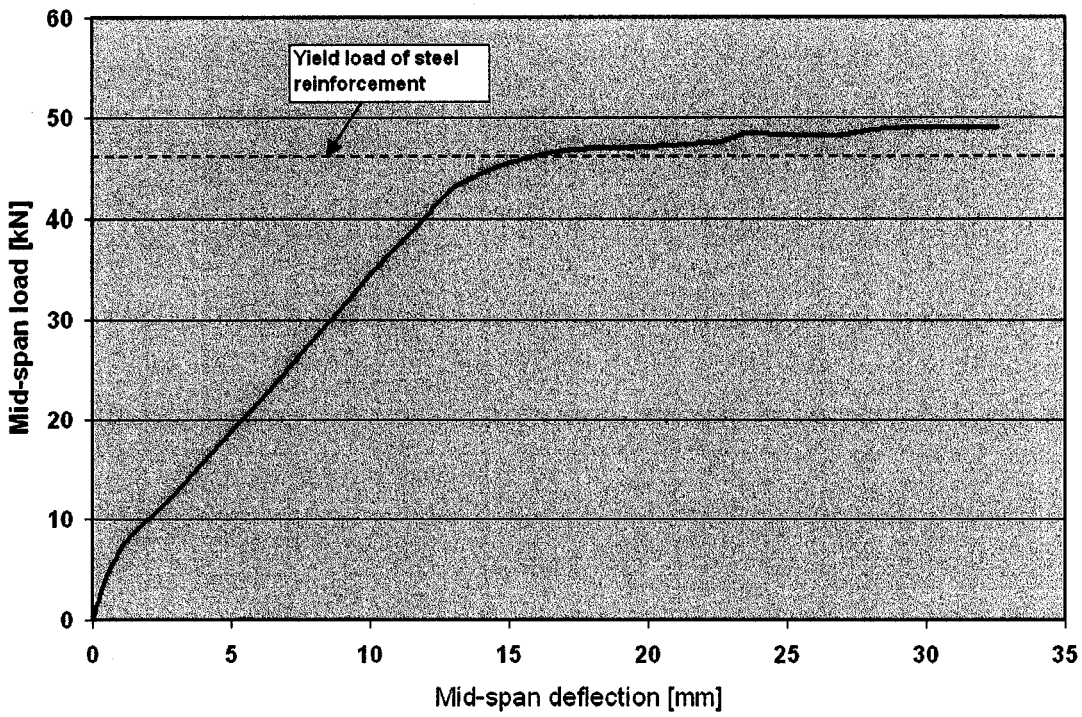

Figure 2.2: Load-deflection of a concrete beam reinforced with steel rebar. Adapted from [8].

Multiple modes of failure are possible in concrete structures under bending loads. Failure may occur by shear-compression (micro-cracking of the concrete), dowel splitting (cracking along tensile reinforcement), reinforcement bond failure (initiating pull-out) and large-scale shear failure,

among others [9]. These are illustrated in Figure 2.3 [9]. Shear failure, evidenced by long, diagonal cracks between supports, may be reduced by the addition of shear (web) reinforcement (known as stirrups) as illustrated in Figure 2.4. This results in a greater transfer of load to the flexural reinforcement. Dowel splitting in the concrete occurs coplanar with the reinforcement when loads are transferred transverse to the axis of the reinforcement.

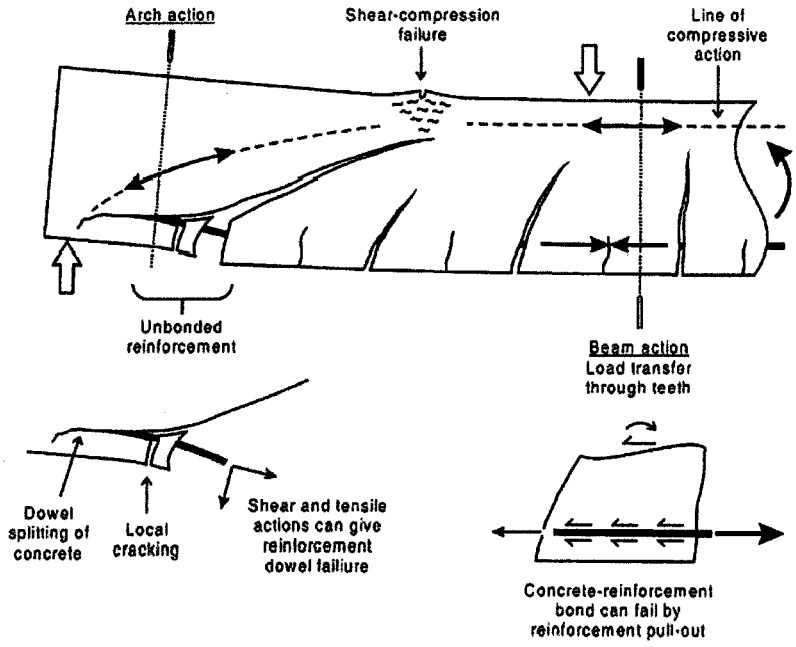

Figure 2.3: Failure modes in a concrete beam under bending loads [9].

The volume of reinforcement in structures is only about 1-2%, but provides a significant increase in load-bearing capability. However, when corrosion occurs over time the reinforcement is reduced considerably.

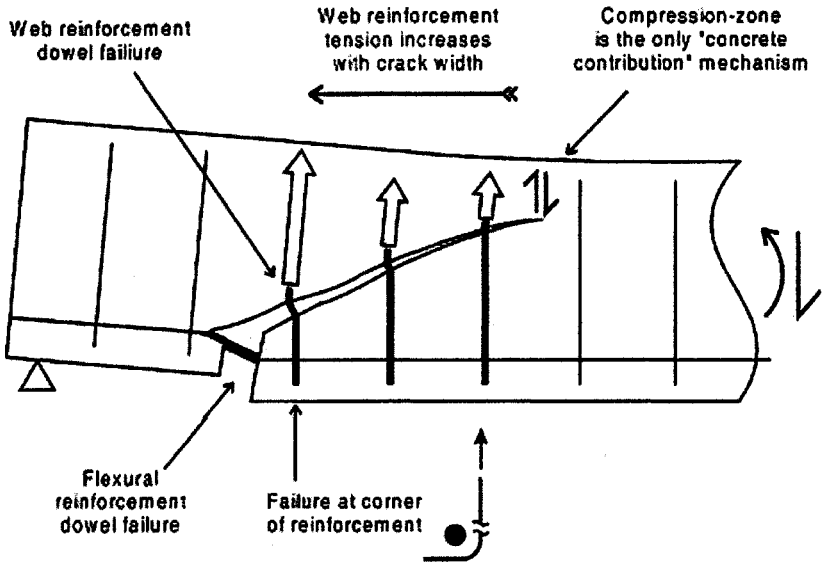

Figure 2.4: Concrete beam behaviour in the presence of shear resistant web reinforcement using dowels [9].

2.2 Corrosion of reinforcement

The problem of steel corrosion in concrete is highly visible in most aging infrastructure installations in North America and around the world. Evidence of the degree of the problem exists in buildings, bridges, piers, aqueducts, culverts, and even street curbs and light standards. The severity is notably higher in areas having harsh environments including costal regions and regions with extreme freeze-thaw cycles. An example of the latter is Ottawa, Ontario, Canada. With seasonal fluctuations in temperature of up to 70° C and daily fluctuations sometimes in the range of 20° C structures repeatedly undergo thermal expansion and contraction. This results in the rapid development of cracks in the concrete surface permitting the penetration of electrolytes (water containing alkalis, chlorides and other caustic materials) to the interior of the structure. The concentrations of these substances is increased by the application of road salt to driving surfaces as a means of deicing. As a result, steel reinforcement is quickly converted into a concentrated source of multiple microscopic galvanic cells. Ultimately, the reinforcement degrades completely or the concrete to reinforcement bond degrades to such an extent that the reinforcement is no longer effective. In many cases this occurs over a very short time – 3 - 10 years. Figures 2.5 through 2.8 illustrate several examples in the downtown area of Ottawa.

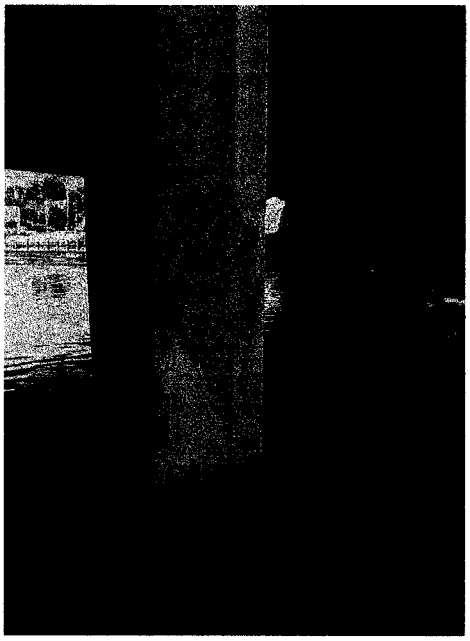

Figure 2.5: Bridge support column showing rust emerging from cracks and large areas of patch-work repair.

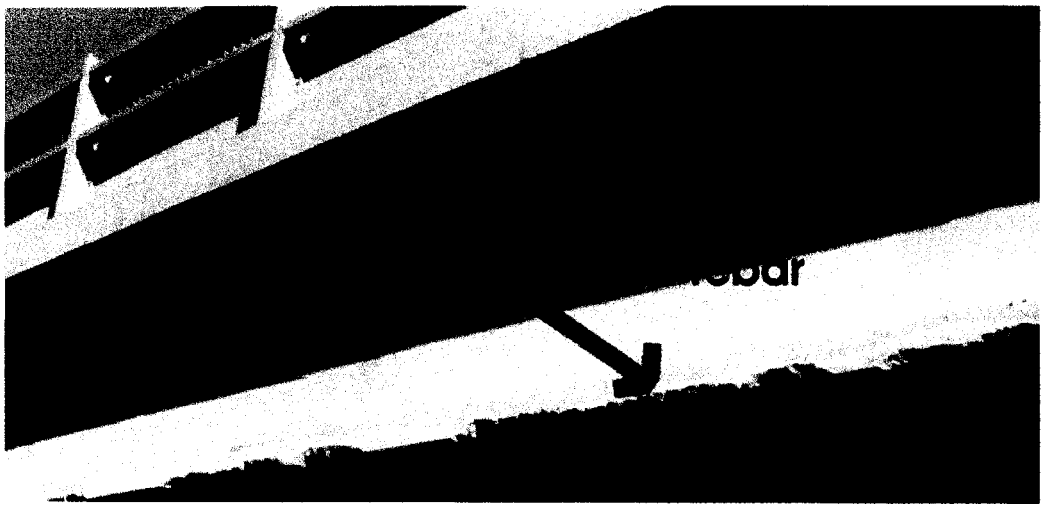

Figure 2.6: Exposed and corroded rebar in the Highway 417/Rideau Canal bridge deck, Ottawa, Ontario

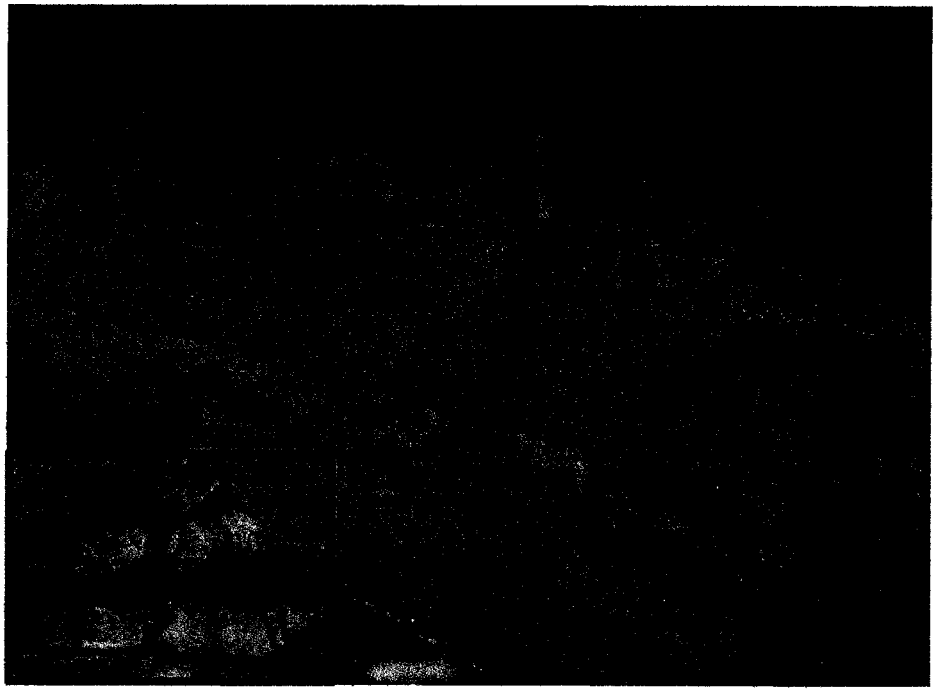

Figure 2.7: Concrete retaining wall showing exposed, corroded reinforcement and closeup (inset).

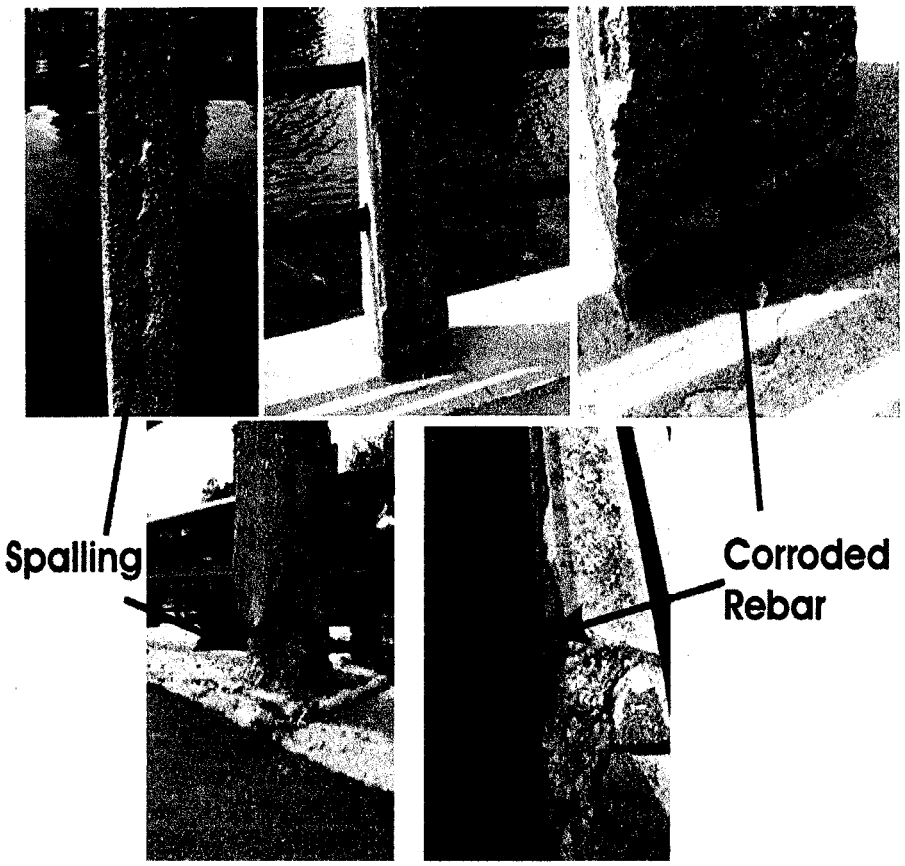

Figure 2.8: Damage progression and result of corroded steel rebar in rail supports along the Rideau Canal recreational pathway in Ottawa, Ontario. Similar damage of varying degree is observed in a majority of the supports (2003).

2.3 Methods of corrosion prevention

Despite its desirable traits, steel lacks sufficient resistance to chemical attack, thereby lowering the reliability of the reinforcement in corrosive environments. Several methods of protecting the reinforcement from the environment have been implemented.

One of the simplest and most frequently used methods of corrosion prevention is to coat the rebar with a protective coating, usually epoxy resin, which prevents the electrolyte from contacting the steel. This can be done during rebar manufacturing or onsite. Material handing and natural loading of the structure can chip or wear portions of the coating, exposing the steel to chemical attack even before the concrete is poured. Once initiated at these locations, corrosion progresses vigorously

at the exposed location as well as throughout the reinforcement.

Another method involves the use of cathodic protection, i.e., the use of a material that is more active (anodic) [10] connected to the reinforcement. The anodic material is connected to the structure to be protected via a simple circuit. In the presence of an electrolyte this more active anodic material, e.g., magnesium or zinc, corrodes instead of the steel, i.e., is sacrificed, and is replaced regularly for continued protection. The process is widely used with great success in the protection of buried pipelines and containers, and automotive wheel wells and body panels, but the complex grid of a typical reinforcement of the shear volume of steel in a large structure reduces its effectiveness.

Galvanic protection is similar to cathodic protection but with the anodic material (usually zinc) providing a full coat of the steel via a hot-dipping or spraying process [11].

A thin stainless steel cladding over typical rebar has been proposed to provide similar protection to full stainless steel bars, but at a significant cost reduction. Unfortunately, small manufacturing or handling defects were shown to result in extensive corrosion of the central reinforcing steel [12].

Various steel alloys such as stainless steel may be used in some situations but galvanic corrosion remains a concern, especially if a combination of structural and stainless steels are used. Gareth Thomas of MMFX Steel Corporation of America [13, 14] has developed a unique material for use in rebar. Known industrially as MMFX steel, the material is reported to be absent of galvanic micro-cells responsible for corrosion. Instead,

> "dislocated martensite laths ... are substantially free of twinning alternate with thin films of retained austenite"

achieved through controlled heating and tempering, thereby isolating galvanic pairs.

2.4 Fibre reinforced polymer composites

Fibre reinforced polymer [FRP] composites provide an excellent solution to many of the problems observed with other methods of corrosion prevention for a variety of applications. For example, FRP wheel wells and body panels in automobiles have been very successful in reducing roadside pollution created by crumbling, rusted parts, in addition to extending the life of the vehicles by many years. The combination of high-strength fibres with corrosion-resistant polymer matrices

virtually eliminates the need for additional protection.

Another advantage of FRP reinforcement is that the strength and stiffness may be tailored to specific situations depending on the ratio of fibre to matrix. The Rule of Mixtures [ROM] predicts the elastic modulus and ultimate tensile strength of a composite for the case of longitudinal tension:

$$E_C = E_f \cdot V_f + E_m \cdot (1 - V_f) \quad (a)$$
$$\sigma_C = \sigma_f \cdot V_f + \sigma'_m \cdot (1 - V_f) \quad (b) \qquad (2.1)$$

where subscripts c, f, and m represent composite, fibre and matrix respectively,

V_f = the fibre volume fraction,

E_C = the elastic tensile modulus of the constituent/composite

σ = the ultimate tensile strength of the constituent/composite

σ'_m = the tensile strength of the matrix at the fibre failure strain.

Manufacturing techniques allow for a practical limit of approximately 70% for fibre volume fraction for all fibre types. Figure 2.9 shows typical tensile stress-strain curves for the most common types of unidirectional FRPs - carbon (CFRP), glass (GFRP) and aramid (AFRP).

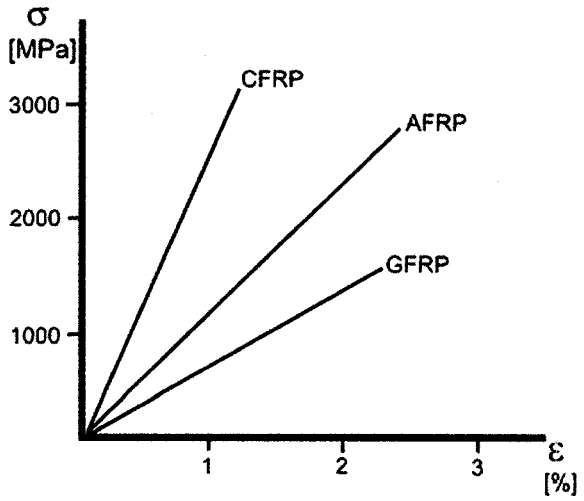

Figure 2.9: Mechanical properties of common FRP rebar materials.

The disadvantage of low ductility of FRP composites will be addressed later, but the advantages of replacing steel reinforcement with FRPs should be clear. One major concern, aside from the lack of ductility, is the relative cost of using FRPs in place of steel. Steel is widely available and generally inexpensive because of relatively simple and well established manufacturing processes. It is also recyclable. Reinforcing fibres and FRP rebars, on the other hand, require more involved manufacturing process and are considerably more expensive to produce. The initial costs should not be considered alone when comparing steel and FRP reinforcement. The life cycle cost (LCC) of any structure or other application, encompassing the initial material and labour costs, maintenance, repair and replacement, should play a major role in the choice of reinforcing material of the rebars.

2.5 Comparison of life cycle cost for steel and FRP bridges

The FHWA's Innovative Bridge Research and Construction Program (IBRC) and Intelligent Sensing for Innovative Structures Canada (ISIS Canada) are two of several North American agencies focussing on the development of structures employing advanced materials for civil engineering applications. While this includes special high strength stainless steels and other similar materials, the focus has been on various forms of FRPs. In 1998, the IBRC directed funding towards 84 FRP rebar development projects representing 11% of its funding (Figure 2.10) in conjunction with projects by each State's Department of Transportation. This represents a small amount of worldwide investment in alternative structural rehabilitation and replacement technologies versus total deck replacement and bonded reinforcement (the application of wide strips of FRP on the underside of decks and around columns).

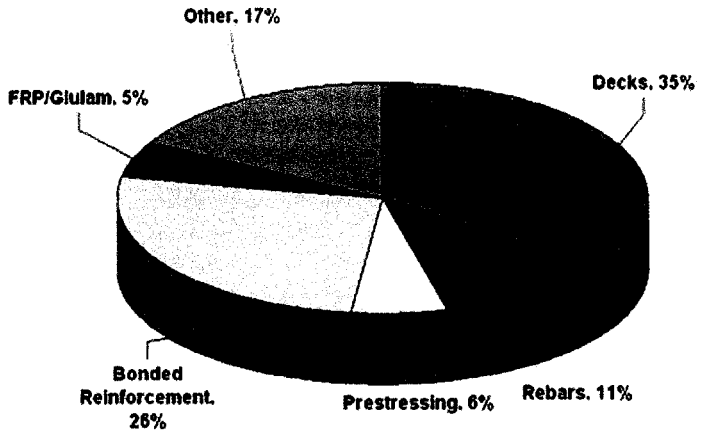

Figure 2.10: IBRC Funding allocation (1998) [adapted from 15]

The major driving force behind this investment and increased use of FRPs in construction is the LCC of the structure. Unfortunately, LCC predictions are not globally, or even regionally applicable. For example, the LCC of a bridge in Phoenix, AZ, USA will be significantly greater than the same design in Halifax, NS, Canada due to a higher degree of humidity, salinity and thermal cycles .

In contrast to the generally held belief that FRPs are more cost effective for building in the long term, Nystrom et al [2] conclude that the LCC of FRP materials in bridge construction is, and will remain, higher than that of traditional materials but their study is limited to bridges with spans less than 10 m in the state of Missouri where road salting is an infrequent process. Consideration is also not given to the cumulative effect of quicker installation times, that is, the shortened time for labour per bridge frees up manpower for other projects, nor to the reduced need for larger, more expensive heavy lifting equipment (due to lighter FRPs), both obvious and significant cost benefits. Additionally, the cost of maintenance repair is estimated at 1% of the initial construction cost - in strong contrast to the realities of larger structures. Considering this low proportion, a LCC savings of $\$88/m^2$ for FRP was projected versus a $\$222/m^2$ initial premium as compared to using steel rebars [2].

Conversely, an Ottawa Hydro study [16] found that for even smaller applications such as

light standard reinforcement, FRP materials outperform traditional materials (wood and steel-reinforced concrete) in LCC by several times. Additionally, the ideal failure mode (shear at the base) under vehicle impact is achieved with FRP reinforcement.

In addition, Nathan and Onyemelukwe [17] presented three separate LCC analyses for a bridge deck in Ft. Lauderdale Florida. Notable results of the study include a 45% higher rehabilitation cost for steel versus FRP bridges, a 7% higher replacement cost and a 58% higher repair cost.

Most strikingly, the *actual* first-cost of Sierrita de la Cruz Creek bridge in Texas, USA partially reinforced with GFRP, and designed by Timothy E. Bradberry, PE was found to be only 1.5% higher than had it been constructed solely with epoxy coated steel rebar. Had the entire bridge mat been reinforced with GFRP, the first cost "would have been 6.4%" higher than with epoxy coated steel [18]. This is significant as the Department of Transportation of Indiana found bridge deck replacement is commonly required every 45 years with major maintenance requirements in half that time [19].

In a complementary example of the longer service life of FRPs in construction, Busel [20] reports a high degree of success for GFRP dowel bars (Figure 2.4) placed in concrete highway contraction joints (Interstate-77 and Ohio State Route 7). After 15 years under actual service conditions the only degradation of the GFRP dowel bars was due to mechanical wear; the tensile and shear strengths were unaffected as was the stiffness. Epoxy coated steel dowel bars under identical conditions showed extensive corrosion damage and delamination of the epoxy coating.

The aesthetic and environmental benefits are not quantifiable from a financial perspective but are nonetheless an important consideration in material selection. Prior to 1998, [21], fewer than 80 bridges worldwide were constructed using FRP reinforcement. In the past five years, the applications have increased dramatically, beginning with small research driven applications. This trend will continue towards standard use. Two examples of GFRP reinforced bridge decks are shown in Figure 2.11.

2.6 Survey of FRP rebar research

Several areas of research have been active with regards to various properties and the behaviour of FRP rebar. The majority of the work has been in concrete rebar bonding. The durability of the FRP reinforcing bars and the fibres used to form them has been the subject of some research. More recently, research has been undertaken in the active (real time) monitoring of structures reinforced with FRPs. Each field will be briefly presented. Finally, efforts to produce pseudo-ductility in the reinforcing bars which has been of interest to many researchers will be discussed in detail in Section 2.8.

(a) 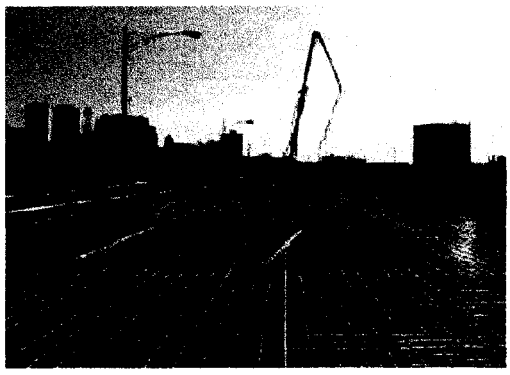 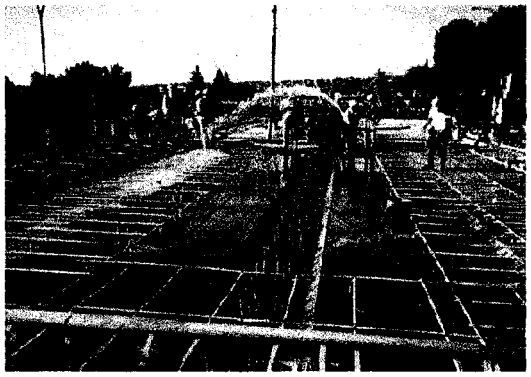 (b)

Figure 2.11: 1999 Redecking of Dayton, Ohio's Salem Avenue bridge (left) and 1997 construction of Calgary, Alberta's Crowchild bridge (right) both with GFRP reinforcing members. [22]

2.6.1 Concrete-rebar bond strength

Pultrusion is the typical method of manufacture for FRP rebar as it is a fully continuous process and is ideal for long products having a non-varying cross-section. The continuous cross-section causes problems with anchoring to concrete; the frictional interface between pultruded rod, having a glass-like surface, and concrete is low. Several means of increasing the anchoring by modifying the rebar surface have been developed with good results. Figure 2.12 shows several types of surface deformation achieved by: wrapping a fibre tow around the surface (a), moulded deformation (b), (e) and (f), 3D braiding (c), twisting of strands (d), and coating with sand (g). A glass coated CFRP rebar and typical ribbed steel rebar are shown in Figure 2.13.

(a) (b) (c) (d) (e) (f) (g)

Figure 2.12: Types of surface deformation on FRP rebar for improvement of bond to concrete: (a) spiral indentation; (b) deformed; (c) braided rod; (d) multiple twisted strands; (e) deformed; (f) helically indented; (g) sand coated. [5]

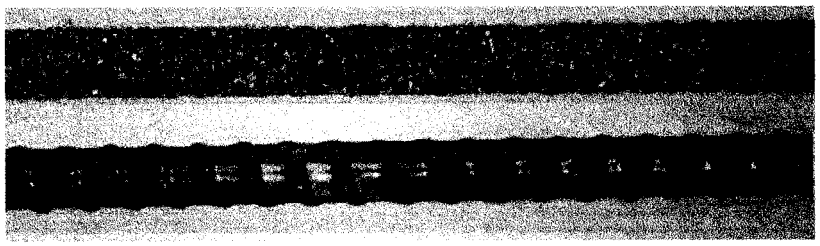

Figure 2.13: Glass coated CFRP (top) and typical ribbed steel rebar [23]

The FRP-to-concrete bond strength varies considerably between types of manufacture as would be expected, but also within each class. Wang, Goto and Joh [24] determined typical bond strength of 14-20 MPa for a variety of rebars. Benmokrane et al [25] report bond strengths of 13.6 and 14.4 MPa for embedded lengths of 200 and 100 mm, respectively, for CFRP rebar; for AFRP rebar, the bond strengths ranged from 4.4 to 13.2 MPa for embedded lengths of 350 and 100 mm, respectively. It is also shown in [25] that the concrete mixture has an effect on the bond strength. Figure 2.14 shows concrete-FRP rebar pull-out curves for sand coated aramid FRP rods (a) and helically-indented pitch-based carbon FRP rods. The load was measured at the loaded end (anchored end proximal to gauge length) and the free end (anchored end distal to gauge length). The maximum pull-out load differs considerably between the surface finishes. The average bond force during the pull-out portion is slightly greater than 8 kN for both types, but the variation is significantly different. This figure suggests that sand-coated coating of the surface provides a more controllable interface than does surface deformation. This is most likely due to the smaller size of interference to slip. It is possible then, that reducing the size of particles would further reduce the variation.

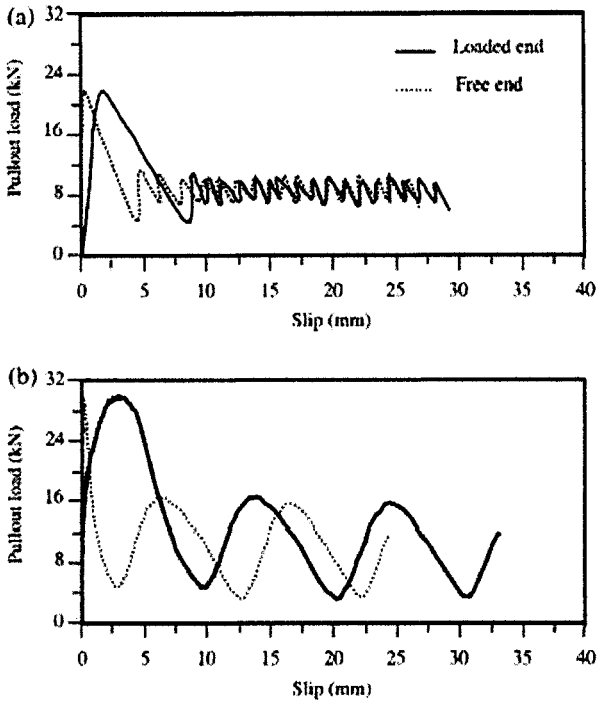

Figure 2.14: Rebar pull-out curves for (a) sand-coated AFRP and (b) helically deformed CFRP embedded in concrete[26].

2.6.2 Durability of reinforcing fibres and FRP Rebar

The driving force behind the implementation of FRPs as a replacement for structural steel is mainly the anti-corrosive behaviour, but FRP rebars do experience other forms of degradation and their durability is of concern in some applications. The changes in performance of unimpregnated fibres and FRP rebar are presented here.

2.6.2.1 Fibre durability

Studies have shown that unimpregnated fibres may degrade considerably in the presence of moisture. Glass and especially aramid fibres swell by absorbing moisture but carbon fibres are unaffected [27].

When surrounded by resin, as in FRP rebar, the fibres are partially sealed against all physical agents. Electrolytes, light, radiation and thermal energies do penetrate to some degree. The next

section presents these effects in FRP rebars.

2.6.2.2 FRP rebar durability

The American Concrete Institute (ACI) reports [22] that various environmental conditions affect the tensile strength and modulus of FRP rebars to different degrees. The deterioration of strength and stiffness for FRP rebars under controlled conditions is shown in Table 2.1. Glass displays the greatest sensitivity to alkaline, ultraviolet, moisture and elevated temperature exposure, especially for the ultimate tensile strength where up to 75% of the strength may be lost due to alkalinity [22] as shown in Table 2.1 (specific fibre and resin properties, and exposure time were not disclosed). Figures 2.15 and 2.16 show CFRP as having higher resistance than either GFRP or AFRP to temperature. It should be noted that, in most cases, the in-service temperatures will likely not reach a point where significant reduction in performance will be observed, with the exception of the ultimate tensile strength of GFRP rods.

Table 2.1: Reduction, as a percentage of maximum, of strength and stiffness of GFRP, AFRP and CFRPs due to various environments.

	GFRP		AFRP		CFRP	
Environment	**E**	**σ**	**E**	**σ**	**E**	**σ**
Alkaline [22]	0-20%	0-75%	0-20%	10-50%†	0-20%	0-20%
Ultraviolet & moisture [29]	--	0-40%	--	0-20%	--	0-20%
High temperature [30, 31]	Fig 2.16	>20% [30], also Fig. 2.15	Fig. 2.16	Fig. 2.15	Fig. 2.16	>20% [30] also Fig. 2.15

†AFRP rods were exposed to alkaline environment with and without tension simulating pre-construction storage and in-service conditions [32].

It has been shown by the ACI [22] that the GFRP-concrete bond pull-out strength (discussed in section 2.6.1) may be reduced by 80-90% at a temperature of 200° C. It is also well understood that a loss or burn-off of the matrix under extreme temperature eliminates the load-transfer and crack blunting mechanisms of the composite rendering it useless. Thus, FRP reinforcement should be limited to applications where service temperatures will not appreciably approach the glass transition temperature (Tg) of the matrix [22]. This is the primary reason why FRPs are seldom considered for populated buildings or other high-temperature applications except when used together with structural steel for other purposes as in Magnetic Resonance Imaging (MRI) cages.

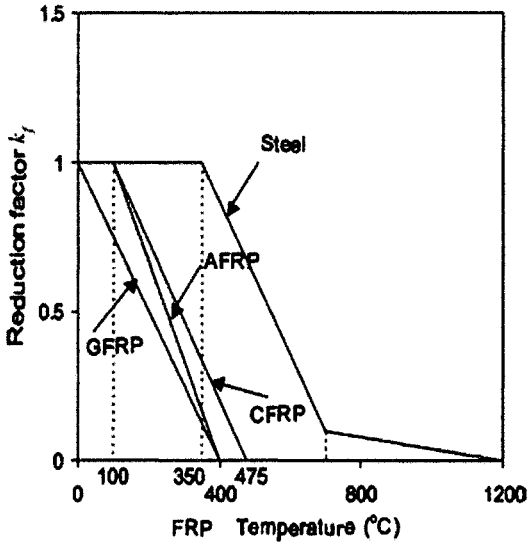

Figure 2.15: Ultimate tensile strength reduction factors for FRP rebar [31].

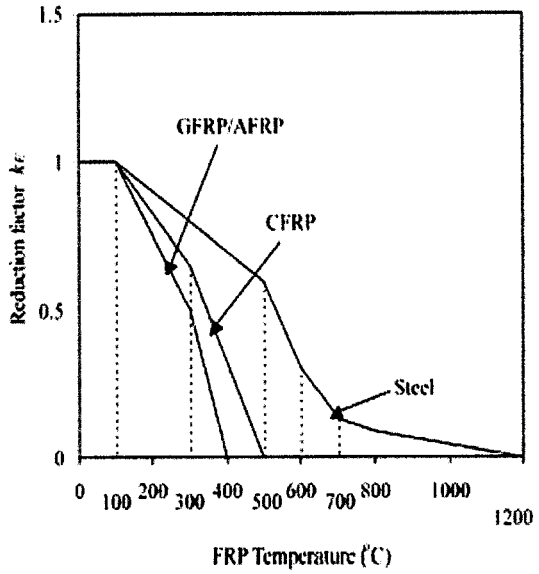

Figure 2.16: Elastic modulus reduction factors for FRP rebar. [31]

2.6.3 Monitoring of FRP reinforced structures

Instead of relying on visual methods for failure prediction, some research is being done on methods for monitoring structural strains. Conventional monitoring techniques involve placing traditional strain gauges or LVDTs on the underside of bridge decks where maximum tensile forces will occur. These, however, lack long-term durability and accurate monitoring is limited to the early years of a structure. A novel monitoring method uses vibrating strain gauges embedded directly into concrete to measure the low amplitude hysteresis of the structure and has proven stable over long terms [33]. One suggested alternative [34, 35, 36] is the inclusion of fibre optic sensors in the core of GFRP rebar. The glass sensors are less sensitive to corrosion and have a similar modulus to the glass fibres in the bar, thus reducing stress concentrations. For CFRP rebar, the resistance change (piezoresistivity) of the carbon fibres under load may be monitored with simple and inexpensive equipment [38].

While continuous monitoring is desirable from a long-term performance perspective, the need for visual warning indicators remains. It is necessary that some form of ductility, whether real or apparent (e.g., pseudo-ductility), be introduced into the reinforcement system.

2.7 Comparison of steel and FRP rebars

The detail of the previous discussions on steel and FRP rebars is summarized in Table 2.2. It is now appropriate to discuss the last item in the comparison, the ductility of the rebar material. Rebar steel can have ductility (based on % elongation) of up to 50% (see Figure 2.1) while the maximum FRP ductility is 4.5%, essentially the maximum tensile fibre strain of the fibres. This is a very large difference and as such has been an active area of research as discussed in Section 2.8.

Table 2.2: Steel versus FRP properties comparison

Property	Steel	FRP
Corrosion resistance	low	high
Ultimate tensile strength, σ_{uts}	400-700 MPa	up to 3200 MPa (CFRP)
Tensile elastic modulus, E	206 GPa	varies with V_f (200 GPa obtainable)
Temperature resistance	maintains strength up to several hundred degrees	poor (oxidation above degradation temperature of polymer matrix)
Yield strength, σ_{yp}	400-700 MPa	no yielding apparent - brittle failure at ultimate tensile strength
Ductility (% elongation)	up to 50%	<4.5%

2.8 Ductility in FRP reinforcement bar

2.8.1 Specific problem definition

The pursuit of FRP reinforcing bars having high ductility has used a given set of fibres, namely carbon, glass and aramid, in combination with thermoplastic or thermoset resins. This has not been successful since the maximum ductility is limited to the maximum fibre strain. This has led to efforts to create a different set of construction codes from those of steel. This new set of construction codes for bridges relies on concrete crushing in compression at the upper surface as the mode of failure [37]. This mode of failure is less predictable than tensile reinforcement failure.

In this work, two novel approaches to increase the limit of the ductility of FRPs closer to that of steel have been undertaken using concepts analogous to fibre pull-out. While many researchers have examined the FRP-concrete bond and pull-out behaviour, none have identified this or similar mechanisms as a means of achieving the desired levels of ductility. The goal is to develop an FRP rebar with the same mechanical properties as a steel rebar that they may be used under the existing construction codes.

2.8.2 Distributed versus local ductility

Figure 2.17 highlights the difference between FRPs and steel. Concrete has both low tensile strength and ductility. Steel, also having considerably higher strength, has a maximum elongation that is many times the maximum elongation of glass and aramid fibres. The FRP materials do have much higher load capacity than steel (after yielding), but are linear up to failure. That is, they do not exhibit a near constant load up to failure as seen in steel.

While reported values of ductility are usually for the entire length of a specimen, reinforcement of concrete should be considered from a local perspective. Figure 2.3 presented various crack and pre-failure conditions along the underside of a beam. Between cracks, the concrete remains intact and the reinforcement shares load transfer with the concrete host. Only within the cracks must the reinforcement yield. Figure 2.18 shows the relationship between crack location, bar tension and bond stress for a reinforced concrete beam. The bar tension varies between cracks, reaching a maximum within the crack and a minimum between cracks as the transfer of load due to bonding reaches a maximum. This is important in that the reinforcement must exhibit ductility only in the crack zone, i.e., local ductility.

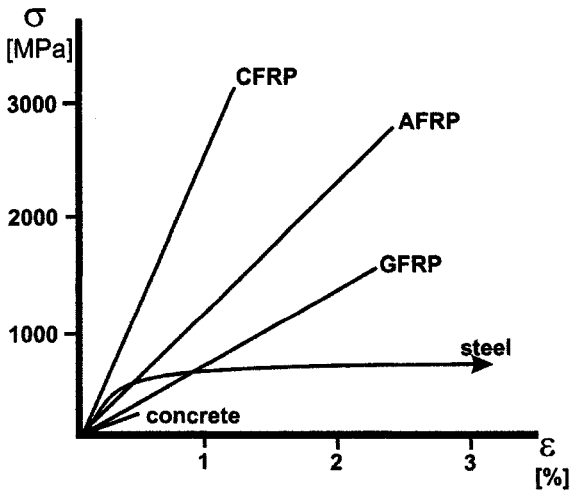

Figure 2.17: Stress-strain curves for concrete and various reinforcing materials.

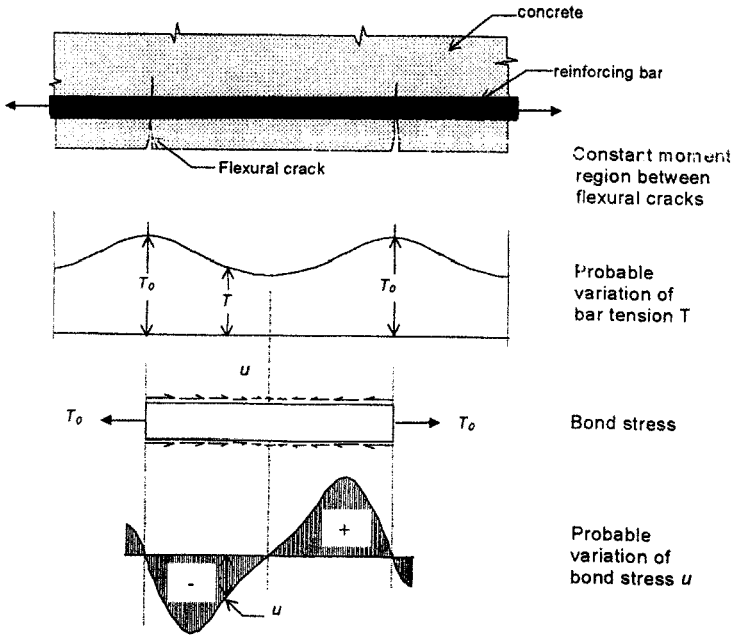

Figure 2.18: Variation of stress in a reinforcing bar at and between cracks in concrete host [44].

2.9 Existing solutions for high ductility

While possessing high toughness and strength, composite materials show negligible plastic deformation up to failure. In simpler terms, the stress-strain curve for a unidirectional composite is linear up to failure as illustrated in Figure 2.17. The limits of ductility for individual fibre types (glass, aramid, carbon) have been reached. Other methods of producing ductile *behaviour*, termed pseudo-ductility, have been pursued with limited success. Combinations of different types of fibres - hybridization - and variations of the fibre placement and/or manufacturing method - structural hybridization - have not achieved resulted in substantial gains in ductility. They are described below for completeness.

2.9.1 Fibre properties

High stiffness is linked to low ultimate strain in the three main fibre types (Figure 2.17). Carbon, or graphite, fibres typically have the highest elastic moduli and ultimate strength. The ultimate strain of glass fibres may be greater than two times that of carbon, but with a lower modulus. Finally, aramid fibres strike a balance between the two, having an ultimate strain similar to glass, but with a modulus between glass and carbon.

2.9.2 Hybridization

2.9.2.1 Fibre hybridization

Combining different types of fibres having differing strengths, failure strains and stiffness results in non-linear stress-strain behaviour. This fibre hybridization has recently been popular with a number of research groups.

The theoretical behaviour of a unidirectional fibre hybrid sample is shown in Figure 2.19. The initial rise is due to contributions from all of the fibres with first failure at the lowest failure strain of the fibres. This is the "elastic zone". Successive slopes, forming a saw-tooth pattern, are produced by sequentially lower contributions from the remaining fibres. This behaviour is termed "pseudo-ductile zone". It is noted that lines with decreasing slope pass through the origin as all fibres are parallel and loaded simultaneously. The extension of the rod is thus still limited to the maximum fibre strain.

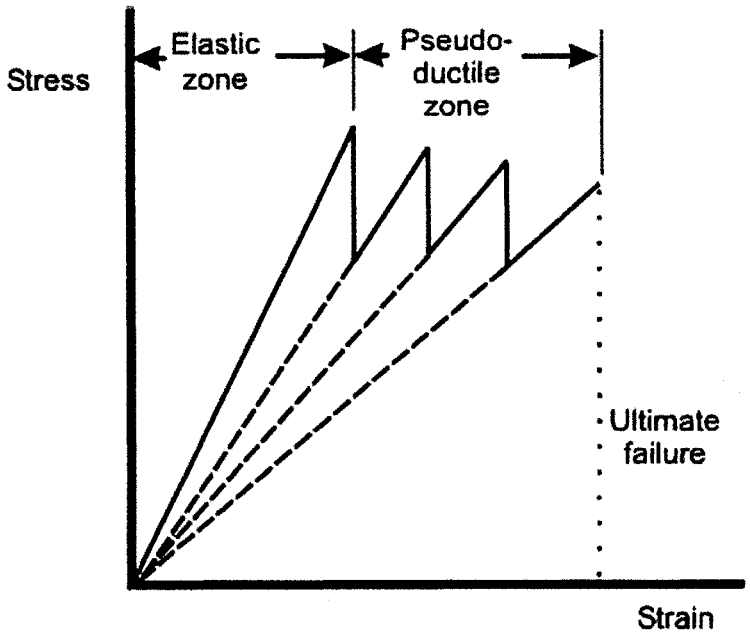

Figure 2.19: Typical fibre-hybrid stress-strain curve (adapted from [5])

Early investigations of this technique were performed by Bunsell and Harris [39] using symmetric laminated plates. Two layers of high-modulus, unidirectional CFRP were sandwiched between layers of lower modulus, but higher ultimate strain GFRP. The CFRP layers provided the initial modulus and a high initial strength. The interaction between the CFRP and GFRP layers, as well as the higher elongation of the glass fibres produced a load-strain curve having distinct elastic and inelastic regions (Figure 2.?). The maximum strain observed was still limited to that of the glass fibres.

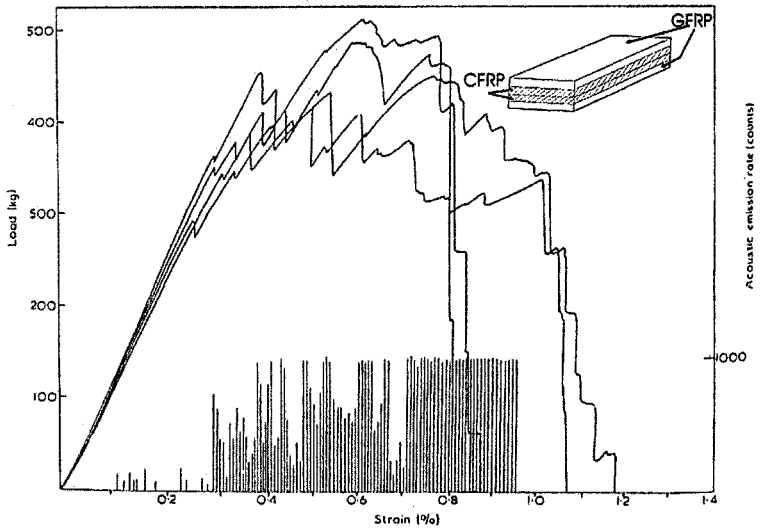

Figure 2.20: Schematic of structure and load-strain curve for CFRP/GFRP laminate [39]

Later tests by Bakis et al [38] eliminated the laminate structure by mixing fibre bundles in pultruded rods. The fibre bundles were placed in different locations throughout the cross section as illustrated in Figure 2.21. A range of volume fractions and matrix types were used. Pseudo-ductility of the type described above was achieved in several of the rods but the maximum strain was limited to 1.7%.

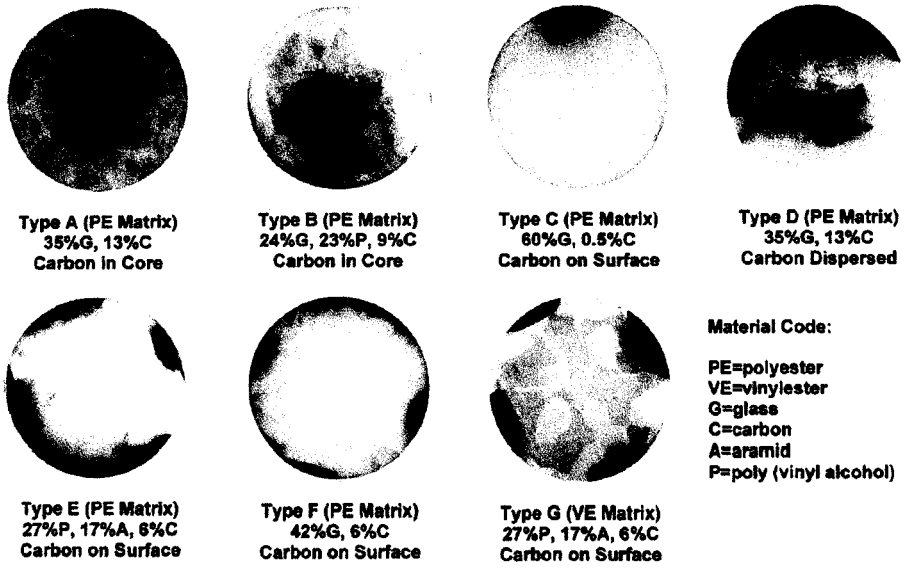

Figure 2.21: Cross-sections of structural variants of glass/carbon hybrid rebar [38].

A sample of the Bakis specimen load profile for a carbon (V_f=13%) and glass (V_f=35%) Type A fibre hybrid is given in Figure 2.22. The first peak indicates the failure of the lower ultimate strain carbon fibres. The second peak represents the failure of the glass fibres. Interestingly, the resistance of the carbon fibres does not change until first failure. This suggests that either the carbon fibres were not well aligned with the longitudinal axis of the specimen in the unloaded state or the sensitivity of the system is insufficient to indicate the integrity of the system. Either case illustrates the importance of visual indicators in detecting structural faults – errors in the manufacture or installation of electronic monitoring systems may result in service under unsafe conditions.

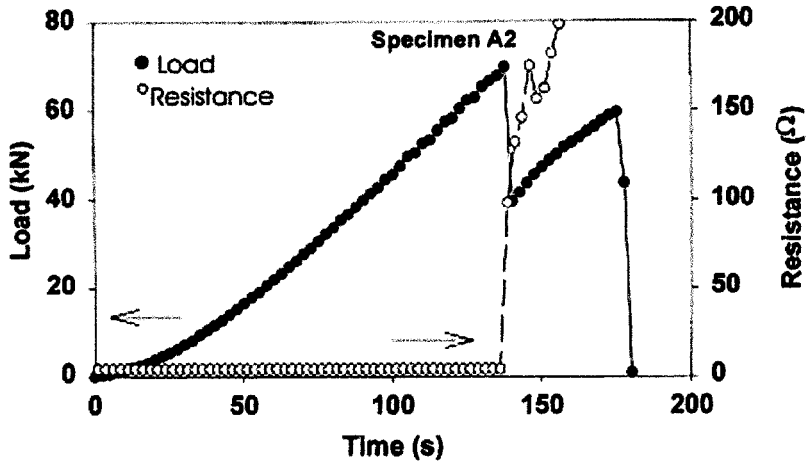

Figure 2.22: Load versus time plot for a specimen (Type A) by Bakis et al [38] as shown in Figure 2.21

2.9.2.2 Structural hybridization

With the limitation on ductility using unidirectional fibres parallel to the axis of the rod being established as that of the fibres employed, Tamuzs and Tepfers [41] manufactured rods having 2D-braiding over compressible cores of various type, including glass tubing and porous polyurethane. Upon application of load, the fibres would begin to orient in the direction of the load. During reorientation, the inner core would collapse allowing further reorientation and elongation of the braid. The obvious drawback was a reduction in diameter, reducing or eliminating rebar-concrete bond in addition to little improvement in the overall strain.

Somboonsong, Ko and Harris [40] attempted to further increase the maximum elongation by reorienting portions of the fibres off the axis of the rod. Using unidirectional carbon fibres in the core to provide high rigidity and initial strength, an outer layer of lower modulus aramid fibres was applied by braiding. At the point of fracture of the carbon fibres, the aramid fibres reoriented towards the rod axis and received the load from the carbon fibres. The technique was successful (Figure 2.23) in increasing the maximum strain for some of the specimens, but self-locking nature of the braid prevented full reorientation. The maximum strain reported was 2.5%.

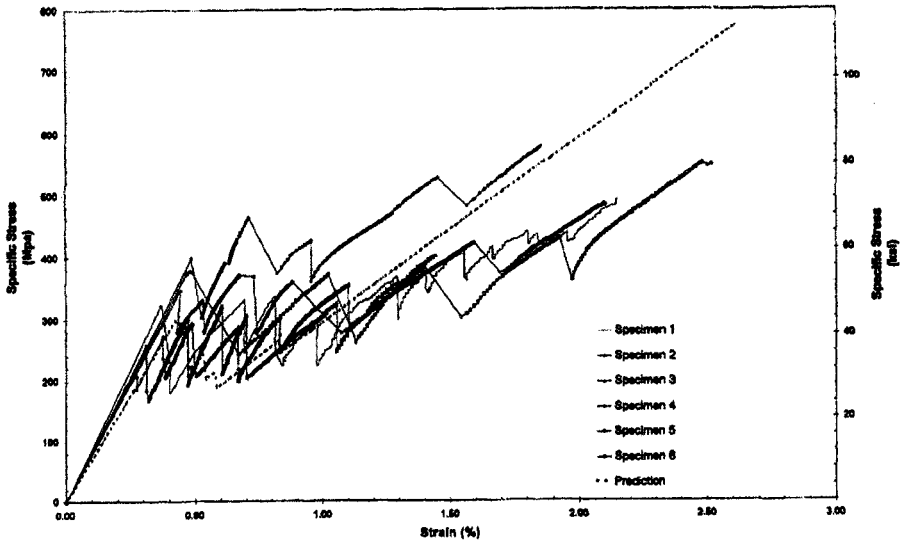

Figure 2.23: Hybrid core with braided over wrap - CFRP and GFRP hybrid. [40]

Belarbi and Chandrashekhara [42] manufactured hybrid cores covered in filament wound shells. The complete alignment of the fibres to the axis of the rod did not occur (Figure 2.24) and the resulting maximum strain was 1.6%

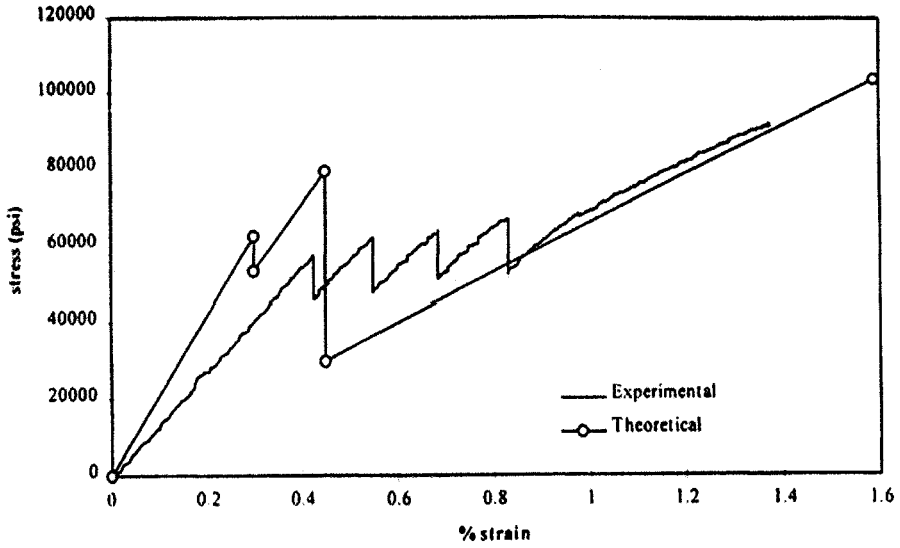

Figure 2.24: Theoretical and experimental stress-strain curves for unidirectional core with filament wound over wrap [42].

2.9.3 Effect of unbonded length on mechanical properties

De la Rosa [5] produced rods having a fibre composite inner rod with four types of carbon fibre (Figure 2.25) wrapped in a 2D braided aramid shell (over-wrap) in order to determine the effect of unbonded length on the ultimate strength and general behaviour. The fibres were arranged in order of increasing fibre strain from the inside out. The aramid shell served to transfer the applied load between the concrete and the fibre composite inner rod and did not have a significant load carrying ability.

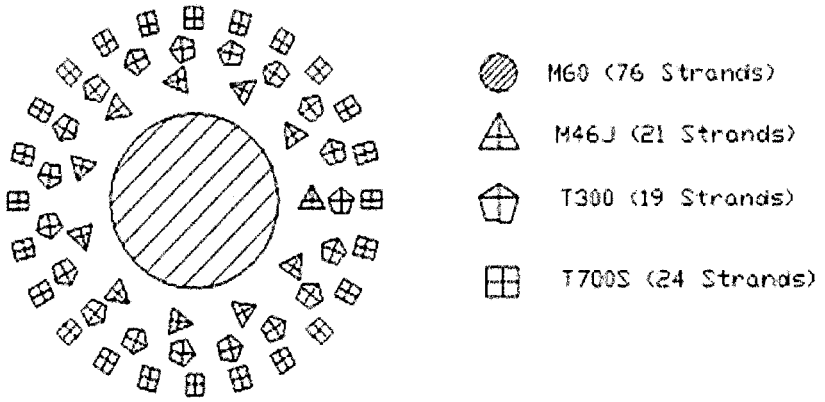

Figure 2.25: Cross section of unidirectional core of rods by de la Rosa [5]

The predicted, expected[1] and experimental behaviours are shown in Figure 2.26. The experimental curve is for a specimen having an unbonded length of 500 mm. The ultimate strain was less than expected, and the loads higher, but the characteristic sawtooth pseudo-ductility was observed. In general, de la Rosa found that the ultimate load increases with a decrease in the unbonded gauge length due to a higher statistical probability of defects in longer rods. However, several of the rods with smaller gauge length exhibited unexpected load-displacement performance. High loads were sustained for large displacements. In the present study, the reasons for the anomalies were investigated and the discoveries formed the basis for the remainder of the work. The following Chapter discloses the results of the investigation.

---

[1]Expected loads are 77% of predicted values based on previous tests results [5] where experimental loads were approximately 33% lower than design loads.

Page 32 missing.

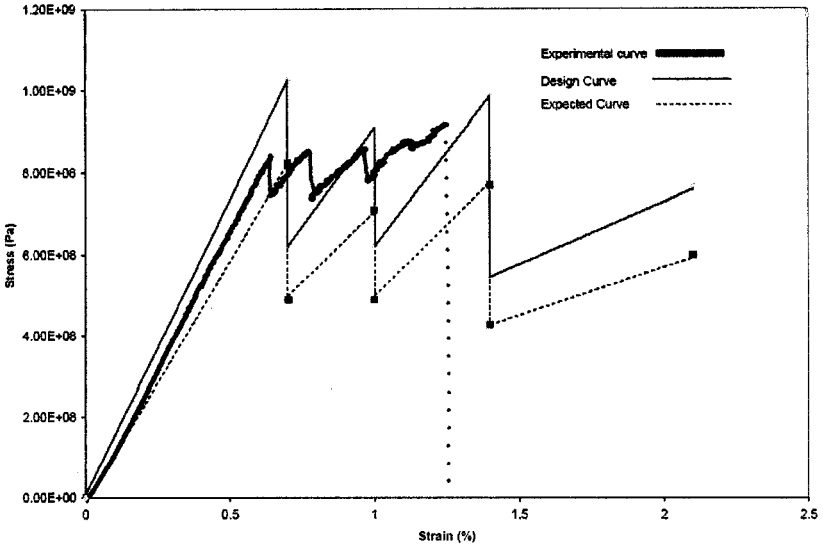

Figure 2.26: Design, expected and experimental curves for FRP rebar by [5]. The experimental curve is for a rebar with gauge length 500 mm.

Chapter 3: Investigation of Unpredicted Tensile Behaviour

The hybrid rods [5] were tested for ultimate strength and, elastic modulus (for the 500 mm gauge length). For a better understanding of the results, the test setup is presently described. The rods were mounted in internally rifled steel tubes filled with high shear strength MBRACE epoxy resin system as illustrated in Figure 3.1 and tested in tension to produce load-displacement curves using an Instron 1332 servo-hydraulic machine. A data recorder powered by LabVIEW in parallel with a chart recorder recorded the results. A second chart recorder was connected to an extensometer to accurately measure the elastic modulus for selected specimens. The specimens from de la Rosa's study were longitudinally sectioned as part of the current work; sectioning was done with a slitting saw mounted in a milling machine or a bandsaw.

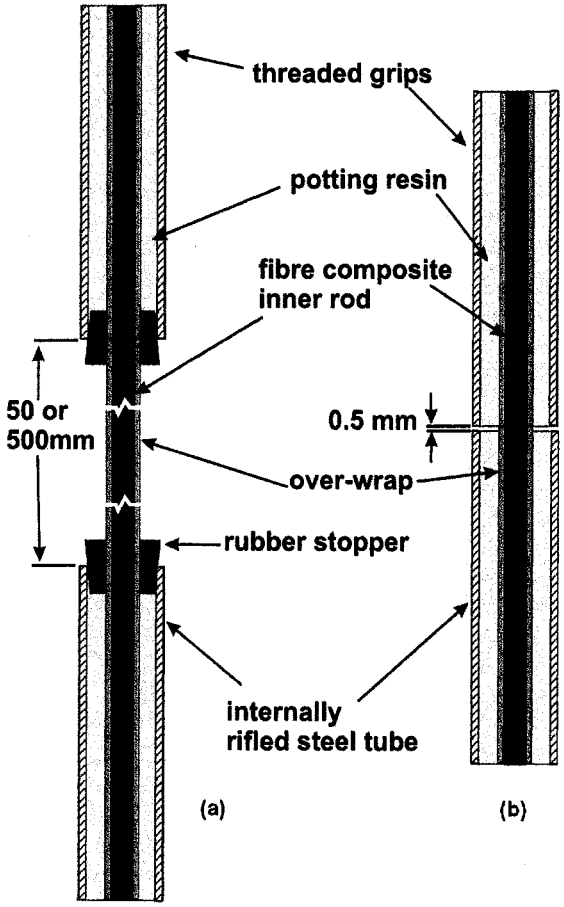

Figure 3.1: General schematic of the test set-up for hybrid FRP rebar. (a) 50 or 500 mm gauge length (b) 0.5 mm gauge length.

Test results showed three distinct load-displacement behaviours illustrated in Figures 3.2 and 3.3. The failure types are categorised herein as Type I, Type II and Type III, the details of which are presented in Figures 3.4, 3.5 and 3.10, respectively.

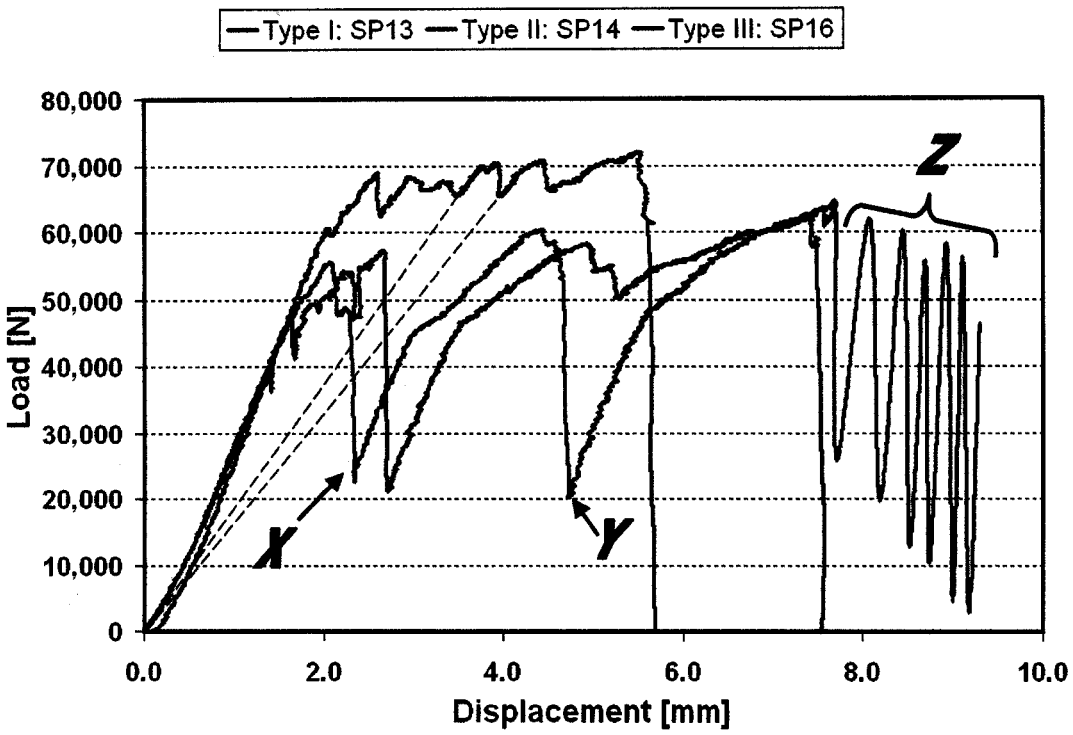

Figure 3.2: Load versus displacement curves for select specimens having a gauge length of 0.5 mm.

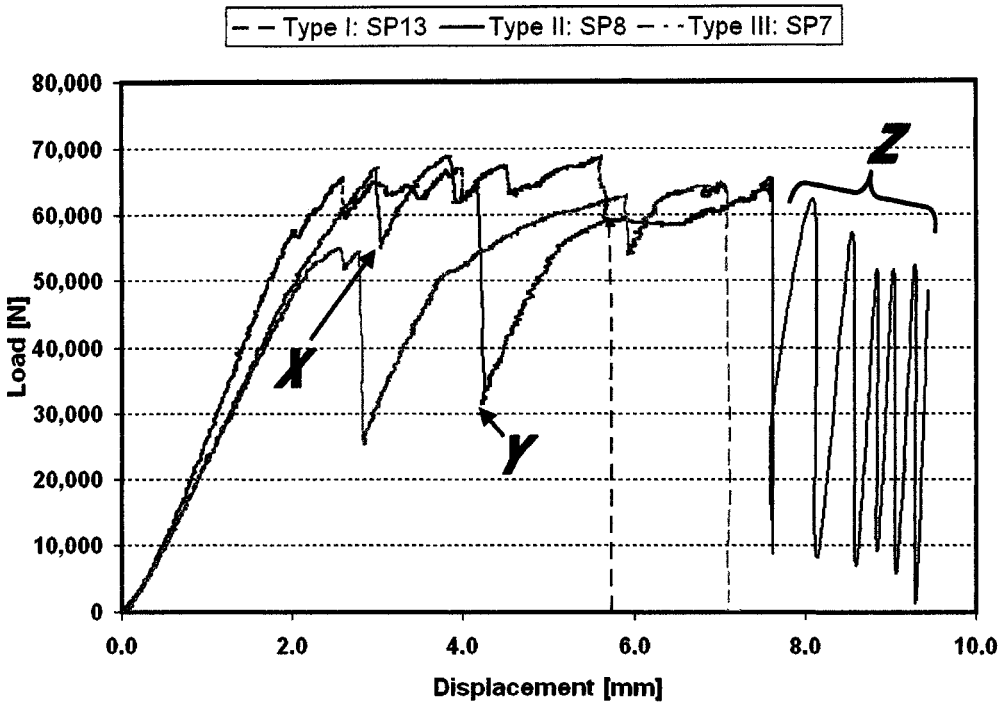

Figure 3.3: Load versus displacement curves for select specimens having a gauge length of 50 mm. (Note: SP13 had a gauge length of 0.5 mm and is included here for comparison).

3.1.1 Type I failures

Type I failures exhibited pseudo-ductility as predicted in [5] and failed in either the gauge length (illustrated schematically in Figure 3.4) or at the transition from gauge length to embedded portion. The measured loads were slightly higher than predicted. Both the aramid over-wrap and hybrid graphite core failed in a single location. Successive elastic behaviour in the pseudo-ductile zone is due to the contribution of the unfailed fibre types in the rods. It is noted that a line coincident with each slope passes approximately through the origin (see dashed lines for SP13 in Figure 3.2) suggesting elastic recoil to near original length upon removal of load as previously described (Figure 2.19)

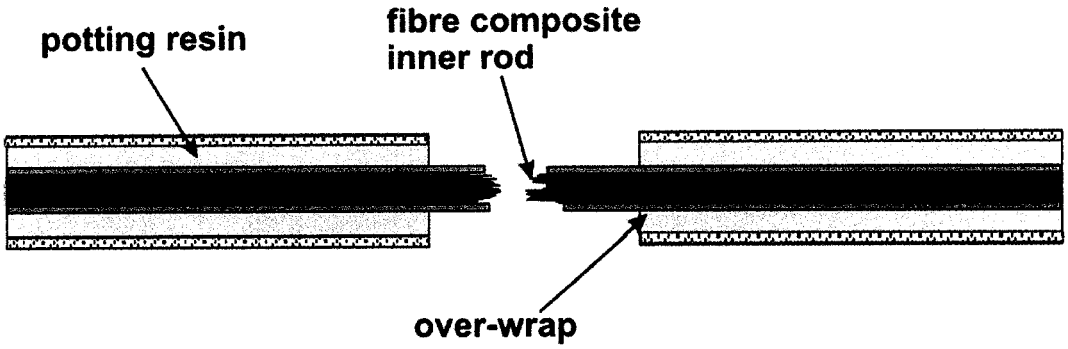

Figure 3.4: Type I failure: classical failure of carbon rod and aramid over-wrap.

3.1.2 Type II failures

Type II failures, occurring in specimens of 0.5 and 50 mm gauge length, exhibit similar initial elastic rise as in Type I followed by a rapid drop in load associated with debonding of either the potting resin/over-wrap interface or the over-wrap/inner rod interface. The former is most likely due to the presence of the unpotted gauge section and associated change in modulus. This point is indicated by 'X' on in Figures 3.2 and 3.3. Following this drop – varying in degree for the specimens – is another linear rise; this precedes another debonding and loading segment at the second interface (point 'Y'). The final common characteristic in the load displacement behaviour is a series of large, rapid load variations (zone 'Z') similar to stick slip behaviour seen in steel rebar/concrete grout bond pull-out tests [Figure 1.14].

The sectioned samples exhibiting Type II failure behaviour had several features of the

sections which were common among the specimens. Observable in a pre-sectioned state, the carbon rods had shifted inwards at both grip ends. The degree of shifting was greater at one end (as in Figure 3.5)

Additionally, a portion of the over-wrap had pulled out of one of the grips on each specimen. This was observed during the testing stage. It was noted that the over-wrap was secure in the grip ends where the carbon core had shifted. Sectioning revealed that the over-wrap had fractured inside the potted length of the grips allowing the post debond pull-out of the over-wrap. The frictional strength of the over-wrap/core interface was high enough to maintain load transfer leading to the shifting of the carbon rod with respect to the anchored over-wrap. A schematic of the sectioned specimen showing the above features is provided in Figure 3.5. Several photographs of pre-sectioned and sectioned Type II specimens are presented in Figures 3.6 to 3.9.

The pull-out of the over-wrap contributed the stick-slip portion (zone'Z') of the load-displacement curves as the jacket keyed mechanically with the epoxy due to the braid undulations until the load rose again to surpass the keying load and the process repeated.

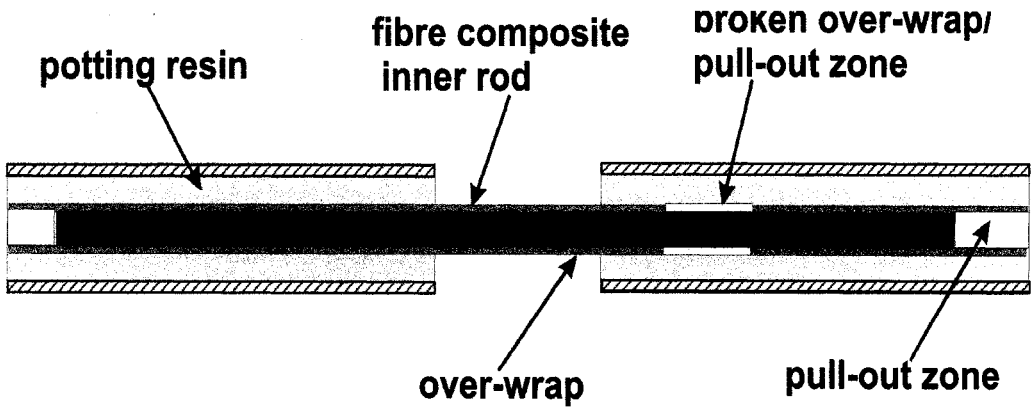

Figure 3.5: Type II failure - fracture of the aramid over-wrap within the potted length and subsequent pull-out of the system.

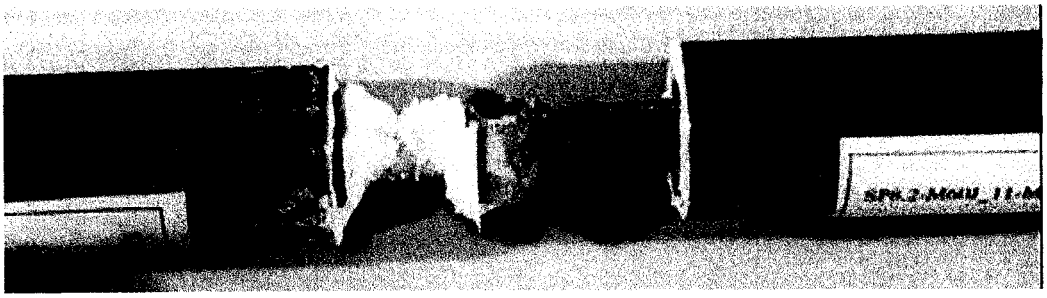

Figure 3.6: Image of SP 8 prior to sectioning of the anchors. Pull-out can be observed at both ends. The right side (SP8.2) experienced Type II failure.

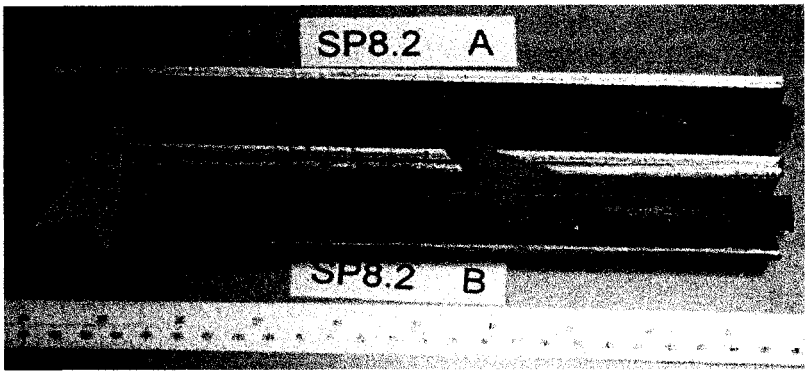

Figure 3.7: Image of sectioned SP8.2 rod anchor. The light coloured arrow indicates the shift between the carbon rod and over-wrap. The dark coloured arrow indicates the over-wrap fracture and pull-out.

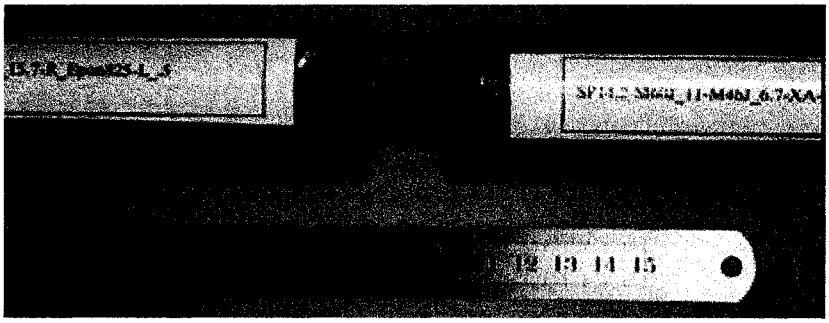

Figure 3.8: Image of extended gauge section of SP14.2. The original gauge length was 0.5 mm; the test was stopped when the gauge section had reached approximately 28 mm.

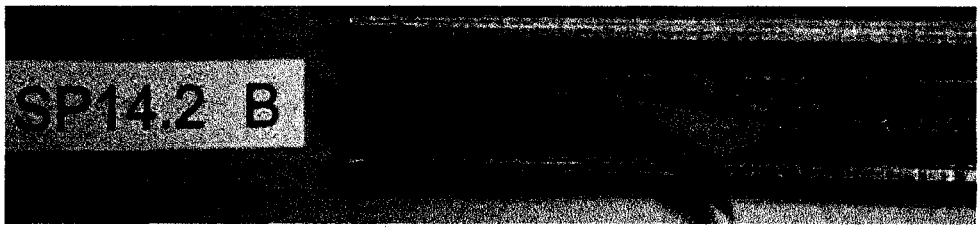

Figure 3.9: Sectioned SP 14.2 anchor showing failed Kevlar over-wrap pull-out

3.1.3 Type III failures

Finally, Type III failures display a variety of load-displacement curves. Common to these is the initial linear-elastic portion as in Type I and Type II. Sudden or measured decreases in load, constant load, and combinations thereof were observed in the post-elastic zone. Type III specimens exhibited shifting occurring between the carbon inner rod and aramid over-wrap. The degree of shift is between 3 and 15 mm and includes the entire rod, typically from both ends. In some cases the rods fractured in the gauge length (Figure 3.10).

Whereas the over-wrap of Type II specimens failed within the potted sections, the Type III over-wrap remained intact in this area; pull-out was limited to the inner rod. The smaller degree of pullout seen in the Type III specimens was dictated by the cessation of testing and would possibly have been as large or larger than the Type II specimens.

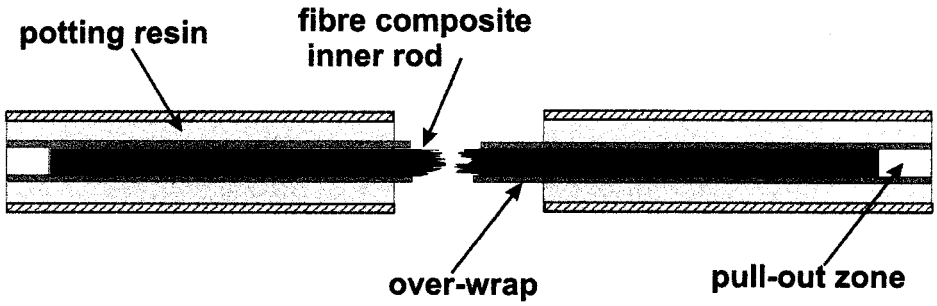

Figure 3.10: Figure Type III failure - pull out of carbon relative to aramid over-wrap; fracture of FRP inner rod occurred for some specimens (illustrated)

One specimen, SP10 - identified as Type IIIb - is distinct in both the load-displacement curve and observed failure condition. The pull-out zone suggests constant load for several millimetres of pull-out, though the magnitude is quite low relative to the debonding load. The failed specimen shows classical fibre pull-out in the gauge length. The failed shards appear to be small bundles of fibres. At a higher pull-out load, this is perhaps the ideal state. The load-deflection curve and a cross-section of the specimen are given in Figure 3.11.

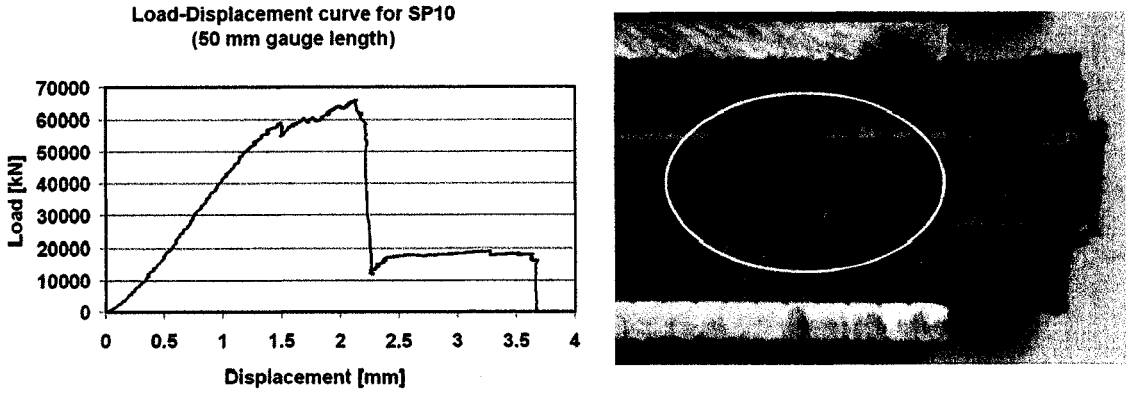

Figure 3.11: Load displacement curve (left) and close-up of fibre pull-out failure of SP10 from [5]

A summary of specimens and their failure types, segregated by gauge length, is given in Table 3.1. It is obvious from the chart that relative sliding mechanisms are predominant in specimens with smaller gauge lengths (0.5 and 50 mm) which are similar to typical cracks on the underside of a concrete beam under service loads.

Table 3.1: Summary of rod failure types by gauge length.

		Failure Type		
Gauge length	**Specimen**	**I**	**II**	**III**
500 mm	**SP1**	X		
	SP2			X†
	SP3	X		
	SP4	X		
	SP5	X		
50 mm	**SP6**			X
	SP7			X
	SP8		X	
	SP9			X‡
	SP10			X
0.5 mm	**SP11**			X
	SP12			X
	SP13	X		
	SP14		X	
	SP15			X
	SP16			X

†SP2 Data resembles Type III failure, but does not show physical signs of pull-out.
‡SP10 exhibited localised classic fibre pull-out at the gauge section/potting interface.

3.1.4 Analogy to short fibre composites

The characteristics of the load-displacement plots together with the physical failure modes for the described specimens are similar to those of short fibre composites. More specifically, they resemble single-fibre pull out tests results. Short fibres are used in many composite applications to maximise the toughness of a given product by exploiting interfacial properties. The results discussed above suggest the same mechanisms as in short fibre theory may be applied to achieve higher apparent ductility. The next Chapter thus provides a background on short-fibre composite theory and highlights information necessary to fully understand the different options for pseudo-ductile rebar.

Chapter 4: Theory of Short Fibre Composites

The addition of fibres having high strength and high stiffness to a polymer matrix imparts these characteristics to the resulting composite. However, the length of fibre determines if the composite will fail in a brittle manner or experience pull out. In short fibre composites fibre pull out can occur. While the strength and stiffness are decreased, the ductility is increased. Pull out is advantageous in that it requires the breaking of the interface between the matrix and fibre, giving an initial stiffness (see (i) in Figure 4.1). After interfacial failure (see (ii) in Figure 4.1), frictional sliding between the fibre and interface supports a gradually decreasing load as the fibre pulls out of the matrix (see (iii) in Figure 4.1). The theory related to pull out is now presented.

4.1 Critical length of fibres

At a certain fibre length, the tensile force carried by the fibre at its maximum tensile stress and the frictional forces of the fibre-matrix interface surrounding the fibre are balanced. This is known as the fibre critical length. Increasing the length of the fibre results in fibre fracture (a brittle failure mode) as the interface strength exceeds the fibre strength. Decreasing the length results in failure of the interface and leads to one half of the fibre being pulled out of the matrix (a "ductile" failure mode).

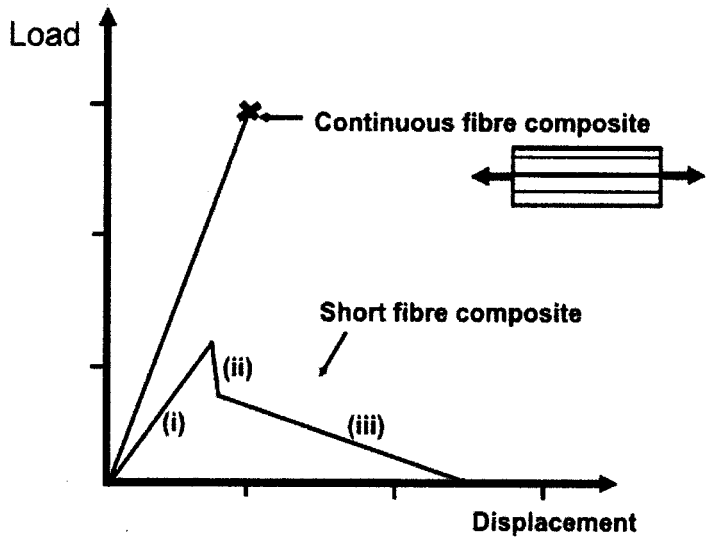

Figure 4.1: Comparison of load-displacement generic curves for continuous and short fibre composites.

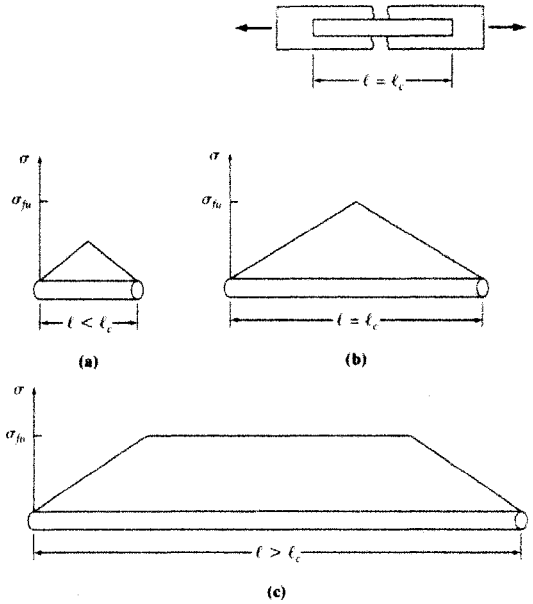

Figure 4.2: Stress in a fibre for varying lengths relative to critical length, l_c. [11, p 368]

Figure 4.2 illustrates the three states of tensile fibre stress along a fibre in a fibre composite loaded along the fibre. 4.2(a) shows the fibre at less than the critical length. Here, the fibre failure stress, σ_{fu}, will never be reached. More precisely, there is insufficient transfer of the load from the matrix to the fibre to result in fibre fracture. Figure 4.2(b) illustrates the balanced condition where the maximum fibre stress equals the fibre failure stress; the fibre length is equal to the critical length. In this case, either one half of the fibre may pull out of the matrix or the fibre will fracture at the midpoint of its length. Finally, figure 2.4(c) presents the case of long or continuous fibres where the fibre length exceeds the critical length considerably. Fibre fracture is the sole mode of failure for this case.

The critical length is dependant on fibre and interface parameters as detailed in Equation 4.1.

$$l_c = \frac{P}{\pi \cdot \phi \cdot \tau} \tag{4.1}$$

where l_c is the critical length,

P is the load in the fibre,

ϕ is the fibre diameter, and

τ is the frictional shear stress of the interface.

4.2 Fibre pull-out

Assuming the length of a fibre is less than the critical length, Equation 4.1. may be rearranged to predict the load required during pull-out (equation 4.2). Figure 4.3 shows a segment of embedded fibre with tensile and shear loads.

$$P = \tau \cdot \pi \cdot \phi \cdot (l_e - \Delta) \tag{4.2}$$

where l_e is the original embedded length, and

Δ is the distance the fibre has been pulled out.

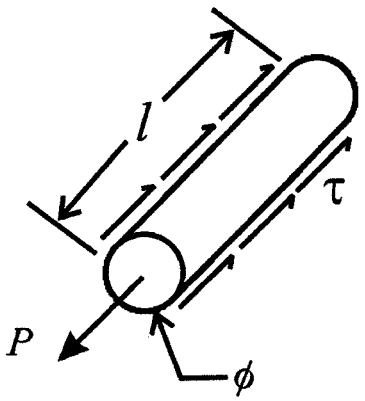

Figure 4.3: Force balance and parameters for a short fibre in tension.

As the fibre is pulled out of the matrix, a smaller length of the fibre remains embedded resulting in a decreased shear area, thus a lower load is required to continue pull-out. For an ideal short fibre composite, the load decreases linearly as the embedded length decreases. The rate of decrease, i.e., the slope of the load-pull-out curve (Figure 4.4) is also dependent on the fibre diameter and the frictional shear stress at the interface.

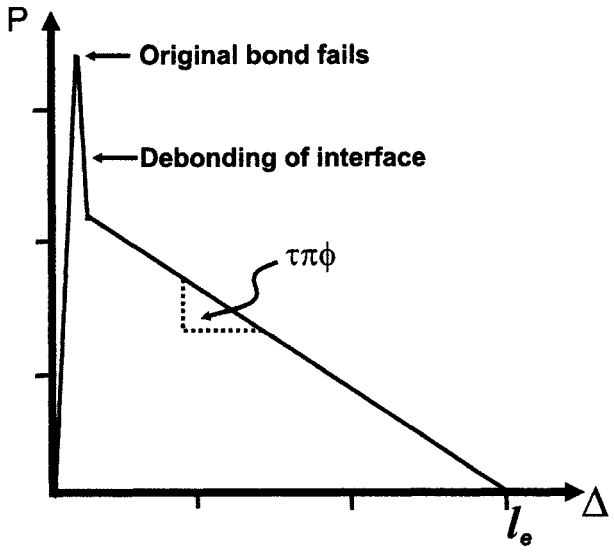

Figure 4.4: Plot of fibre pull-out.

4.3 Strength and stiffness of unidirectional, short-fibre composites

It was stated earlier that the strength and stiffness of composites using short fibres are reduced as compared to the case for a continuous fibre composite. The ROM prediction for composite strength where fibres are less than the critical length is similar to the ROM for continuous fibre composites, but the ultimate strength of the fibre is replaced by the interfacial properties (Equation 4.3).

$$\sigma_C = \sigma_m \cdot (1 - V_f) + \frac{\tau\phi}{l} \cdot V_f \qquad (4.3)$$

where $\tau\phi/l$ replaces the term in Equation 2.1 (continuous fibres) and represents the contribution of the short fibres.

The stiffness, i.e., elastic modulus, is not predicted using this method as the mechanics for short fibres are different. Halpin [43] and Tsai developed a widely accepted model for predicting the elastic modulus of short fibre composites (Equation 4.5). This equation is used to predict the contribution of short fibre rods in one of the methods to produce pseudo-ductile rebar as introduced

in the next section.

$$E = \frac{1 - 2\frac{l_c \cdot \eta_l}{\phi}}{1 + \eta_l \cdot V_f}$$

where

$$\eta_l = \frac{\frac{E_f}{E_m} - 1}{\frac{E_f}{E_m} + 2\frac{l_c}{\phi}} \qquad (4.5)$$

where η_l is the fibre efficiency,

E_f is the elastic modulus of the fibre,

E_m is the elastic modulus of the matrix,

l_c is the critical fibre length, and

ϕ is the fibre diameter.

4.4 Application of pull-out theory to FRP rebar

It was described earlier that a large amount of research is directed towards the anchoring of FRP reinforcing bars in concrete by altering the surface of the reinforcement. Test set-ups and results are very similar to fibre pull-out tests aimed at increasing ductility of composite structures. It is surprising, then, that the two do not appear to have been combined previously. The methods described in this body of work extend the pull-out mechanism to FRP reinforcement of concrete by encouraging relative sliding of the rebar and concrete, rather than promoting improved anchoring. Traditional steel reinforcement is not anchored in regions where the rebar deforms, so it should not be necessary that FRPs are locked into place.

Two distinct approaches to pseudo-ductile rebar, both relying on interfacial properties, were taken. The first approach employs large 'fibres' or meso-scale FRP discontinuous rods having known pull-out characteristics mixed, in combination with continuous fibres for stiffness, in a matrix

to produce a continuous/discontinuous hybrid rebar. The design, manufacture and testing of specimens using this approach are detailed in Section 5.1 . The second approach, detailed in Section 5.2, involves a fibre composite rod with the required stiffness, covered by an over-wrap with regular intervals of discontinuity. The over-wrap/inner rod interface is a highly controlled surface producing a predictable, repeatable and relatively constant pull-out load. The outer surface of the over-wrap is rough to provide sufficient anchoring to the concrete.

Chapter 5: Development of High Ductility Rebars

5.1 Method A: Multiple meso-rod reinforcement

A theory based approach was taken to design conceptual specimens having sustained load-deflection behaviour via the simultaneous pull-out of multiple meso-rods over a cross-section at any location along the length. Initially, a series of short-fibre coupons were manufactured to determine the range of ductility that may be expected from traditional unidirectional, short-fibre bars. A numerically controlled machine fitted with a high strength steel X-Acto® blade was used to chop prepreg carbon fibre strips to nominal lengths of 0.5, 1.0, 2.5 and 5.0 mm which were then formed and cured into elongate, rectangular cross section specimens. Micrographs showing the alignment and distribution of a portion of the 0.5 mm specimens are seen in Figure 5.1.

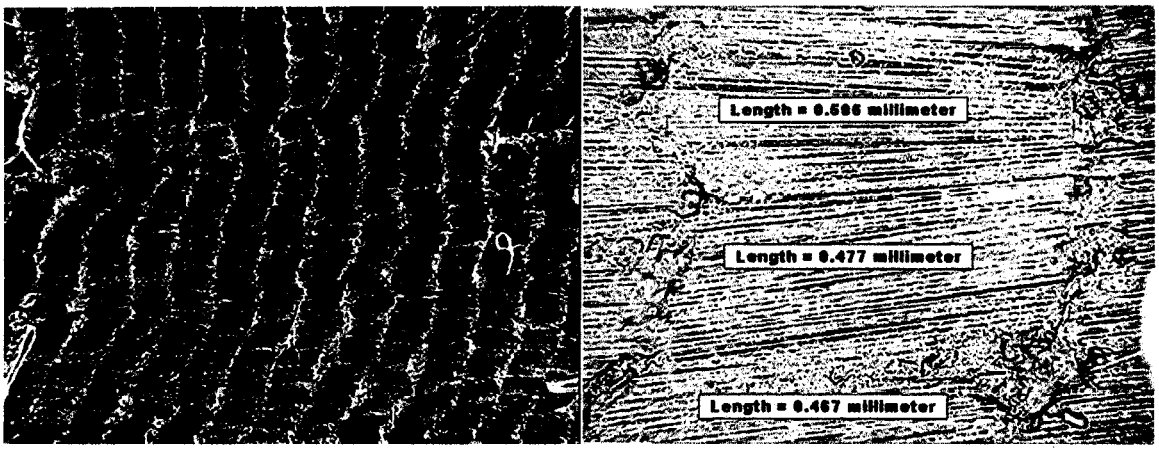

Figure 5.1: Micrographs of 0.5 mm unidirectional short-fibre composite coupons at 2x (left - dark field) and 20x (right - bright field)

Tensile testing of the coupons showed failure strain was limited to less than 1% with failure strain increasing with fibre length. In contrast to the theoretical cumulation of fibre pull-out at numerous sites, the failure was localised to a small region on each specimen. The difficulty in manufacture of such specimens and the need to increase the strength and stiffness of rebar designed from short-fibre theory led to the use of larger discontinuous bundles of fibres in combination with continuous fibres. Two distinct families of meso-rod specimen were created: a concept model having fully discontinuous unidirectional 'fibres' made of steel, and another having a combination of discontinuous and continuous unidirectional carbon fibre reinforcement.

5.1.1 Fully discontinuous, multiple steel meso-rod design

5.1.1.1 Determination of interfacial shear stress for epoxy resin system and steel

For manufacturing simplicity, dowel pins were selected to simulate short fibres in a concept model to illustrate the behaviour of a composite rod having aligned fibres shorter than the critical length. The pins had highly polished surfaces and excellent dimensional tolerance. The interfacial frictional shear stress for the selected matrix and steel was determined using steel dowel pins suspended in an epoxy resin coupon (100 parts Epon 825 epoxy resin plus 19 parts Ancamine 1482 hardener cured for 90 minutes at 110° C). The dowel pins had a diameter of 4.76 mm, a half-length of approximately 25.4 mm and the epoxy resin coupon cross section was approximately 12 mm x 12 mm. The specimens were tested in tension in the presence of a crack at the mid-length of the dowel (see schematic, Figure 5.2). The bond between the dowel pin and the matrix was broken manually for one-half of the specimen prior to testing to isolate the pull-out behaviour.

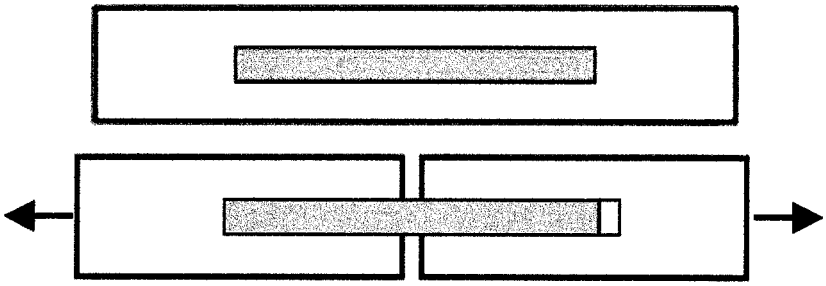

Figure 5.2: Schematic of pull-out behaviour of steel meso-rod specimen.

The load-displacement plots for four specimens are shown in Figure 5.3. Excellent repeatability is observed for specimens 2 to 4. The first specimen was not included as it failed at the interface of the grip tabs during mounting. The average frictional shear stress, τ, for specimens 2 to 4, calculated using Equation 4.2 rearranged to isolate the shear stress (as in Equation 5.1) – was 0.66 MPa.

$$\tau = \frac{P}{\pi\Phi(l-\Delta)} \tag{5.1}$$

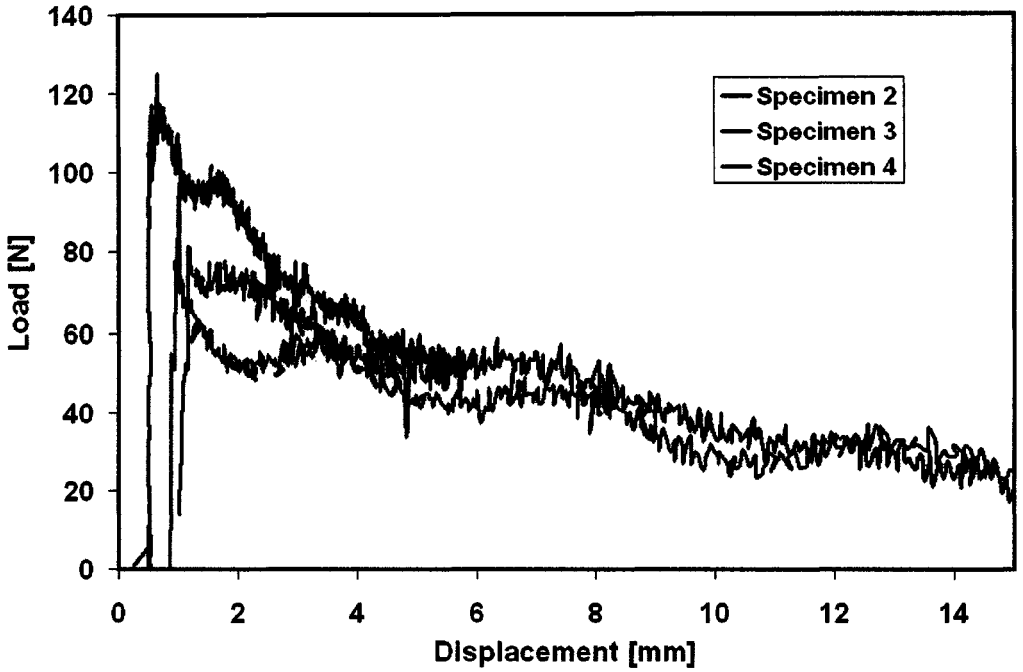

Figure 5.3: Load-displacement curves for steel-rod pull-out tests.

5.1.1.2 Design of multiple steel meso-rod rebar

To ensure the same tensile load-carrying capability at all cross-sections along the length of the specimen, it was necessary to space the 'fibres' such that a slice through the sample would be the same as another slice at a different location (Figure 5.4). In general, the spacing of fibres to produce the most consistent cross-sections may be found by Equation 5.2. Limits in the physical size of test equipment and constituent materials, seven steel meso-rods were chosen for the present specimen. The fibre arrangement ensures that six 'fibres' carry load at the onset of pull-out. The arrangement of the steel meso-rods in the cross-section was done to balance the load carrying capability (i.e., strand 3 and 4 were opposite each other).

$$s = \frac{l_f}{n+1} \tag{5.2}$$

where s is the spacing between fibres having coincident axes,

l_f is the length of the fibre, and

n is the number of strands in the composite.

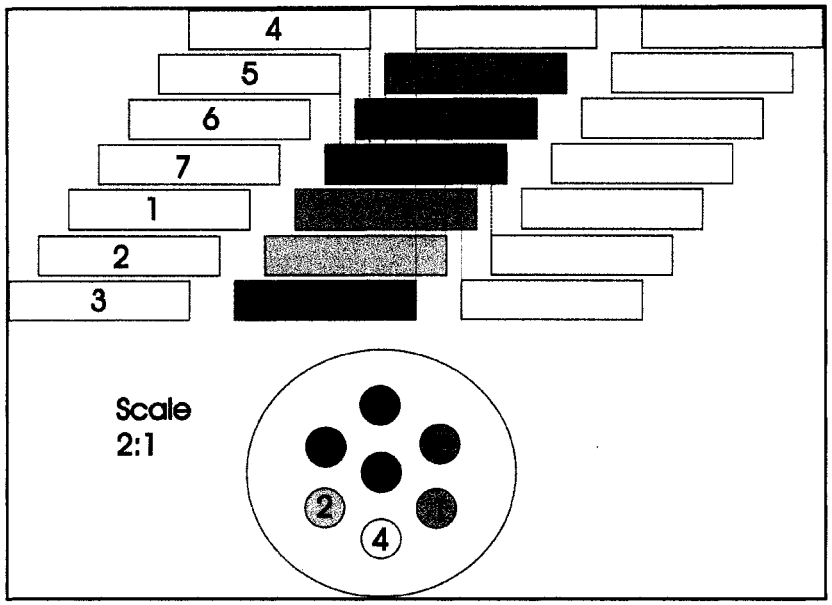

Figure 5.4: Strand configuration giving most consistent cross section for 7-strand specimen.

The theoretical load-pullout curve is shown in Figure 5.5. The slope changes and a load shift occur at displacements where a fibre no longer contributes to load bearing. This is because for every unit of displacement, the total embedded length decreases by the displacement multiplied by the number of spacers still embedded; at the slope change, the embedded length decreases by a lower multiple of the displacement. This is also why the magnitude of the slope increases.

A second plot is superimposed on the design curve. This second plot shows the trend line of a *single* fibre having the same initial embedded length as a single fibre from the multiple strand design and a circumference equal to the circumference of a single fibre multiplied by the number of fibres in the specimen. The same surface area participating in the first stage of pull-out therefore exists between the two plots. For the multi-fibre specimen, the participating surface area drops each

time a fibre pulls free from the matrix.

While it first appears that a single fibre is more effective in carrying load, it is important to note that the multiple meso-rod specimen is not fully representative of a scale product as it was designed to avoid fibre repetition; an actual rebar would have many repeating strands ensuring a higher load carrying capability throughout and behaviour similar to that of the single fibre specimen.

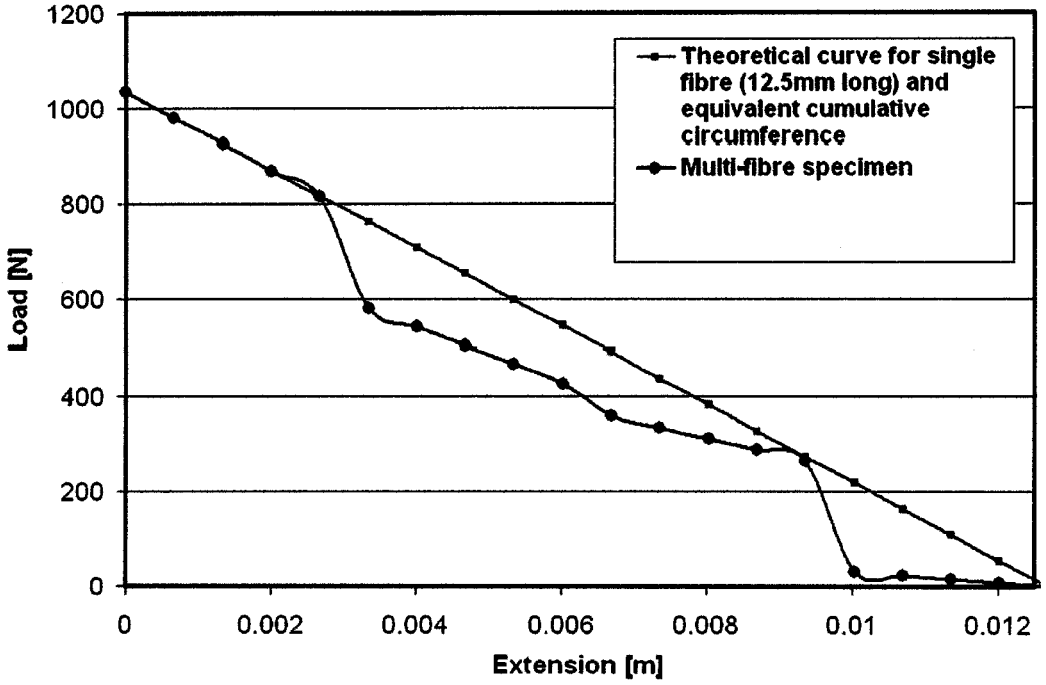

Figure 5.5: Predicted pull-out curves for multi-strand steel specimen and a single fibre of equal length and equivalent cumulative circumference.

5.1.1.3 Preparation of multiple steel meso-rods rebar

Mould-released steel threaded rods were placed through the centre of hollow steel spacers during manufacture to maintain alignment of the spacers. A compression spring was placed at the top of the rods to assist in sealing the contact between steel and plastic spacers. Polyvinyl tubing was placed at the bottom of each strand and cut to varying lengths to offset the spacers in each strand from adjacent strands as in Figure 5.4. A close-up of the assembled strands is provided in Figure 5.6. The strand pattern was achieved by using an end-cap with a pattern of holes threaded to receive

the alignment rods externally threaded at the end. A hexagonal pattern with a central strand was used (Figure 5.7).

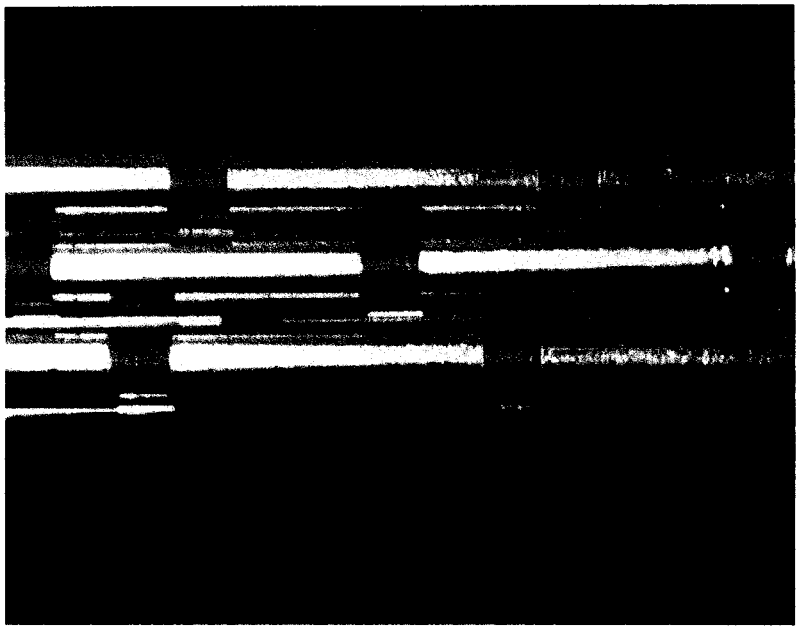

Figure 5.6: Close-up of discontinuous 'fibres' for multiple meso-rod specimen.

For the first casting a 6.35 mm thick aluminum tube (Figure 5.7) was used to encourage proper heat transfer during the curing and cooling stages. The tube was split longitudinally along one side and the internal walls were coated with mould-release to allow post-cure removal. The tube and the spacer assembly are shown in Figure 5.7.

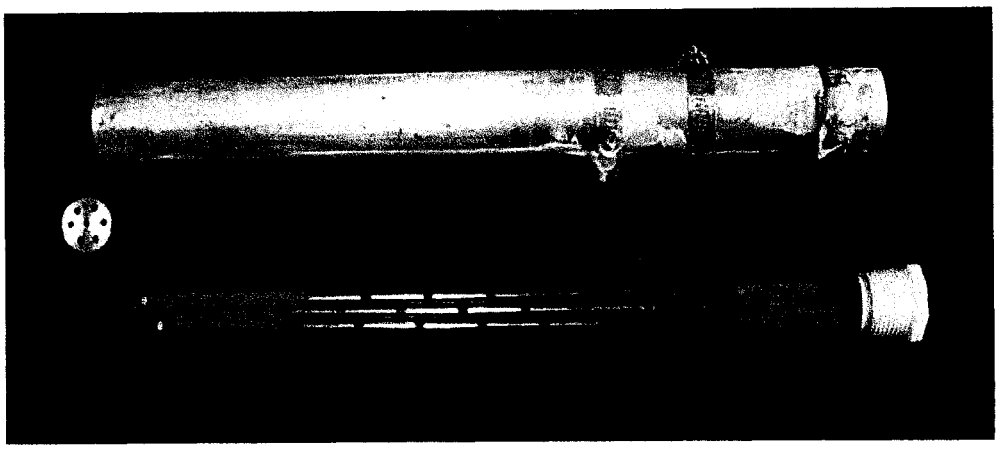

Figure 5.7: Partially assembled multiple strand steel meso-rod specimen

Difficulties were encountered during demoulding that prevented continued usage of this method. A second apparatus was designed and constructed to provide better visualization and handling of the specimen. The new version replaced the aluminum mould with thin-walled glass tubing; the plastic end-cap by an aluminum plug pattern and the fully threaded alignment rods with coated straight rods having threaded ends. A schematic of the assembled set-up is shown in Figure 5.8. An exploded view is given in Figure 5.9 including a detailed view of the compression spring to assist sealing of the steel fibres and plastic spacing tubes.

Figure 5.8: Schematic of revised multi-strand steel meso-rod specimen with glass mould and predefined break at the centre. An exploded view detailing the sealing mechanism is shown in Figure 5.9

One half of the resin was poured into the bottom mould and allowed to cure. A thin layer of wax was applied to the surface of the cured resin (Figure 5.10). When the wax had dried, the second half of the rod was poured (Figure 5.11). This procedure was designed to produce a very thin, uniform discontinuity across the cross section of the specimen to simulate the smallest crack width that might traverse an FRP rebar. Removal of the complete casting from the mould required breaking of the glass tubing.

ITEM NO.	QTY.	PART NO.
1	1	Pattern base
2	7	alignment rod
3	98	spacer
4	49	fibre
5	7	Riser
6	7	Compressior spring
7	7	washer
8	7	spring
9	7	nut
10	1	Alignmment plug
11	1	Glass mould
12	1	No 6 Stopper
13	1	Glass mould

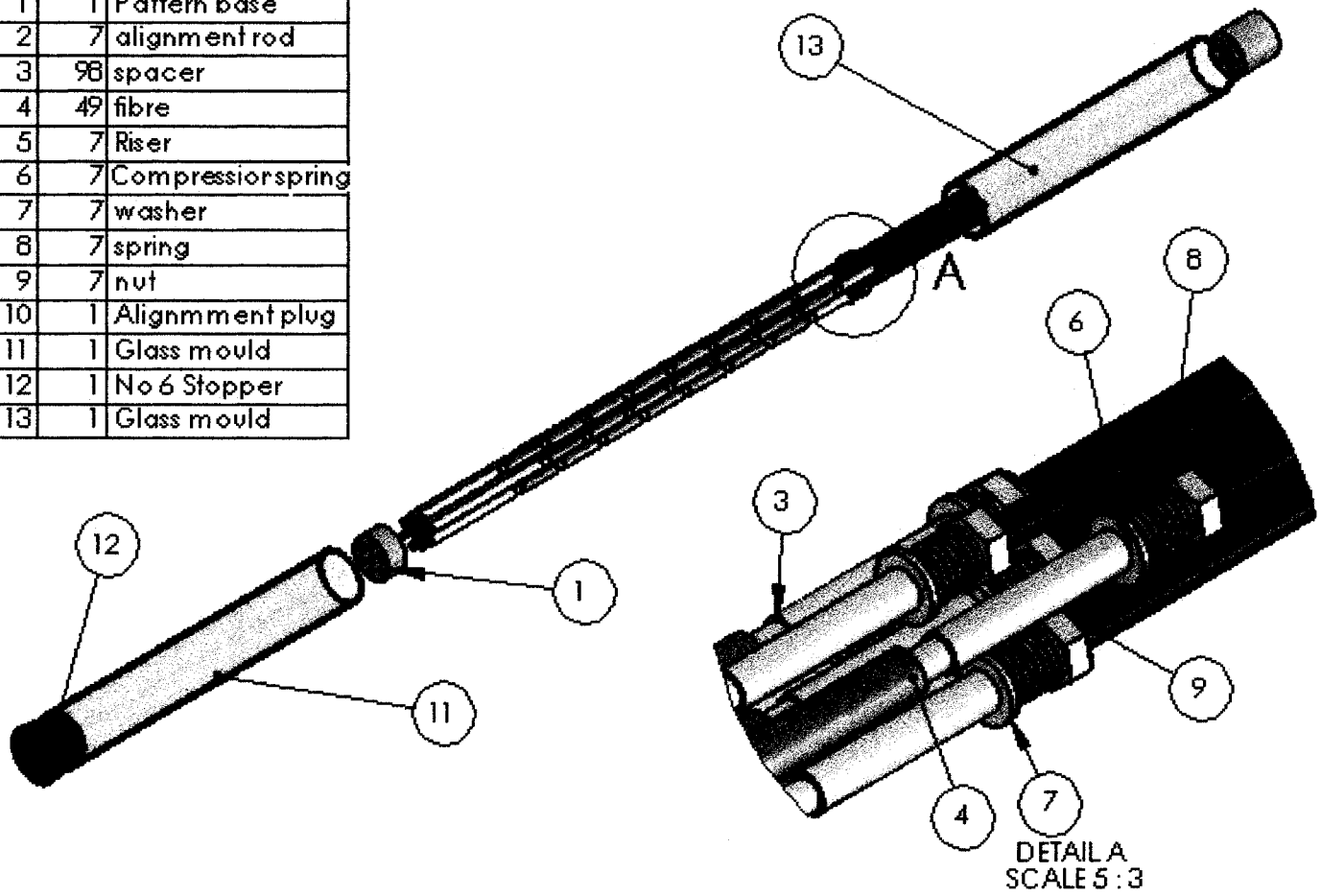

Figure 5.9: Exploded view of multiple strand assembly with glass mould and detail view of compressive sealing system.

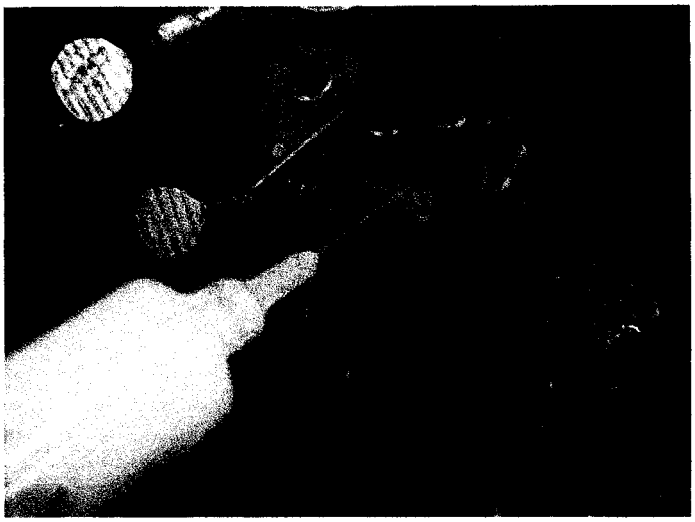

Figure 5.10: Application of wax interface between halves of the casting using a syringe. Care was taken not to deposit wax on the 'fibre' surfaces.

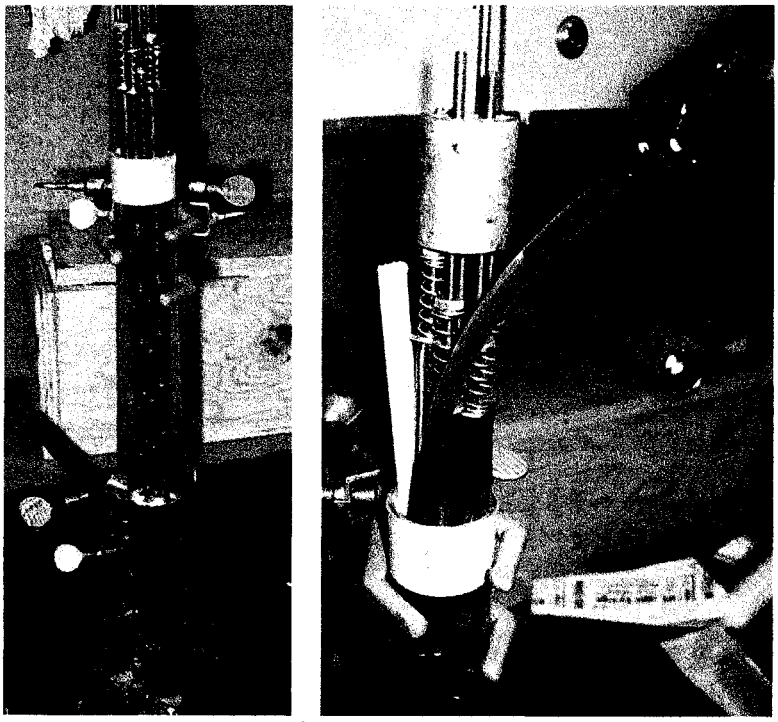

Figure 5.11: Assembly of 2nd stage (left); pouring of 2nd stage resin from bottom up using syringe and tubing.

The completed specimen was potted in steel end tubes as in prior tests and tested in tension on an Instron 4482 machine at a rate of 10 mm/min. The load-displacement plot is presented in Figure 5.12.

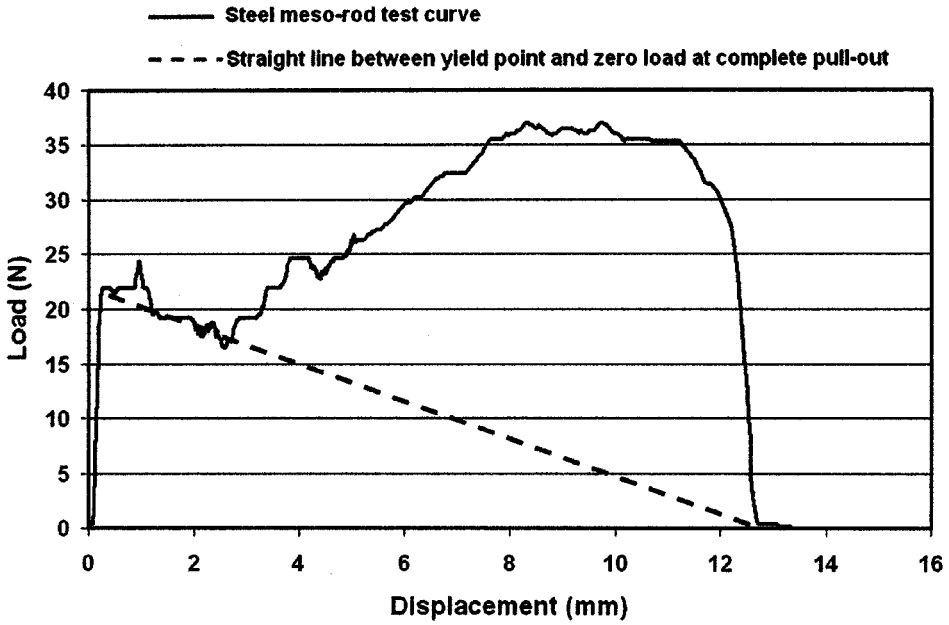

Figure 5.12: Pull-out test plot for the multiple strand steel meso-rod. Sustained load is evident at large displacements and increases to a maximum load higher than initial yielding.

The active initial combined length of spacers was approximately 54 mm. Using the previously measured interfacial shear strength of 660 kPa, an initial load at the onset of pull-out of 628 N is predicted. The large difference between this load and that observed during the test could be due to a number of factors. Firstly, the relative positioning of the spacers proposed in Figure 5.4. was not achieved as desired. The intentional crack followed a random path across the cross section, running lengthwise along several fibres and traversing the space between inline fibres. Secondly, only a portion of the spacers was active during loading. That is, due to the random path of the crack, the surface area of fibres acting during pull-out was less than required to meet the load – this was also due in part to resin cracking during removal of the specimen from the mould and more significantly during removal of the alignment rods. At the most, only three of the seven steel meso-rods contributed to the load carrying capability of the rebar. The low experimental result could also

be due to an interfacial shear stress well below 660 kPa.

The surface finish of the spacers used in the test had a much higher sheen than the dowel pins in the interface tests. In addition, the melting temperature of the wax was exceeded during curing. As a result, the wax travelled along the interface between the resin and the inner surface of the glass tube (Figure 5.13) It is possible that the wax also travelled along the outside of the steel spacers substantially reducing the frictional shear stress. Future specimens should use a high temperature grease or mould release.

Although the observed loads were significantly below the prediction (predicted maximum load - 1024 N; maximum actual load - 36 N) the initial portion of the curve profile shows the behaviour of a typical pull-out test (dotted line) up to approximately a 3 mm extension. After that point, the curve rises steadily and linearly to a load approximately twice the initial 'yield'. The reasons for this behaviour are not known at this time. However, the brittle resin shows some evidence of small chipping which may indicate particle interference to slip of the meso-rods.

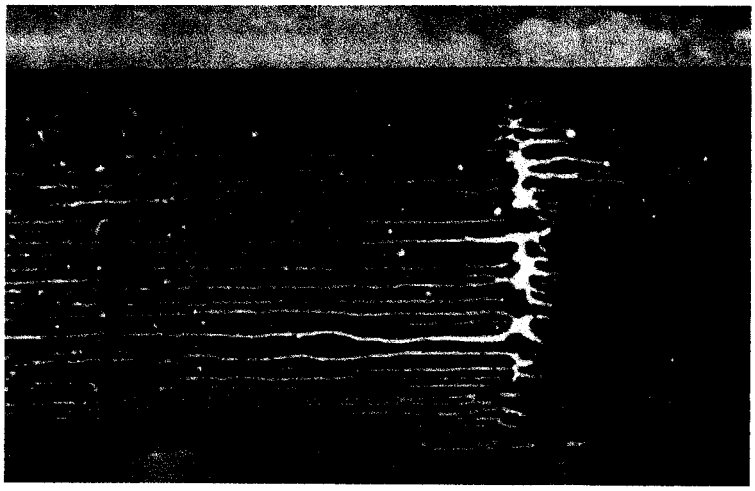

Figure 5.13: Close-up of 'crack' joint (white). Traces of mould release appear axially on the specimen surface.

5.1.2 Continuous/discontinuous, multiple carbon fibre composite meso-rod design

In the steel-spacer meso-rod concept test, a sustained load during pull-out occurred. This led to the production of two prototype carbon continuous/discontinuous meso-rod rebars. The rebars were designed and constructed as described below.

5.1.2.1 Design/manufacturing process

Without the benefit of highly a controlled process, such as pultrusion, to manufacture the rods the design and manufacturing of the specimens were governed by available materials and processes and were simultaneous.

The multi-step process is:

1. Assume the fibre type, resin material and the number of fibre tows per meso-rod

The first specimen, 1-MJ60-E/S-21-E/T[1], used a single 12,000 fibre tow of Torayca MJ60B high-modulus carbon. The second specimen, 2-MJ60-Ep/A-22-Ep/A used two tows lightly twisted together to produce a length of 24,000 fibre single tow. In each case, the tow was strung on a fixture as shown in Figure 5.1 to produce pre-tensioned segments. A resin was then manually applied to the fibres by syringe deposition. The fibres were then drawn between two fingers[2] to force the resin into the fibres. This was repeated for a total of three applications each until the fibres were fully impregnated and encapsulated by a thin resin coating

The two samples used different resin systems:

- 1-MJ60B-E/S-21-E/T: East Systems epoxy with a mix ratio of resin to rapid-cure hardener at 5:1. Curing was at room temperature for 24 hours.
- 2-MJ60B-Ep/A-22-Ep/A: Shell Epon 825 resin with 1482 Ancamine hardener at a mix ratio of 100:19. Curing was at 114 deg. C for 90 minutes.

After curing, the segments were cut from the fixture in lengths of 490 mm. The resulting segments were high-quality rods having generally constant cross section and a smooth, glassy surface finish.

---

[1]The specimens are numbered as *# of tows – fibre type – resin system for tow (E/S: East Systems; Ep/A: Epon/ancamine) – rod count – resin system for rod (E/T: Epothin)*

[2]Powder-free latex gloves were worn to prevent transfer of natural oils to the system.

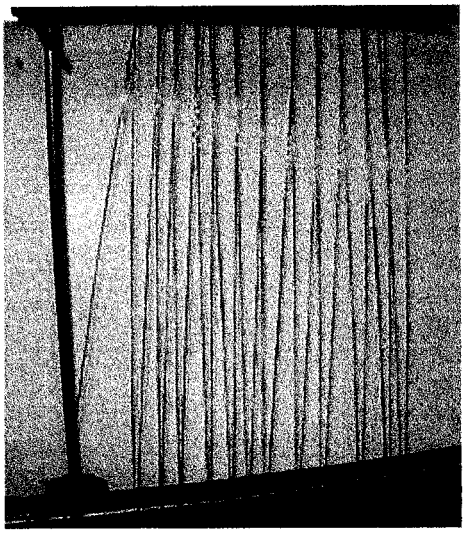

Figure 5.14: Fibre stringing and curing rack.

2. *Determine the volume fraction of continuous meso-rods using Equation 5.3.*

$$V_f = \frac{\dfrac{(Tex)\times(Tow\ count)}{\rho_f}}{\dfrac{\pi}{4}\phi_{rod}^2} \tag{5.3}$$

where *Tex* is the weight, in grams, per 1000m of a fibre tow,

Tow count is the number of fibre strands,

ρ_f is the mass density of the fibres, and

ϕ_{rod} is the average measured value of the fabricated meso-rod.

The meso-rod diameters and resultant V_f are given in Table 5.1.

Table 5.1: Diameter and volume fraction of continuous carbon meso-rods.

Specimen	No. of meso-rods	ϕ_{rod} [mm] (15 sample average)	V_f [%]
1-M60JB-E/S-21-E/T	21	0.994 ± 0.125	13.8
2-MJ60B-Ep/A-22-Ep/A	22	0.958 ± 0.102	29.6

The volume fractions are low due to the nature of the resin application process. A controlled pultrusion using a die may produce volume fractions up to 80% though similar ranges are not necessary. Specimen 2-MJ60B-Ep/A-22-E/T exhibits a much higher density at a similar diameter due to the use of twice as much dry fibre and the much lower viscosity of the Epon resin system at elevated temperature, relative to the RT East Systems resin. This allowed greater penetration into the fibres during the cure cycle.

2. Calculate the elastic modulus and ultimate strength of the individual carbon rods from ROM (Equation 2.1)

3. Calculate the volume fraction of carbon-rods in the rebar

$$V_{m-r/rebar} = \frac{(No.\ of\ meso-rods) \times \phi^2_{m-r\ (ave)}}{\phi^2_{rebar}} \tag{5.4}$$

where $V_{m-r/rebar}$ is the volume fraction of meso-rods in the rebar.

4. Calculate the critical length of meso-rods and adjust segment length for assumed magnitude of debond force

Knowing the volume fraction, dimensions of the rods and strand count and assuming a conservative estimate of 10 MPa for interfacial shear stress from earlier work, the required lengths of the discontinuous portions were determined using Equation 5.1 (Table 5.2, 1). Referring to Figure 5.15, two alternatives for creating the hybrid continuous/discontinuous rods were available. In the first, continuous fibres run through the core of the hybrid; for the second, the continuous fibres run along one side of the rods. The second alternative was chosen for relative ease of manufacture.

Table 5.2: Material properties for carbon meso-rods

	1-M60JB-E/S-21-E/T	2-MJ60B-Ep/A-22-Ep/A	Eqn. No.
length, meso-rod (nom.)	5 mm	11 mm	4.1
E, meso rod	49 GPa	41 GPa	2.1
σ_{max}, meso-rod	278 MPa	587 MPa	2.1
E, rebar	30.1 GPa	42.4 GPa	5.5
σ_{max}, rebar	202.8 MPa	216 MPa	5.6

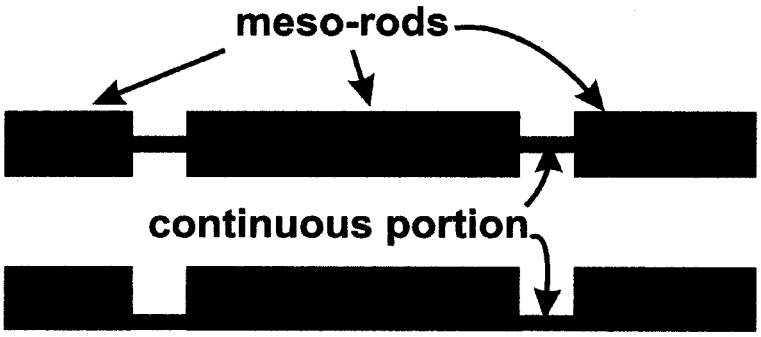

Figure 5.15: Proposed alternatives for continuous/discontinuous hybrid strand: a) continuous fibres form the core of the hybrid strand, b) continuous located on the perimeter of the hybrid strand.

To produce the continuous/discontinuous hybrid system from the rods, a fine-toothed saw was used to cut through the cross section at the lengths given in Table 5.2, 1. The saw was drawn with continuous pressure in one direction to produce consistent depth and quality of cut. Figures 5.16 and 5.17 show the cutting procedure and a side view of a segmented rod, respectively.

A length of 170 mm, located centrally, was segmented for each rod. It was not necessary to segment the entire length of each rod as all but a 70mm central gauge length would be unbonded during testing providing 50 mm for a clip-on extensometer with 10 mm clearance at each end.

Figure 5.16: Partial cutting of carbon rods.

Figure 5.17: Close-up of partially segmented 2-MJ60B-Ep/A-22-Ep/A rod showing depth of cuts at 40-60% of diameter.

5. Determine contribution of meso-rods to elastic modulus using Halpin-Tsai (Equation 4.5)

The meso-rod lengths were calculated knowing the volume fraction of the rods and assuming the interfacial shear stress at onset of pull-out to be 40 MPa. An area ratio of 1:1 was selected for the discontinuous/continuous portions, that is, cuts would be made into the rods at 50% of the diameter, and the maximum pull-out load was assumed to be 40% (from testing discussed in Section 5.2.2) of the debond force. The projected elastic moduli were calculated using the short fibre ROM equation (Equation 4.3) where the meso-rods were treated as the short fibres. Table 5.2, 1 lists the theoretical moduli and maximum strength immediately prior to pull-out, ignoring debonding.

6. Determine elastic modulus, and maximum strength of the rebar immediately prior to debonding considering the volume fraction and properties of meso-rods, continuous fibres and matrix

The ultimate strength of the rod may be calculated using the ROM considering V_f as the volume fraction of the continuous fibres; the meso-rods do not contribute significantly in proportion until the continuous fibres have fractured and pull-out begins. The elastic moduli of the rebars were calculated using the ROM equation modified by the Halpin-Tsai [43] equation (Equation 4.5) to account for the discontinuous meso-rods.

$$E_{rebar} = E_m \cdot V_m + E_{m-r/rebar} \cdot \left(\frac{V_{m-r/rebar}}{2} \right) + E_f \cdot \left(V_{f,m-r} \cdot V_{m-r/rebar} \right) \qquad (5.5)$$

$$UTS_{rebar} = UTS'_m \cdot V_m + \frac{l_c \cdot \tau}{\phi \cdot 0.5} \cdot \left(\frac{V_{m-r/rebar}}{2} \right) + UTS_f \cdot \left(V_{f,m-r} \cdot V_{m-r/rebar} \right) \qquad (5.6)$$

where subscript $_{f,m-r}$ refers to contributions of the fibres within the meso-rods,
subscript $_{m-r/rebar}$ refers to contributions of the meso-rods to the overall rebar, and
UTS'_m is the tensile strength in the matrix at ultimate fibre strain.

5.1.2.2 Assembly of rebar

The 22 meso-rods were subsequently shortened at one end by a random lengths to provide varied positioning of the meso-rods in the assembly as was done in the steel spacer concept model (Figure 5.4), though the relative longitudinal position was not predetermined. The meso-rods were bundled and placed in glass tubes partially filled with another resin; Beuhler Epothin for 1-MJ60B-E/S-21-E/T and the Epon/Ancamine system for 2-MJ60B-Ep/A-22-Ep/A. The glass tubes had an internal diameter of 8 mm (nominal) and wall thickness of approximately 1.5mm. The tubes were previously coated internally with a wax-based release agent.

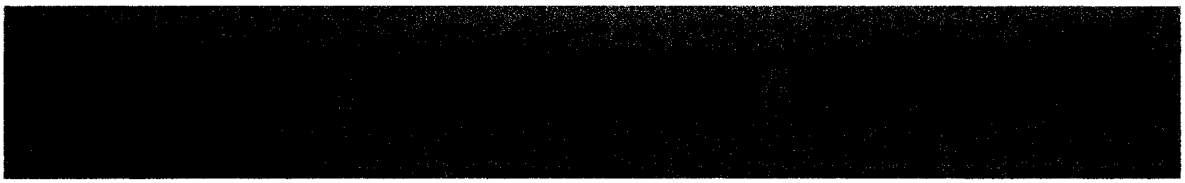

Figure 5.18: 1-MJ60B-E/S-21-E/T rod removed from glass mould. The white PTFE strips demarcate the gauge length containing the continuous/discontinuous structure. (Note - image has been slightly shortened to provide improved visual.)

Rebar 1-MJ60B-E/S-21-E/T was cured at room temperature for 24 hours. Rebar 2-MJ60B-Ep/A-22-Ep/A was cured at 114 deg C for 90 minutes. Following cure and cooling, the glass tubes were broken away from the specimens by light squeezing in a vise and tapping with a rigid plastic hammer. Some surface defects occurred on the 2-MJ60B-Ep/A-22-Ep/A specimen that were caused by coagulation of the wax release agent during the cure cycle. Further specimens should be made using a high-temperature silicon release agent. Minor defects on the other specimen were caused by pockets of vapour unable to escape during cure. Figure 5.19 shows the internal structure of specimen 1-MJ60B-E/A-21-E/T. The epoxy used for this specimen has high transparency.

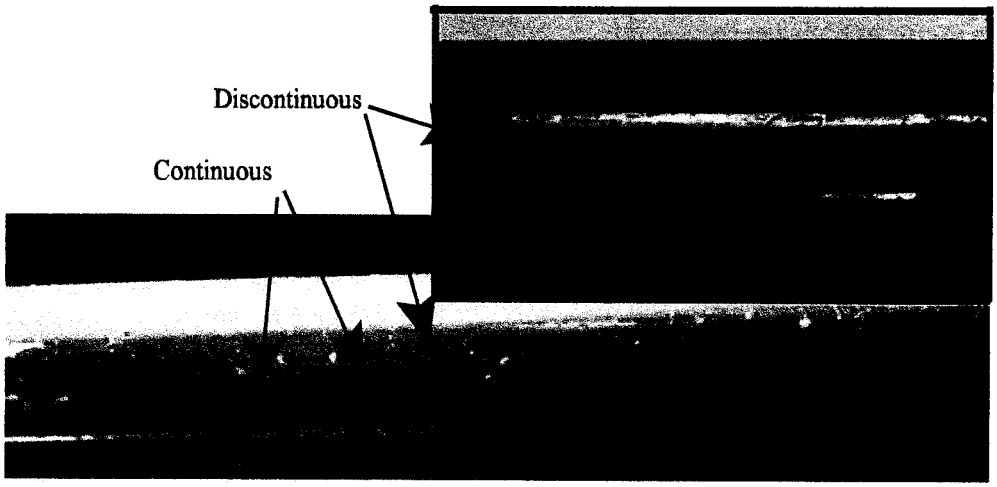

Figure 5.19: Post-cured rod segment showing continuous and discontinuous fibre structure

5.1.2.3 Preparation of rebars for tensile testing

Each specimen was prepared for tensile testing by potting the ends (using MBRACE epoxy system) in internally-rifled 24.5 mm ID steel tubes (see Figure 5.20) with threaded ends for attachment to grips. The ends were sanded with 60 grit paper to enhance anchoring. An unbonded gauge section of approximately 70mm was provided to allow video recording of failure and the attachment of a standard extensometer to measure the elastic modulus.

Two shallow grooves were placed on each specimen at 50mm spacing to permit attachment of the extensometer. A deeper circumferential groove was cut midway between the extensometer grooves to act as a stress concentration to initiate failure.

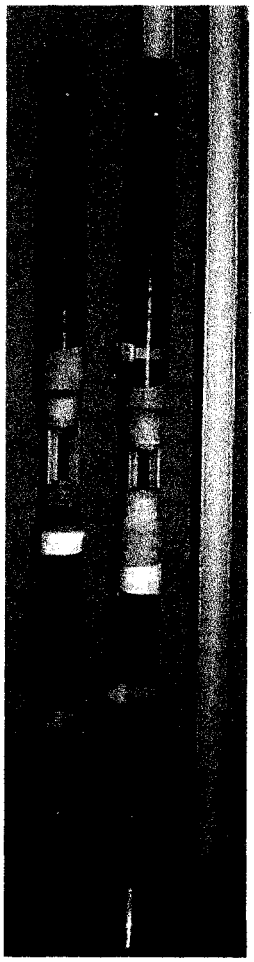

Figure 5.20: Carbon meso-rod rebar potting assembly.

5.1.2.4 Testing method

Each specimen was tested in tension on an Instron 4482 machine using Series IX Instron software at a constant displacement rate of 1 mm/min. Data was simultaneously recorded by the Series IX software and two chart recorders; one for the load-displacement curve and one for the elastic modulus. The extensometer was removed at a strain of 0.1 to 0.2% to prevent damage; the Series IX software used internal calibrations from data prior to this point and applied it to elongation up to fracture.

5.1.2.5 Test results

Load-displacement results of the tests for both specimens are shown in Figure 5.21. A small change in the slope was observed during the test at the point where the extensometer was removed. Elastic modulus calculations r were thus limited to the test region under extensometer control. The predicted and measured elastic moduli and maximum strength for both specimen are given in Table 5.3. The maximum load and elongation were significantly lower than predicted. Both rods failed in brittle tension though the physical characteristics of the failed specimens showed promising features.

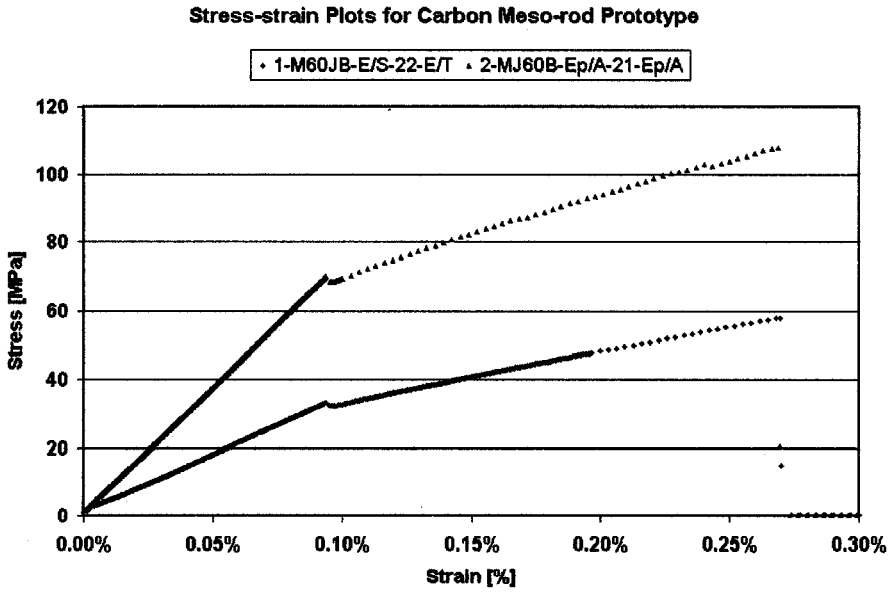

Figure 5.21: Stress-strain plot for carbon meso-rod prototype specimens.

Table 5.3: Elastic modulus results of carbon meso-rod prototypes.

Specimen	$E_{measured}$ [GPa]	E_{theory} [GPa]	$E_{measured}/E_{theory}$ [%]	$\sigma_{max\text{-}measured}$ [MPa]	$\sigma_{max\text{-}theory}$ [MPa]	$\sigma_{mea}/\sigma_{the}$ [%]
1-MJ60B-E/S-21-E/T	22.2	30.1	73.8	57	202.8	28.1
2-MJ60B-Ep/A-22-Ep/A	46.5	42.4	109.7	108	216	50

Figures 5.22 and 5.23 show the mating surface of 2-MJ60B-Ep/A-21-E/T. For each surface, there are several notable characteristics:

1. the meso rod strand fractured at the cut portions as designed,
2. the meso rods themselves did not fracture,
3. the debonding crack travelled along the meso-rods to the discontinuities,
4. the meso-rods protrude from both failed ends,
5. the meso-rods protrude at differing heights, and
6. longitudinal striations appear along the protruding meso rods.

The above characteristics suggest the proper conditions for pull-out. However, interfacial shear stress, interfacial bond strength, manufacturing defects (burring, fibre splitting) at the discontinuities and damage due to debonding may have contributed to the poor result. The controllability of the interface is thus crucial to obtaining desired levels of strength and ductility. The debonding of the adhesive joint between two layers of material may vary from case to case. It would be prudent to remove uncertainty about the debonding and subsequent frictional properties. As the shear strength of a given homogeneous material is typically very repeatable, a known interface, such as a third material strongly adhered to the two mating surfaces would improve the repeatability and performance. A thin layer of thermoplastic material is an example of a potential solution.

5.1.3 Conclusions

Equation 5.5 fairly accurately predicts the stiffness of the meso-rod/continuous fibre hybrid. Equation 5.6 did not, in this case, accurately predict the ultimate strength of the meso-rod bars.

However, the premature failure of the rod prevents a proper assessment of the equation. The frictional shear stress of the interface – affected by surface properties, debond mechanics and cure schedule – was too low to permit the rod to sustain measurable loads after initial failure.

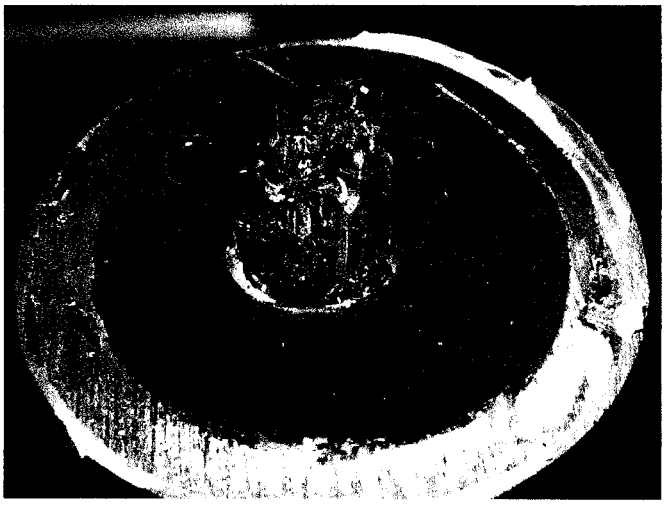

Figure 5.22: Failure of 2-MJ60B-Ep/A-22-Ep/A. Several meso-rods can be seen extending from the resin. Broken out holes from the meso rods on the mating piece are seen at front.

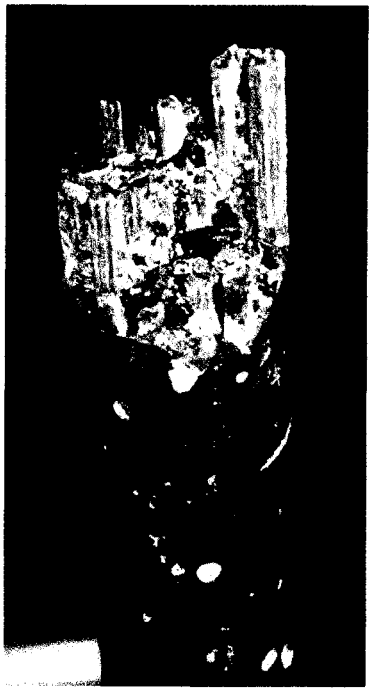

Figure 5.23: Mating portion of Figure 5.22.

5.2 Method B: Discontinuous over-wrap

The second approach to pseudo-ductile failure was based on information from the work of de la Rosa [5]. Several pull-out tests were designed to determine values of τ and the observed pseudo-ductility. The frictional shear stresses of the interfaces between the potting medium/over-wrap, over-wrap/inner core and over-wrap/concrete were required and tensile material tests were conducted for each. A separate component test was designed to verify the progression of failure in the presence of discontinuous over-wrap observed in the previous series of tests.

5.2.1 Interface testing: determination of frictional shear stress.

For the design of the discontinuous over-wrap rebar samples, several tests were designed to determine the frictional interfacial shear stresses during pullout. The specimens are described in the following sections:

5.2.1.1 Over-wrap to potting resin interface test

The test set-up for this specimen is illustrated in Figure 5.24. A 300 mm length of rod was cut from de la Rosa's specimens [5]. The rod was structurally contiguous as was the aramid over-wrap. A test length of 50 mm was chosen to reduce the initial bond failure load, preventing fracture of the rod and the over-wrap/inner rod interface. A 250 mm portion was selected as an anchor on the tension end of the specimen by providing a sufficient surface and to prevent slip from both ends. A gap of 0.5 mm was produced between the grips to simulate a crack through the potting medium and to prevent load contribution by potting resin bridging between the grips. To achieve this, a polypropylene disc was placed over the rod at the junction prior to mounting in the grips. A thin layer of silicone grease was applied to the end of the test section to prevent any contribution to the load by adhesion between the potting resin and the rod.

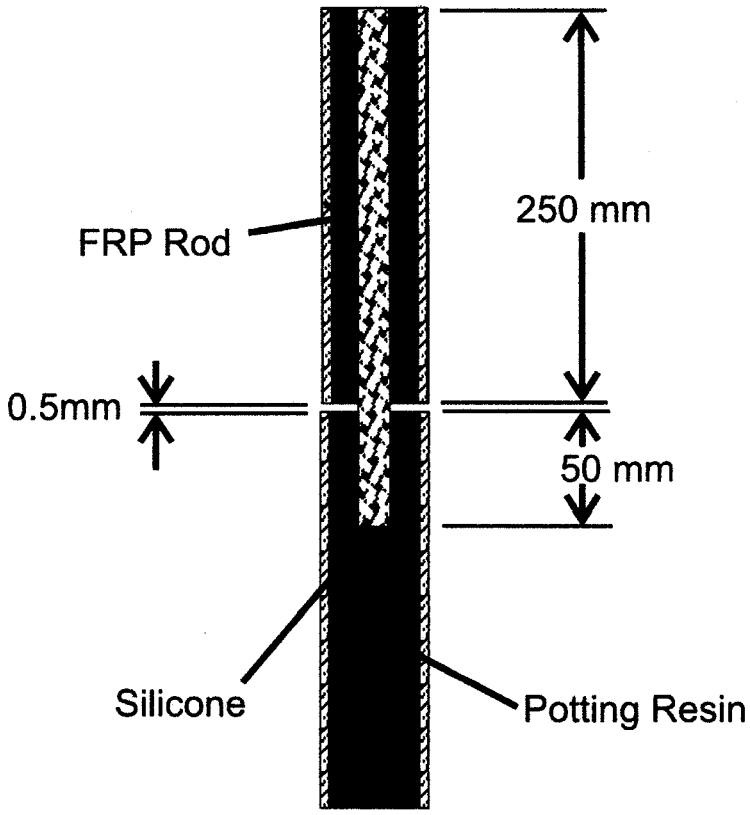

Figure 5.24: Over-wrap to potting resin interface strength test specimen.

5.2.1.2 Over-wrap to inner rod interface test

For this specimen, illustrated in Figure 5.25, the test length was chosen as 70 mm. This required a 320 mm length of rod to match the anchoring of the previous test. The over-wrap was cut 70 mm from the test end, by using a rotating hobby tool fitted with a grinding wheel. The width of the discontinuity was approximately 0.5 mm. The over-wrap was sanded with 80-grid emery paper to increase bonding between the over-wrap and potting resin. All other details of the set-up were as described in the previous test.

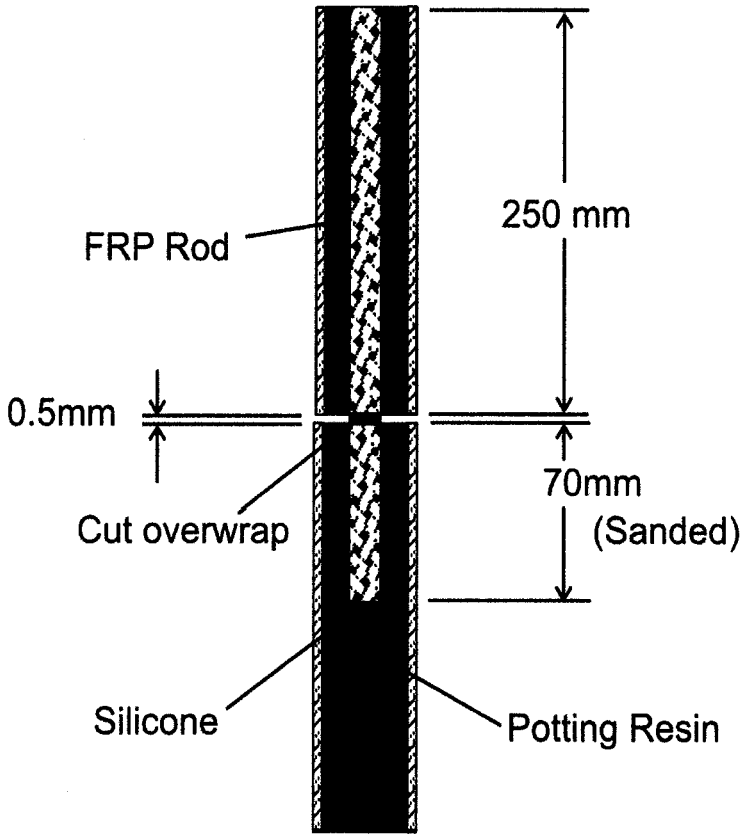

Figure 5.25: Over-wrap to inner rod interface strength specimen.

5.2.1.3 Over-wrap to concrete interface test

The interfacial shear strength of the concrete/over-wrap interface was tested using a test set-up as illustrated schematically in Figure 5.26. The anchoring at the tension end of the specimen was identical to the previous two tests. A 320 mm rod with fully-continuous over-wrap was embedded 70 mm into the concrete. A special grip was produced to decrease the potential for concrete tensile failure. Eight radially disposed anchors were inserted along a common circumference at the base of the grip. The rod was submerged into the concrete and held in position using a retort stand and accessories. Six 18d spiral nails were placed parallel to the rod approximately half-way between the rod and the grip walls in a circumferential pattern. The nails were included to act as small reinforcing bars to prevent concrete tensile failure.

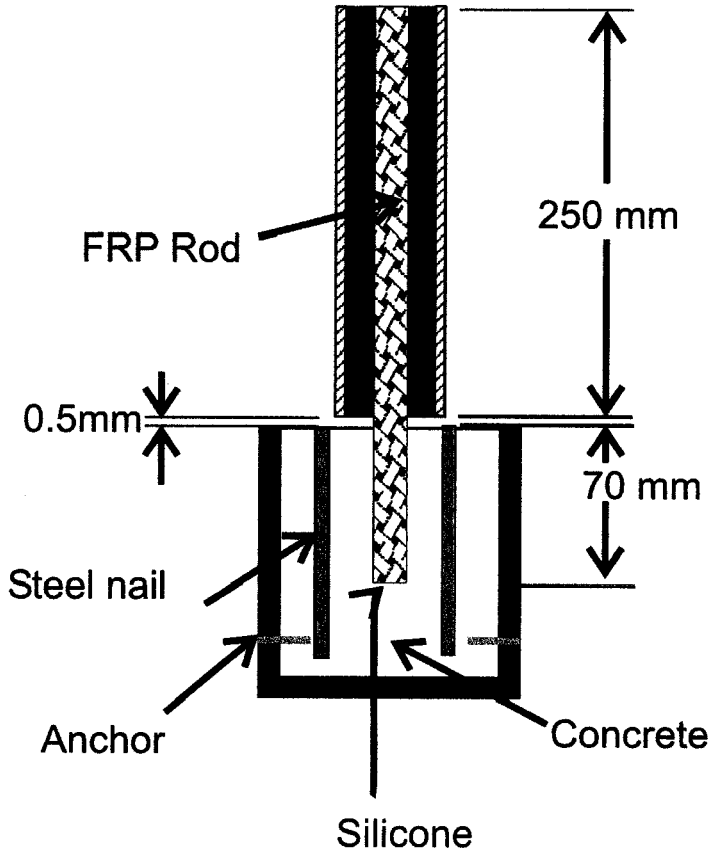

Figure 5.26: Over-wrap to concrete interface strength test specimen.

5.2.1.4 Alignment of specimens

Alignment of the potted rods for each sample was ensured by use of a 15 mm centring pin fit into the core of the inner rod at the longest end and located axially with three screws (Figure 5.27)

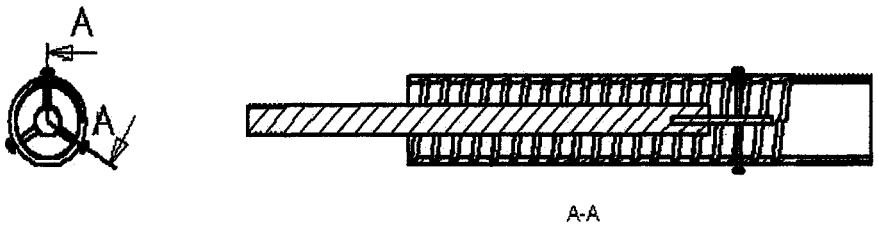

Figure 5.27: Method for aligning anchored end of pull-out specimens.

5.2.1.5 Test parameters

Each of the specimens were tested in tension on an Instron 1332 machine with a constant displacement of 10 mm/min. Figure 5.28 presents the load vs. embedded length plots from the tests.

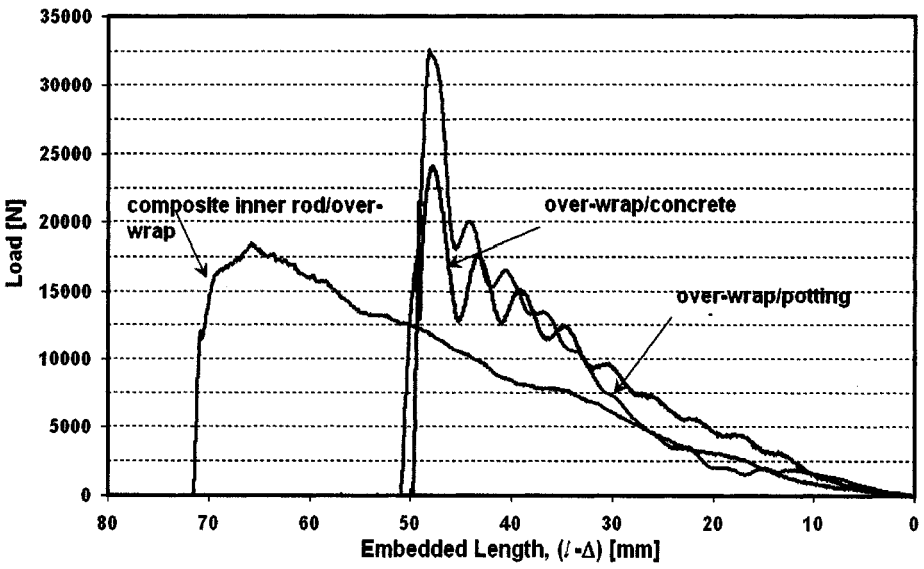

Figure 5.28: Pull-out curves showing relative magnitude of interfacial frictional shear stress in several combinations of media.

The carbon core/aramid over-wrap pull-out test results exhibit classic pull-out behaviour with elastic rise and highly linear decrease during pull-out. As can be seen in the over-wrap/potting medium curves, the pull-out is not uniform; there appears a constant change in the general slope for these and other specimens shown in later chapters. It is generally assumed that the bond-stress is uniform along an embedded fibre or rod and is reflected in Equation 4.2. It is more likely that the bond stress is non-linear along the length of the embedded portion as presented schematically in Figure 5.29. For rod or fibres being pulled out, the variation will likely change, itself, with displacement of the rod, making the prediction of bond stress more difficult. Below the critical length of a rod or fibre, decreasing the load acting on the embedded portions, results in lower strains due to elastic recoil. The slope of the pull-out curve thus decreases as less recoil occurs for the same change in displacement.

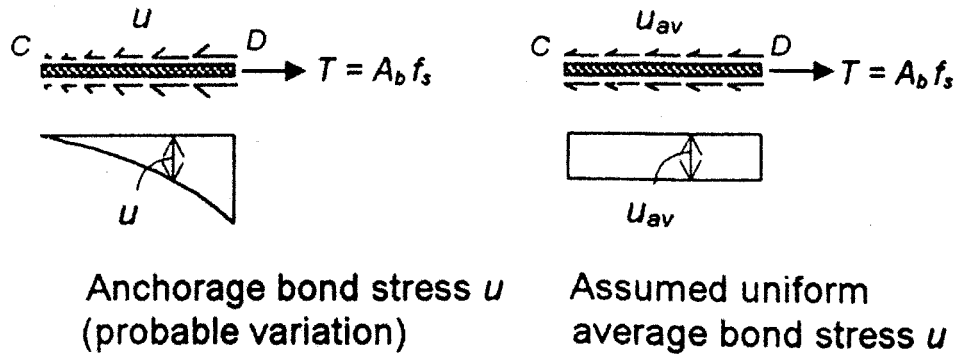

Figure 5.29: Distribution of bond stress along anchored portion of a rod embedded in a medium [44].

As in the tests of de la Rosa [5], and Benmokrane et al [26], undulations are present in tests of over-wrap (manufacture of Kevlar™ braid) to potting medium, confirming the effect of regular braid deformation. The similarity of load magnitude for the over-wrap/inner-rod interface and the over-wrap/potting resin suggest a similar behaviour.

Equation 5.1 and data from Figure 5.28 were used to determine the frictional shear stress at the interface for each of the three tests. The carbon core/Kevlar over-wrap interfacial shear strength was 9.58 MPa. The Kevlar over-wrap/epoxy interfacial shear strength was 3.66 MPa. The Kevlar over-wrap/epoxy interfacial shear strength was 5.5 MPa.

The values given here are average values for sample points from each specimen. The sample

points were taken at the intersection of the pull-out curve and a best fit line between the highest load at the onset of pull-out and a pull-out distance equal to half of the original embedded length. In each case, the shear strength decreased with increases in pull-out.

5.2.1.6 Multiple discontinuous over-wrap component test

A fourth test was conducted to test the concept of an over-wrap which is cut at regular intervals. It was not intended to generate material information. Instead, it was an observational attempt to induce a Type II failure with a repeatable pattern of precut over-wrap. This would verify and extend the mechanism of failure observed in de la Rosa's [5] tests. The specimen, illustrated in Figure 5.30, consisted of a solid unidirectional CFRP core covered by a series of 100 mm lengths of braided aramid over-wrap separated by a 2 mm circumferential gap. The cuts were formed by the use of a hand-held grinding wheel. The specimen was anchored at both ends and a gauge section 0.5 mm long was provided between the anchors. The specimen was positioned in the anchors such that the gauge section was located at the midpoint of the central over-wrap segment.

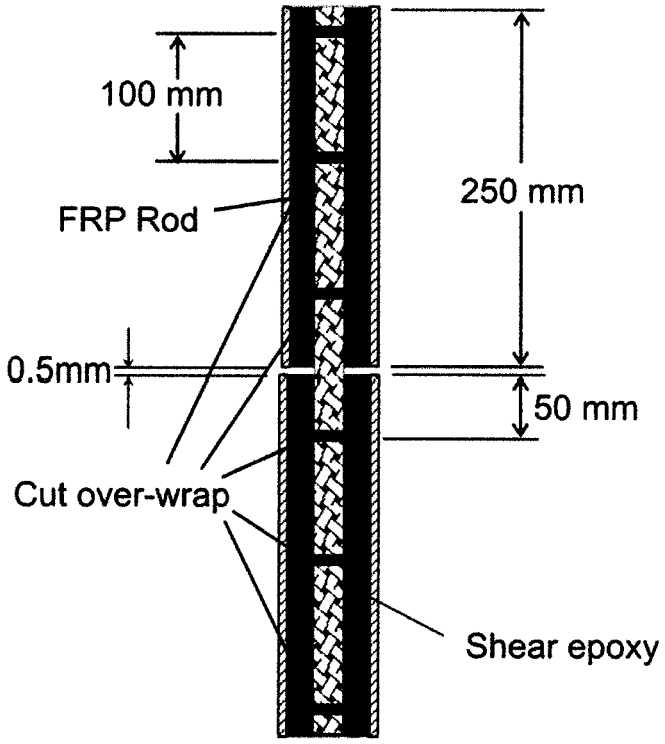

Figure 5.30: Carbon core/Kevlar over-wrap component test specimen.

The load versus displacement curve, provided in Figure 5.31 shows similar characteristics with SP8 and SP14 of de la Rosa [5] (see also Figures 3.2 and 3.3). The initial elastic rise was followed by a sharp drop due to the first debonding. A series of load increases and rapid declines follows again as in Figures 3.3 and 3.2. Finally, the curve exhibits classical pull-out behaviour at a magnitude similar to that of the core-over wrap test in Figure 5.28.

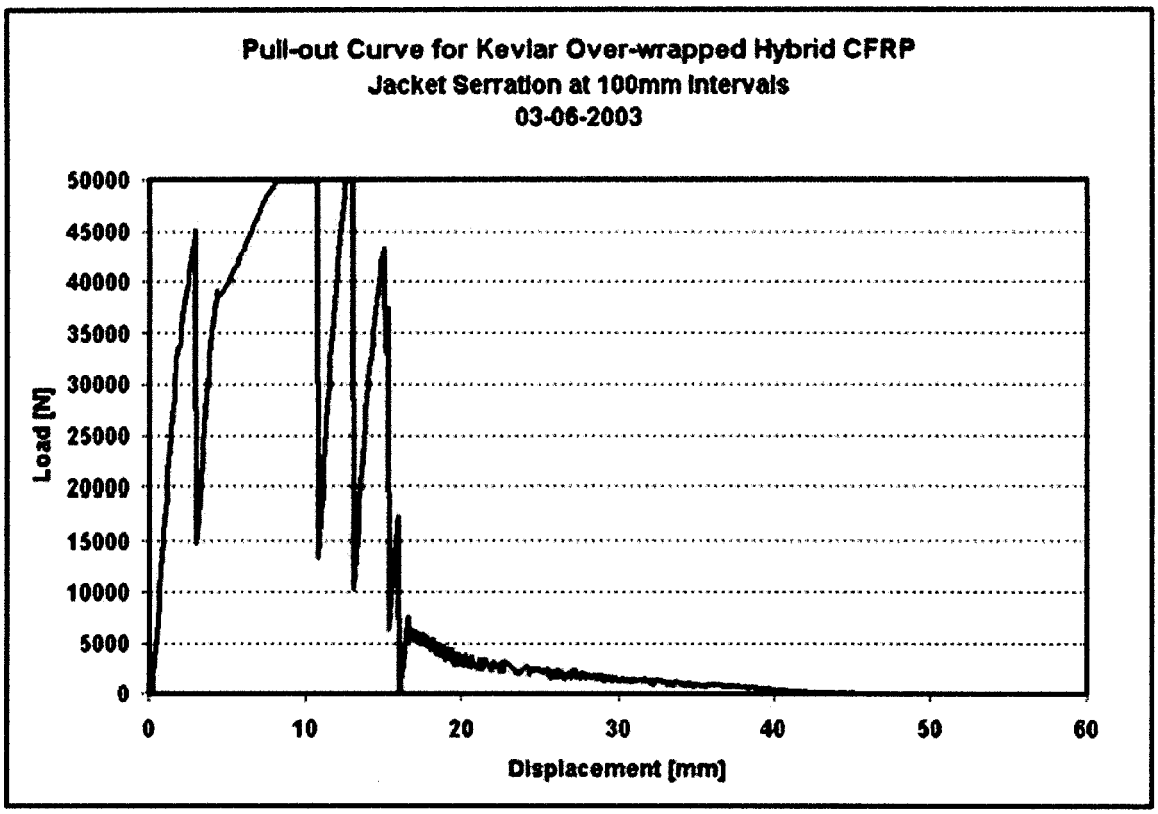

Figure 5.31: Load versus displacement curve for cut over-wrap component test. Note: the load exceeds the limit of the data acquisition unit used in the test.

5.2.2 Steel rebar interface testing

From the materials and component tests, it was evident that a combination of multiple debond stages and friction controlled pull-out could be made to produce rods having high pseudo-ductility. This requires a highly-controlled interface, achieved by the production of a high-quality inner core with constant diameter and constant surface finish. Since the fibre composite inner rod and Kevlar over-wrap were co-cured, the interface between the two had undulations. To this end, steel bar stock was selected for manufacturing concept models.

The steel rebar series was required to test the over-wrap sliding concept using a highly controlled over-wrap/inner rod interface; the nature of the carbon inner rod manufacturing process described later prevents, at this time, accurate and repeatable interfacial frictional shear strength whereas the surface of steel rods can be controlled with relative ease.

To this end, several pull-out tests were designed using a variety of surface treatments. Figures 5.32 and 5.33 show, respectively, a schematic and photo of the first three series of surface treatments, each over a length of 150 mm from one end:

- three specimens respectively sanded circumferentially to: 60 grit; 240 grit; 800 grit followed by polishing with 0.3 μm wet diamond powder,
- high-pressure sand blasted to a roughness approximately equal to 150 grit sandpaper,
- lightly threaded with a ½"-13 tap to a depth of a few thousands of an inch.

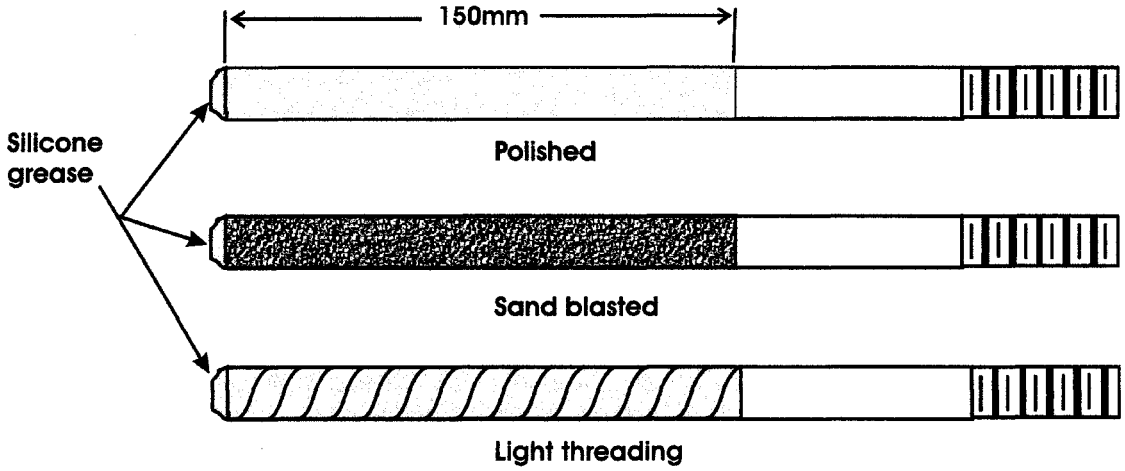

Figure 5.32: Schematic of surface finish for pull-out specimens

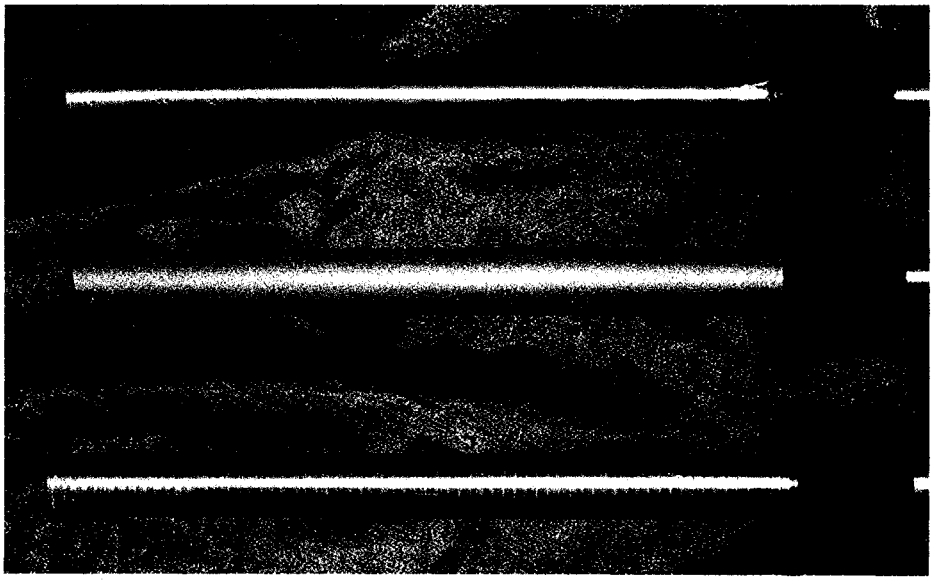

Figure 5.33: Steel pull-out specimens with varied surface finish: 0.3 um polished (top), sandblasted (middle), hand threaded (bottom).

Another set of specimens was produced to investigate the effects of different manufacturing parameters. Shown schematically in Figure 5.34 and in a photograph in Figure 5.35, these involved aramid braiding to check the effect of strand tension against the core, and PTFE (Teflon™) band debond initiators. The PTFE banded specimen addressed the disparity in maximum load required to initiate debond and the maximum available pull-out force. The braid was manufactured over a 120 grit sanded core to a length of 150 mm; over 240 grit sanding and over sandblasting. The later two were braided to lengths of 75 mm.

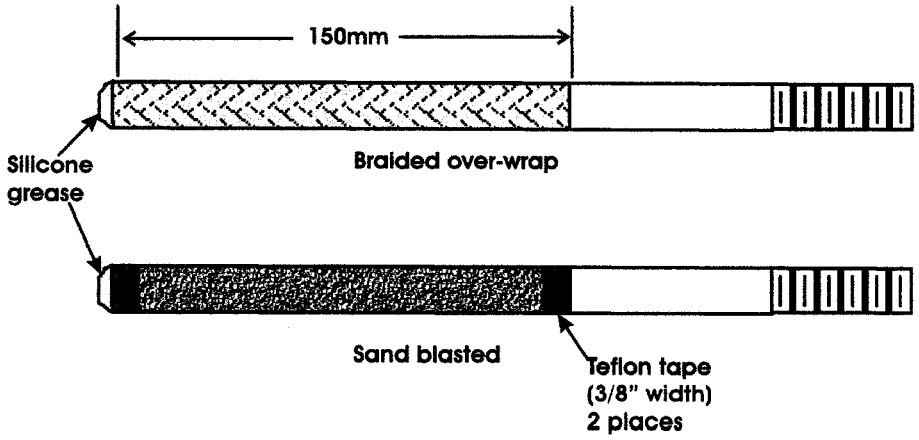

Figure 5.34: Variants of pull-out specimens

All of the specimens were mounted to the extents of the treated surfaces in steel tubes filled with Epon 825 resin system and cured as required. Potting was performed immediately after surface treatment to avoid corrosion which would have altered the surface. Testing was performed at 15 mm/min in an Instron 4482 tensile testing machine. The pull-out plots for the specimens are given collectively in Figure 5.36.

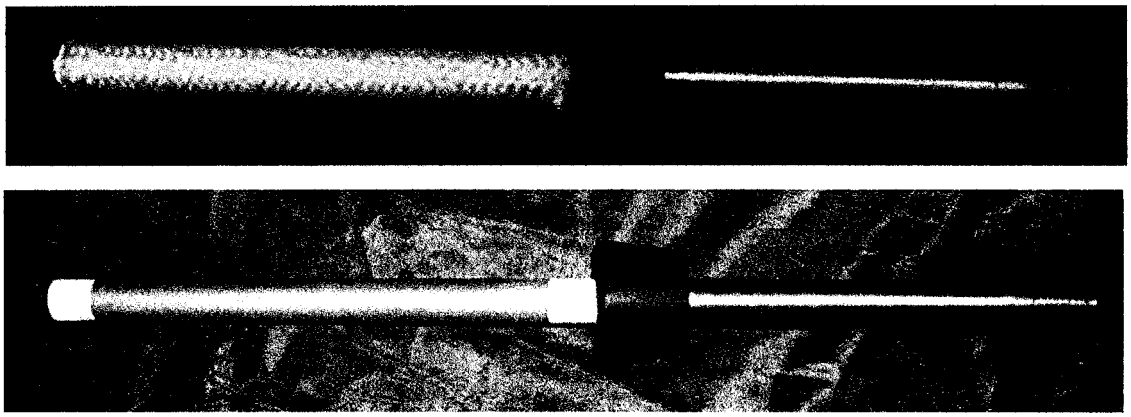

Figure 5.35: Pull-out specimen variants - the PTFE tape is to induce debonding at a lower load.

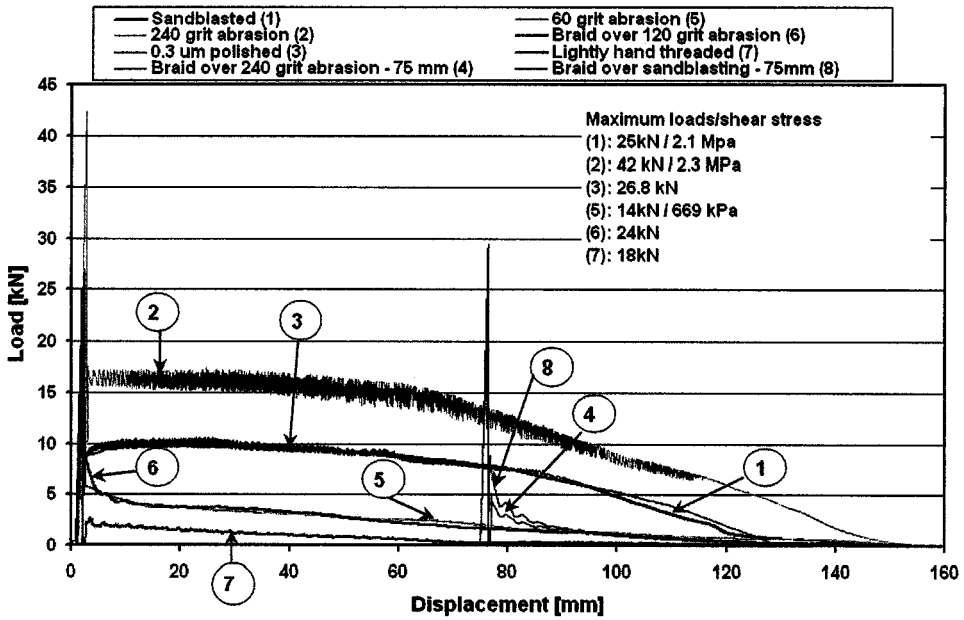

Figure 5.36: Debond and pull-out behaviour for various steel rod surface finishes in Epon 825 epoxy rein systems.

The lightly hand-threaded specimen shows the effects of regular deformities. The small peaks along the plot appear at the same spacing as the threads. The threads may have influenced a higher debond force as the ratio of maximum debond force to maximum pull-out force is highest for this specimen. This suggests smoother surfaces *may* be preferred for actual rebars; cohesion, rather than mechanical keying will provide a less variable pull-out.

5.2.3 Conclusions

Clear conclusions could not be made with respect to the specific surface treatment and pull-out results detailed above. In three instances, nearly identical pull-out behaviour was observed for different surface treatments. Most notable are the 0.3 μm polished and sandblasted specimens. While the surface finishes represent the two extremes, the pull-out curves were identical, appearing approximately midway between the highest and lowest curves. Also similar are the 60-grit sanded, and 120-grit sanded with braided over-wrap. The braid may provide an increase in normal force under axial load thereby increasing the frictional contact between the resin and rod, but this is possibly disproven by the two 75 mm specimens; the extreme difference in surface finish (sandblasted v. 240 grit sanded) is not reflected in the curves as they are very similar. However, the short initial embedded length may have influenced the findings. A minimum 5:1 ratio for embedment-length-to-diameter was necessary as was a length less than that which would result in exceeding the yield strength of the bar. The main conclusions from the tests are maximum interfacial shear stress of 2.3 MPa was achieved, and a given interfacial shear stress can be achieved in a variety of ways.

The following Chapter describes the manufacture of FRP and steel rebar with a discontinuous over-wrap, and the preparation and testing of beams reinforced by the rebar.

Chapter 6: Concrete Beam Preparation and Testing

Two sets of rebars, differing only in the material selected for the core, were manufactured for installation in concrete beams for 4-point loading to test the theory of multiple segment over-wrap sliding. One beam used two over-wrapped low-carbon steel rods, sanded circumferentially with 120 grit sand paper. The 120-grit was chosen as it produced a steady pullout at low loads in the previous tests. It also had the lowest frictional shear stress (660 kPa). Braiding was performed after sanding. A coating of resin was applied to the steel surface immediately prior to braiding. A second coat was applied to the over-wrap prior to cure. The second beam used "pultruded" carbon fibre core with simultaneous braiding. The manufacturing process for these rebars is detailed in the next section.

6.1 FRP Rebar manufacturing

The manufacturing of the carbon core rods, introduced above, required 4 stages:

- core fibre impregnation,
- cross-section formation,
- wet braiding,
- curing.

6.1.1 Fibre impregnation

To produce the inner core of the rods, 80 spools of Grafil XA-S carbon fibre having a thread count of 12,000 per tow, were placed (two tows per spool) on a 20 by 5 spool creel (Figure 6.4).

Figure 6.4: Carbon fibre spool creel.

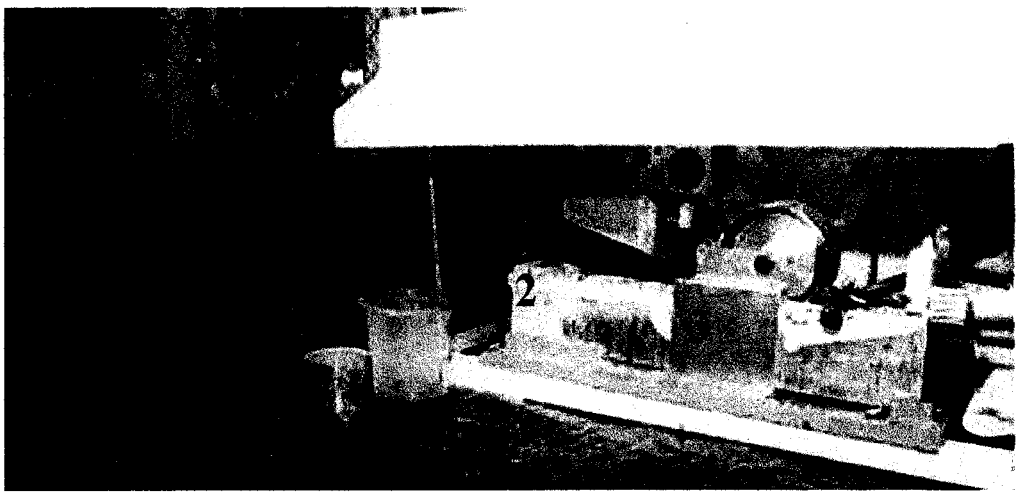

Figure 6.5: Fibres passing through a pre-impregnation forming ring (1) and horizontal separation guide (2) into a heated resin bath (3).

The tows were strung through a ceramic coated aluminium forming ring and then a horizontal separation guide prior to impregnation (Figure 6.5). After the horizontal separator, the fibres passed into a heated resin bath. To encourage wetting, a semi-submerged roller was used to splay the fibres.

At the exit of the bath, the fibres were passed through a nylon forming ring with circular profile similar to the final dimension of the rebar core. Excess resin was squeezed out of the wetted bundle and returned to the heated bath.

The bundled fibres then passed through a Steeger triaxial braiding machine, passing centrally through a formation ring (Figures 6.6 and 6.7). Eighteen (18) strands of aramid fibres were braided over the surface of the carbon fibre bundle. The braid angle was set at 45° from the longitudinal axis of the rod. The interlocking of the aramid strands produces a continuous over-wrap that gives the rod its final size. The aramid fibres are impregnated with resin forced out of the carbon fibres due to braid tension. A coat of resin was added later to wet any dry regions. A pulling mechanism provides the tensile force to pull the tows through the set-up.

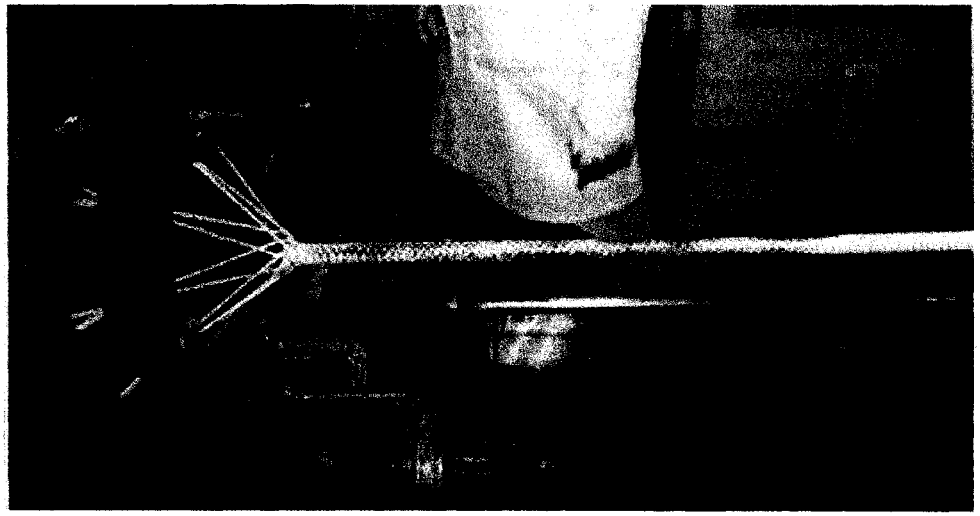

Figure 6.6: Braiding of over-wrap

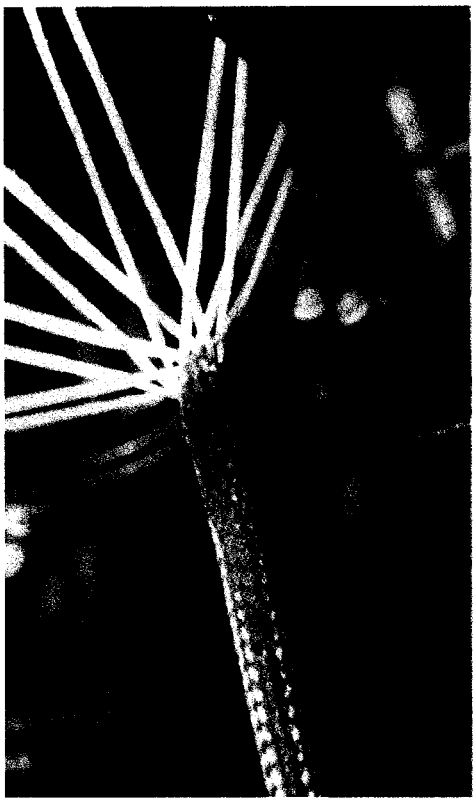

Figure 6.7: A close-up of the braiding of the over-wrap.

6.1.2 Curing

Following impregnation and braiding, the rods were cut to approximately 2m and placed on individual drip/curing racks (Figure 6.8) which were coated with mould release and set on a system of channels to ensure complete drainage of excess resin. The complete system was placed in an oven at 114° C for a duration of 90 minutes followed by open air cooling to room temperature. Figure 6. 6.9 shows a portion of the cured rods.

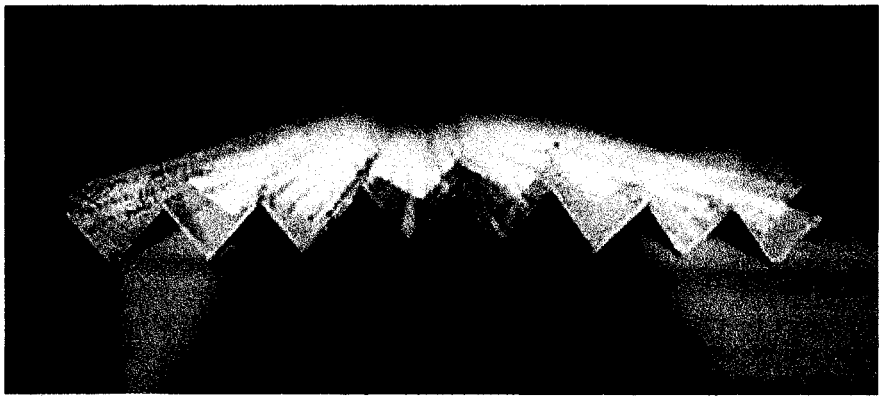

Figure 6.8: Curing rack system: the wire mesh racks, coated with a lubricant, allow excess resin to drip onto the solid channels. The resin then flows along the channel to drain holes where it drips into a basin.

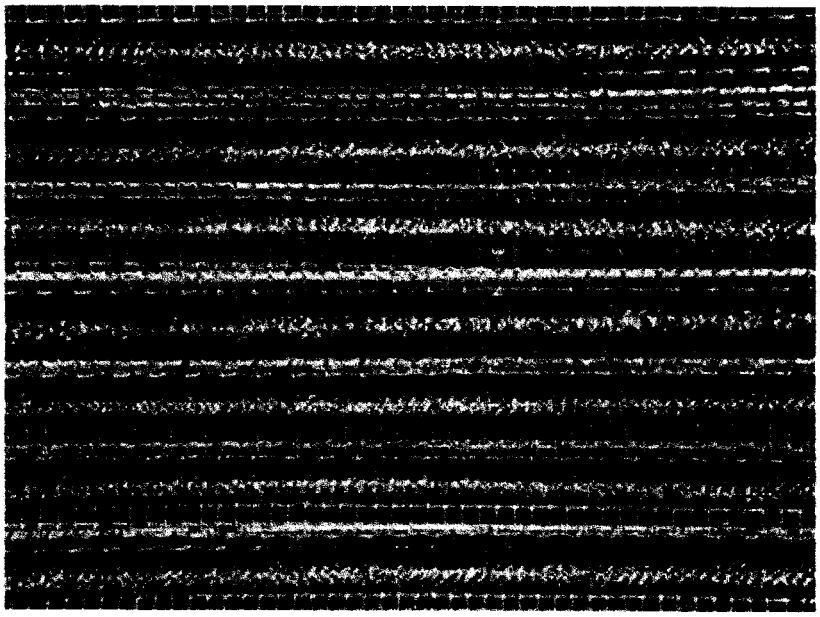

Figure 6.9: Section of post-cured rods on individual curing racks showing surface quality.

6.1.3 Rebar properties

The resulting rods had high stiffness compared to previous rods produced in-house and by commercial manufacturers, a uniform surface finish and a nominal core diameter of 12 mm, yielding a volume fraction of 65.3% (Equation 5.3). The outside diameter, including the aramid over-wrap was nominally 14 mm. ROM predictions (Equation 2.1) were used to calculate the theoretical ultimate strength and longitudinal elastic modulus of the bar (ignoring contributions from the over-wrap); they were 2 113 MPa [239 kN] and 151 GPa respectively[1]. The predicted tensile strength is much greater than the required value of 500-700 MPa for steel while the elastic modulus of 151 GPa is low compared to the elastic modulus of steel. An elastic modulus of 200 GPa is achievable with different carbon fibres.

[1]Experimental confirmation was not performed due to capacity limits on equipment available prior to beam manufacture.

6.2 Concrete Beam Testing

6.2.1 Beam preparation

The braided over-wrap for both the steel and carbon core rods was cut circumferentially at intervals of approximately 38 mm. The cuts were made by rotating the rods against a diamond coated tile saw to a depth equal that of the over-wrap. The cuts were made along the entire length of the rods. Figure 6.10 shows a segment of the steel rods with cuts.

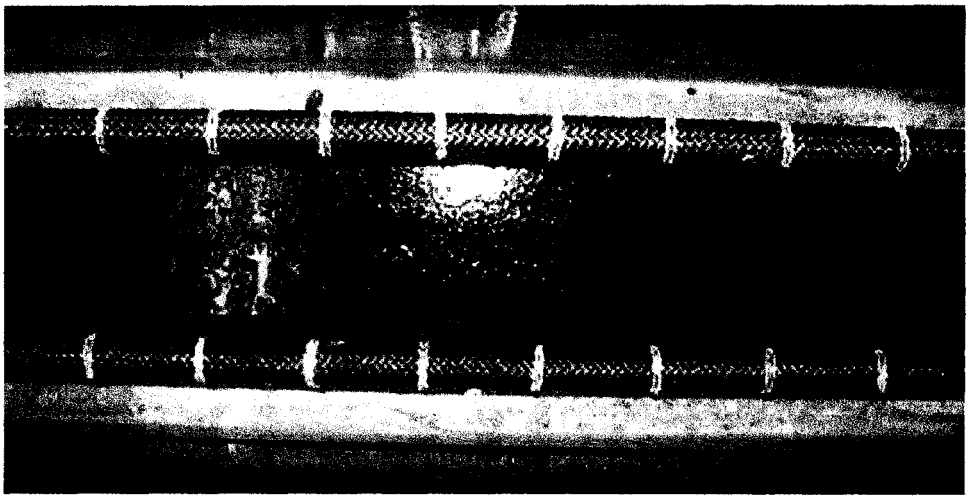

Figure 6.10: Steel/over-wrap system showing 38 mm over-wrap segments.

The completed rods were placed in steel moulds for concrete beams 2000 mm in length with a depth of 260 mm and a width of 127 mm. Laminated carbon fibre stirrups were installed at 190 mm intervals along the beam for shear reinforcement. A 533 mm length of beam void of stirrups was centred along the beam. Concrete was then cast into the mould and allowed to cure a minimum of 28 days.

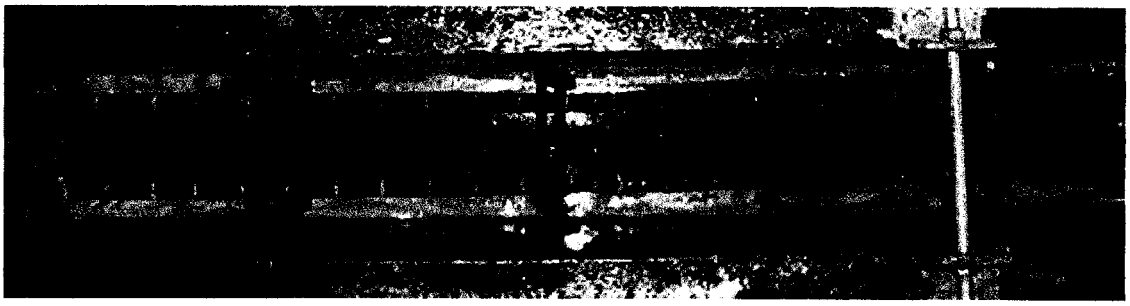

Figure 6.11: 38 mm over-wrap specimens and carbon fibre stirrups ready to be cast.

6.2.2 Beam Testing

The beams were tested in four point bending to provide a constant moment between the two centre load-points spaced 533 mm apart. The load was applied by a hydraulic hand pump feeding fluid to the load points at the top of the beam. The applied load was recorded at one end of the beam under the bottom supports. An LVDT was placed at the on the top of the beam at its mid-span and a dial gauge was placed immediately below it on the underside of the beam to simultaneously record the mid-span deflection. Figure 6.12 shows the set-up during testing of a beam.

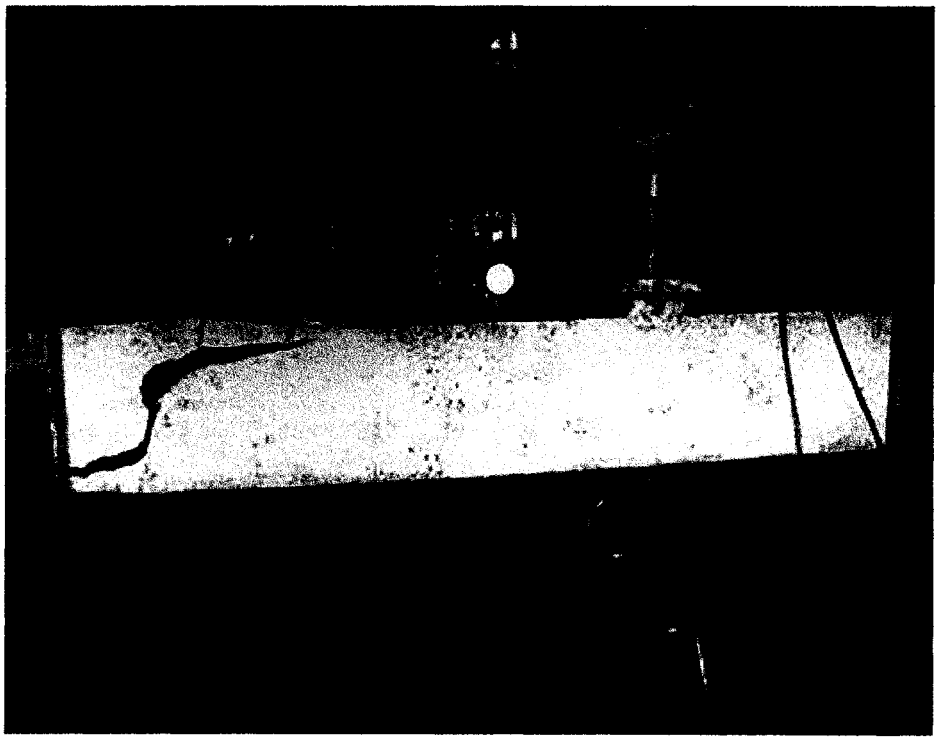

Figure 6.12: 4-point beam test of carbon rod/over-wrap rods in 4 point loading. Shear failure at the stirrups is seen on the left.

The results for the tests are given in Figure 6.13. The beam containing rods having carbon core failed prematurely in shear at a stirrup (Figure 6.12) located outside of the zone of constant moment (between the upper load points). The test was stopped with no evidence of relative sliding of the over-wrap and core of the rod. The beam containing rods having steel core progressed considerably further without significant shear failure. However, the deflection exceeded the limit of the dial gauge. No evidence of relative sliding was present and a multiple shear cracks had developed outside of the upper load points.

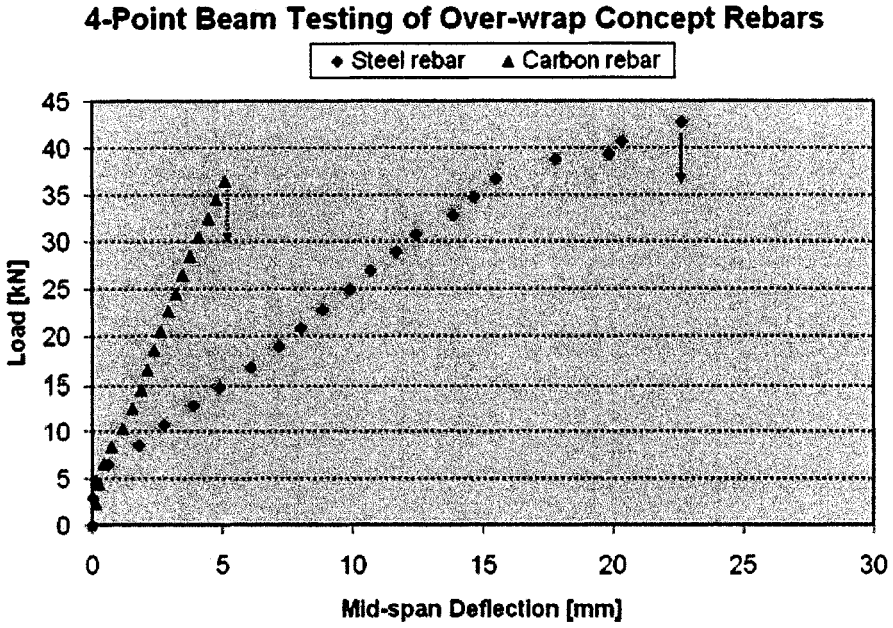

Figure 6.13: Load-deflection data for over-wrap concept rebars in 4-point bending. The magnitude of load is for a single support.

The beams, having failed prematurely in shear at the supports, were retested in 3-point bending using 1 115 mm of the middle span. Steel stirrups were applied externally and close to the supports to improve resistance to shear failure.

The beam reinforced with carbon rebars again failed in shear, exceeding the capacity of the external stirrups. No measurable rod pull-out was observed at the end of the beam. The rod core failed in shear at one support in a brittle manner. A section of unimpregnated fibre at the centre of one of the rods held the beam after failure. The load-deflection curve is given in Figure 6.15.

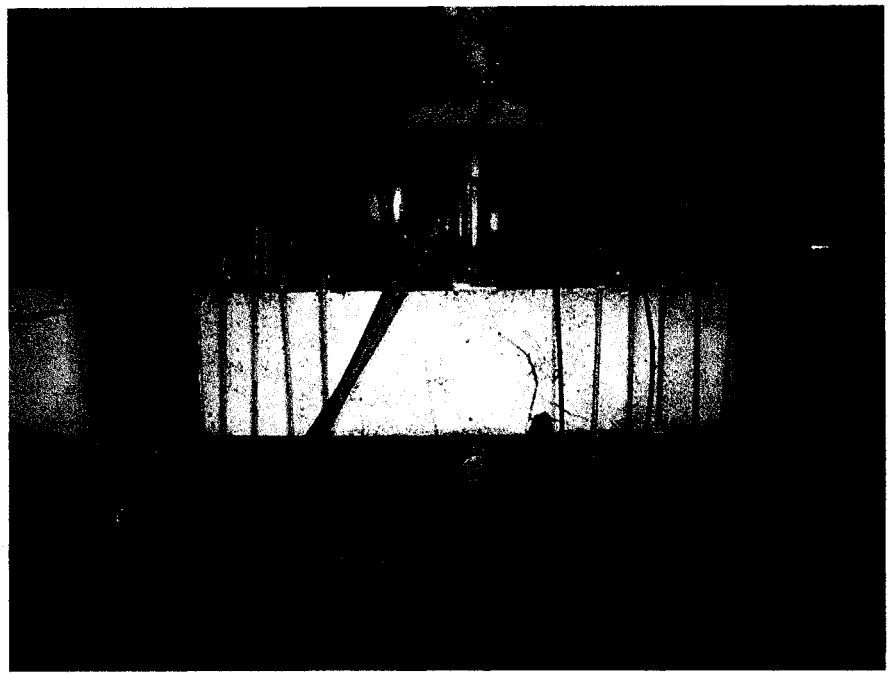

Figure 6.14: Steel rod/over-wrap system under 3-point loading.

The beam reinforced with the steel core/discontinuous aramid over-wrap system exhibited a high degree of pull-out at one end. As seen in Figure 6.15 , the load dropped approximately 33% and was maintained at this level for progressive mid-span deflection. A reading was then taken for every audible release associated with the slipping of the over-wrap over the core. As seen in the figure, this occurred at reasonably even intervals of approximately 1 mm mid-span deflection.

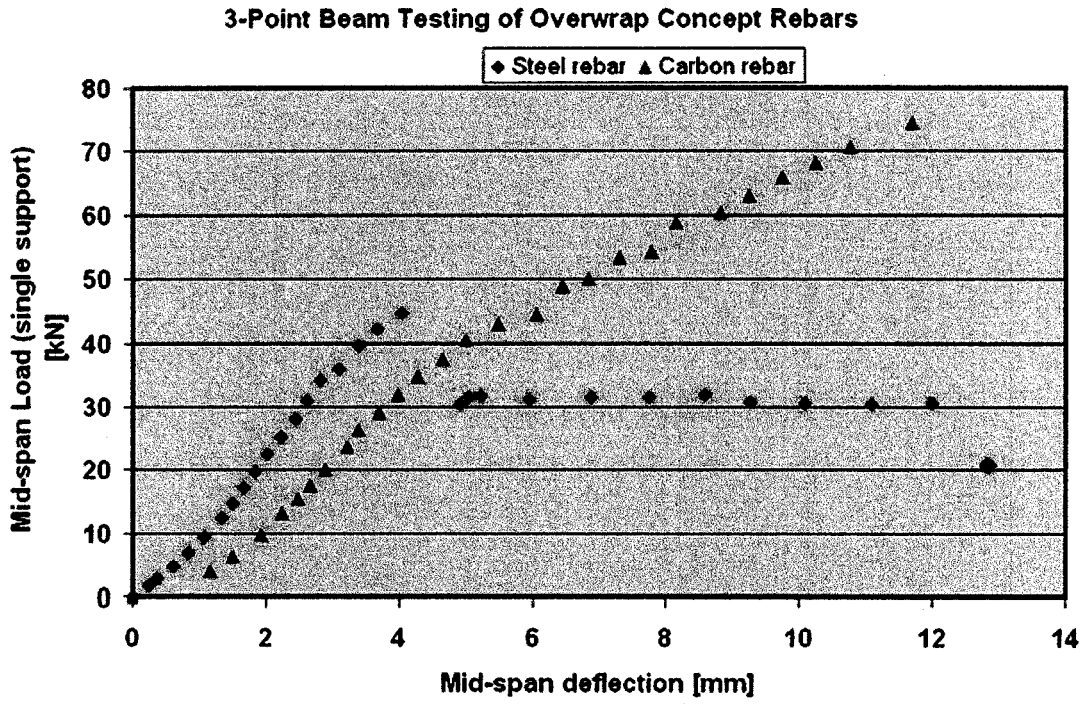

Figure 6.15: 3-Point test plot of over-wrap concept rebars in concrete. The magnitude of the load is from a single support.

Simultaneously, a Mitutoyo™ digital caliper was used to measure the displacement of the end of the rod from its original position, plotted in Figure 6.16 Again, the constant load behaviour is observed. Mid-span deflection was no longer recorded after 12 mm due to limits on the dial gauge. Beyond 14mm of rebar slip from the end of the beam, the load begins to decrease. This is not unexpected as the length of the core carrying frictional shear stress is decreased. The plateau region of the load-displacement plot represents exceptional confirmation of the principle of frictional sliding in two-constituent tensile reinforcement. The behaviour is very similar to that of a steel rebar reinforced beam (Figure 2.2). Figure 6.17 provides photos of the onset of retraction and the position of the steel core at the cessation of the test.

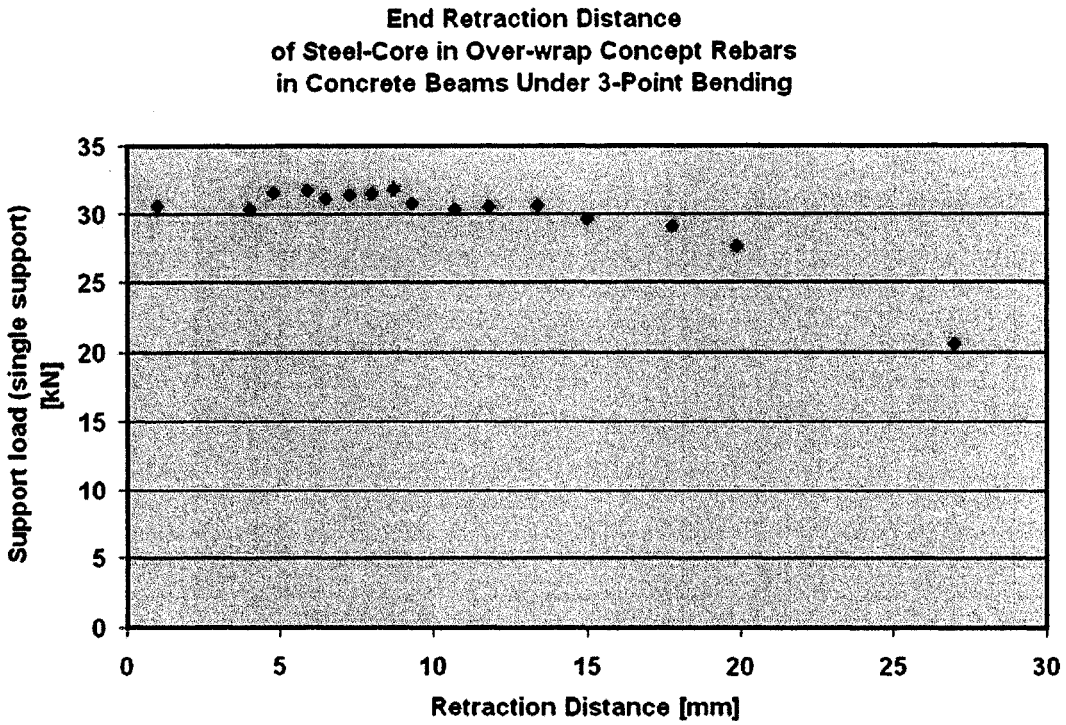

Figure 6.16: End retraction distance of steel core over-wrap concept rebars. Load magnitude is for single support.

Figure 6.17: Progressive movement in rod relative to over-wrap system during increased loading. Images are onset of slip (4mm) and end of test (27mm)

Following the test, the failure surface of the beam was examined. The underside of the beam showed a zone with significant loss of concrete covering and hanging clumps of concrete. These were removed to reveal the reinforcement as shown in Figure 6.18. The lower-left portion of the figure illustrates the sliding of the over-wrap that occurred *within* the beam. The remaining loose concrete was removed to reveal further relative slip shown Figure 6.19. The total increase in spacing between segments of the over-wrap for each reinforcing member correlates closely with the total distance of retraction at the end of the rods, providing further strong evidence of the validity of the over-wrap design. The total length of exposed portions of the steel core of the rebar in the crack zone was approximately 28 mm (left side of Figure 6.18). The rod retracted approximately 27 mm from the end of the beam.

Figure 6.18: Image of failure section of beam showing slip of overwrap system.

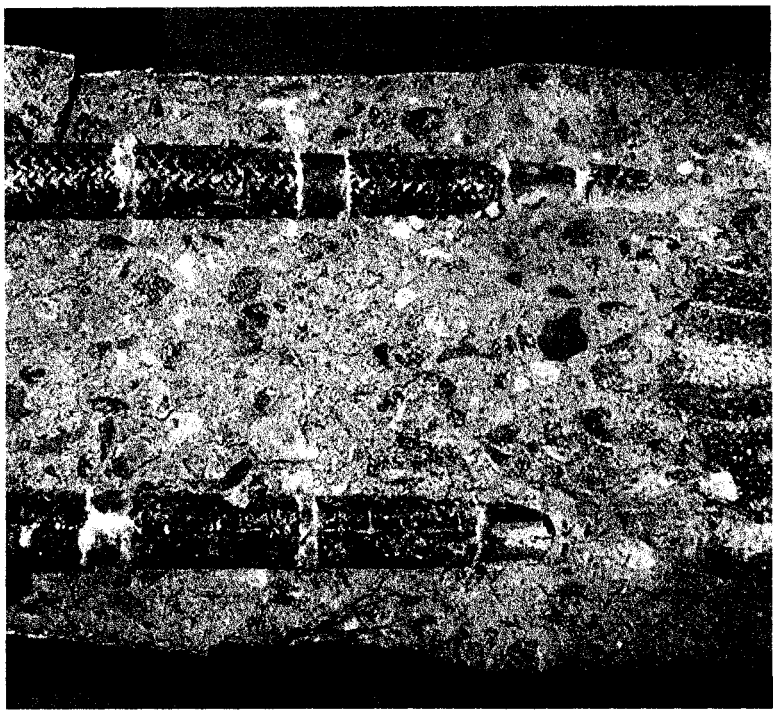

Figure 6.19: Evidence of cumulative sliding of over-wrap segments. The total distance shown here agrees with the displacement of the rod ends (see Figure 6.17).

6.2.3 Conclusions

The test results for the beams reinforced with discontinuous over-wrapped rebar are encouraging. The following conclusions may be made in view of the results.

- The load-deflection behaviour of a beam reinforced with an over-wrapped rod is very similar to a traditionally reinforced beam.
- Interface strength must be high-enough to generate acceptable stiffness in reinforced structures, but also be low enough to allow the inner rod to slip without encroaching on the tensile yield or failure loads of the rod.
- With the correct conditions, total slip distance of the inner rod will be equal to the width of a crack in the damage zone, and
- The manufacturing process for over-wrapped reinforcing rods is simple and may be easily automated and adapted for different reinforcement requirements.

Chapter 7: Comparison of Over-wrap and Meso-rod Ductility Approaches

The numerous experiments and concept models provided much information. While the individual results sometimes produced below expected or design parameters, each displayed some degree of desired behaviour.

The discontinuous over-wrap system with a steel rod embedded in concrete beam showed, exceptionally, the desired multiple debond and slip behaviour. In sustaining a load close to the maximum applied load for large beam deflections, the concept proved effective and viable. What remains is the adaptation to full FRP-cored rods. It may be necessary for the over-wrap to be applied after curing of the central core.

The carbon meso-rod specimens did not show the desired behaviour, but the steel spacer concept model produced a sustained load for the initial portion of the test in accordance with theory. The second portion of the test showed an increased load which is counter to theory and which is, at this time, not understood. The failed carbon specimens show classical fibre failure and pull-out characteristics indicating correct crack mechanics. The interface between the host resin and the meso-rods was of insufficient strength, producing lower than expected loads.

7.1 Properties-based comparison of two methods.

Comparing the two methods reveals clear advantages and disadvantages considering similar overall dimensions, i.e., rebar diameter.

7.1.1 Stiffness

The stiffness of the over-wrap concept will inherently be higher than the meso-rod concept. This is obvious in light of Equations 2.1 and 4.5; the much higher proportion of continuous fibres in the solid inner core elevates the modulus significantly.

7.1.2 Strength

Similarly, the strength of rods manufactured using the over-wrap concept will be higher. The meso-rod concept relies on maximum pull-out load for much of its strength whereas the strength of the over-wrap system is that of either the force required to debond a segment of over-wrap or the product of the fibre strength and the volume fraction.

7.1.3 Global ductility

The concept showing the largest global ductility – defined as the total extension of a rod as a portion of its complete length – is more complicated in the comparison. The mechanism for segmental debond of the over-wrap requires further clarity but it is known that the entire length of rod from a crack to the end of the rod must debond before the ductility is realised. It is likely that the length of discontinuous over-wrap segments depend strongly on the length of the rod and τ.

7.1.4 Local Ductility

The over-wrap system shows little potential for local ductility at multiple locations; the requirement that all of the discontinuous portions must debond before sliding of the rod occurs renders the rod effective only for select locations. On the other hand, the local ductility of the meso-rod concept is limited by the length of meso-rods within the rod. The pseudo-ductile behaviour at a given point is independent of another point along the length. This means that several cracks may simultaneously appear at different points along the rod without negative interactive effects between them and, in the presence of other types of reinforcement (stirrups, dowel bars, tie-wire, etc.), the rods should behave the same.

7.2 Preferred application of the methods

Table 7.1 summarizes the differences in the stiffness, strength, global and local ductility of the two methods. Generally, the over-wrap concept appears the strongest choice for short span structures requiring very high stiffness and can be condensed into a two- or three-stage manufacturing process. The meso-rod concept offers the widest adaptability to varying conditions but requires several more steps to produce a final product.

Table 7.1: Summary of relative properties for meso-rod and over-wrap pseudo-ductility methods

	Meso-rod	Over-wrap
Stiffness	low – limited by length of meso-rods and interfacial shear strength	high – greater V_f of continuous fibres
Strength	low – limited by length of meso-rods and interfacial shear strength	high – greater V_f of continuous fibres
Global ductility	high – cumulation of extension at multiple damage sites	high – rod slips distance equivalent to crack width
Local ductility	high – extension a minimum of half the length of meso-rod	low – relies on activity away from damage site

It was shown in Section 5.2.2 that small changes in the surface of the 'fibre' have a strong effect on the pull-out behaviour. Accordingly, a highly controlled and highly repeatable surface finish is required to attain the shear controlled pseudo-ductility as disclosed in both methods; this is achieved only with multiple manufacturing processes that must themselves be highly controlled and highly repeatable. An alternative solution, broached briefly in Section 5.1.2.5, is to provide an interface between the two sliding surfaces using a third material, one that adheres strongly to both surfaces but itself yields in shear. An example would be polyethylene; the shear strength of any given type of polyethylene is acceptably repeatable

Chapter 8: Conclusions

Both of the two solutions proposed for inducing pseudo-ductility in FRP rebar appear to be promising. A FRP rebar having the strength, stiffness and ductility of steel was not achieved in this work, but the results of various tests and discoveries offer a significant amount of information that should lead to successful replacement of steel rebar. The following sections work assist in furthering the work by summarizing the conclusions from the multiple meso-rod and over-wrap designs as well as the concrete beam testing of over-wrapped reinforcement.

8.1 Multiple Meso-rod Design

- Ductility may be localised allowing for multiple, independent damages sites,
- interfacial shear strength between mating fibre and matrix surfaces is highly variable and reliant on several processing and material factors and thus difficult to predict,
- debond forces are considerably higher than maximum pull-out loads,
- the discontinuous/continuous hybrid strands fracture at the discontinuities leading to frictional loading at the interface,
- the meso-rods themselves do not fracture, and
- the meso-rods may be of considerable length – depending on the interface – allowing for extreme ductility.

8.2 Over-wrap Design

- The strength of the frictional interface between the inner rod and over-wrap is very sensitive to small changes in surface finish of the inner rod and characteristics of the over-wrap,
- a variety of surface finishes and/or over-wrap characteristics may be combined to achieve the same frictional shear stress, and
- the over-wrap should be applied independently of the process for forming the inner rod to avoid negative effects of unexpected changes or interruptions to the curing process.

8.3 Concrete Beam Testing

- The load-deflection behaviour of a beam reinforced with an over-wrapped rod is very similar to a traditionally reinforced beam.
- Interface strength must be high-enough to generate acceptable stiffness in reinforced structures, but also be low enough to allow the inner rod to slip without encroaching on the tensile yield or failure loads of the rod.
- With the correct conditions, total slip distance of the inner rod will be equal to the width of a crack in the damage zone, and
- The manufacturing process for over-wrapped reinforcing rods is simple and may be easily automated and adapted for different reinforcement requirements.

Several recommendations for future research generated from this body of work arise from the above conclusions. These are presented in the following Chapter.

Chapter 9: Recommendations

This work serves as a foundational study on the viability of two approaches to the design and manufacture of FRP reinforcing bars having ductility similar to that of traditional reinforcing steel. The next stage of investigation should involve independent investigations of the two methods. The results of the present investigation give rise to general recommendations on the direction the future research should take.

A discontinuous over-wrap system with a thin intermediate layer between the over-wrap and the inner rod, the outer surface of the rod and inner surface of the over-wrap each being shaped or treated to provide anchoring stronger than the shear strength of the intermediate layer. The intermediate layer may be formed of a thermoplastic layer due to the repeatable material strength of most thermoplastics.

Meso-rods should also be coated with a thin intermediate layer – preferably thermoplastic material – the meso rods having a surface roughened to provide strong anchoring for the thermoplastic layer such that the thermoplastic layer fails in shear. A group of experiments to determine the preferred thickness of the intermediate layer, the surface treatment of the meso-rods, and the effects of matrix curing on the intermediate layer should be designed and performed. Once these have been completed, the physical dimensions – the length and diameter – of the meso-rods may be decided. Additionally, the ratio of maximum debond load to maximum pull-out load should be studied in order to bring them to similar levels. Rods designed with the known interface and meso-rod dimensions may then be manufactured and tested and then compared with the predictive equations for the rebar strength and stiffness. It is possible that the meso-rods will have considerable length resulting in very high levels of pseudo-ductility.

Finally, once effective designs for each of the methods have been completed, the creep and temperature behaviour of the rods should be studied to determine long-term viability of the FRP rebar in loaded and seasonally variable conditions.

The above listed improvements should produce rods that achieve the goal of high pseudo-ductile FRP reinforcement for concrete structures.

References

1. El-Salakaway, E., B. Benmokrane and Gérard Desgagné "Fibre reinforced polymer composite bars for the concrete deck slab of Wotton Bridge" Canadian Journal of Civil Engineering, v 30 (2003) pp 861-870
2. Nystrom, H, et al. "Financial Viability of Fiber-Reinforced Polymer (FRP)Bridges" Journal of Management in Engineering. Vol 19, no. 1 p2-8 (January 2003)
3. Hassanain, Mostafa A and Robert E. Loov, Canadian Journal of Civil Engineering, vol 30, pp 841-849 (2003)
4. Razaqpur, A. G. "Impact of Composites on Construction" Design and manufacturing of Composites, Third Joint Canada-Japan Workshop on Composites, Kyoto, March 2000, pp. 113-120.
5. De la Rosa, Cesar. "Length Effect in Hybrid FRP Rebars for Reinforced Concrete Applications" M. Eng Thesis University of Ottawa Press. Ottawa, ON: (2002) 77 pages.
6. Malvar, L. J., and J. E. Crawford. "Dynamic Increase Factors for Steel Reinforcing Bars" 28th DDESB Seminar. Orlando, FL (1998) 17 pages.
7. Mertz, D. H., et al. "National Cooperative Highway Research Program Report 503: Application of Fiber Reinforced Polymer Composites to the Highway Infrastructure – White Paper No. 5: FRP Composites as Internal Reinforcement of Concrete Components" Transportation Research Board of the National Academies, Washington D.C.: 2003 pp D14-D15
8. CVG 3143 Sample Reinforced Concrete Design Lab Report. March 2004. Unpublished.
9. Stratford T., Burgoyne C. " Shear Analysis of Concrete with brittle reinforcement" , FRPRCS-5 Thomas Telford, London, 2001 pp.939-940
10. Callister, W. "Materials Science and Engineering: An Introduction" 3rd ed. John Wiley & Sons, Inc. Toronto: 1994. pp 554-555.
11. Young, J.F. et al. "The Science and Technology of Civil Engineering Materials" Prentice Hall. Upper Saddle River, NJ: 1998. pp 302-303.
12. Cross, W.M. et al. "Stainless Steel Clad Rebar in Bridge Decks," Study SD2000-04. South Dakota School of Mines & Technology. Rapid City, SD. (2001) 47 pages.

13. Thomas, G. "Low-carbon steels of superior mechanical and corossion properties and process of making thereof." United States Patent US 6,273,968 B1. Issued 14-August-2001.
14. MMFX Steel Corporation of America: Product Bulletin. February 2002.
15. http://www.fhwa.dot.gov/bridge/frp/ibrcweb.htm, December 4, 2003
16. Bogues-Crowe, M. Personal communication, 15-November-2003.
17. Nathan, T. R. and O.U. Onyemelukwe "Comparison of Bridge Deck Alternatives Using Life Cycle Costs" 8th ASCE Specialty Conference on Probabilistic Mechanics and Structural Reliability: 2000. pp 310-316.
18. Bradberry, T. E. , "Concrete Bridge Decks Reinforced with Fiber-Reinforced Polymer Bars," Transportation Research Record 1770, Transportation Research Board, National Research Council, Washington D.C., (2001) pp. 94-104.
19. Saito., M. and K. C. Sinha. "Timing for Bridge Replacement, Rehabilitation and Maintenance," Transportation Research Record 1268, Transportation Research Board, National Research Council, Washington D.C., (1990) pp. 75-83.
20. Busel, John P. "Fiber-Reinforced Polymer (FRP) Composite Dowel Bars...A 15 Year Durability Study" Publication Market Development Alliance of the FRP Composites Industry. Date unknown.
21. http://www.compositesworld.com/ct/issues/2003/April/62
22. American Concrete Institute—Committee 440. Guide for the design and construction of concrete reinforced with FRP rebars, ACI 440.1R-03. Farmington Hills, MI, USA: ACI, 2001.
23. Benmokrane, B. et al. "Mechanical and bond properties of new generation of carbon fibre reinforced polymer reinforcing bars for concrete structures" Canadian Journal of Civil Engineering 29 (2002) 338-343
24. Wang Z., Goto Y., Joh O. " Bond characteristic of FRP rods and effect on long term deflection of concrete beams", Non-metallic (FRP) Reinforcement for Concrete structures, Proceedings of the Third International Symposium, Vol.2, Oct.,1997 pp 389-396
25. Benmokrane, B., Burong Zhang and Adil Chennouf. "Tensile properties and pullout

behaviour of AFRP and CFRP rods for grouted anchor applications" Construction and Building Materials 14 (2000) 157-170

26. Benmokrane, B. et al. "Evaluation of aramid and carbon fibre reinforced polymer composite tendons for prestressed ground anchors." Canadian Journal of Civil Engineering 27 (2000) 1031-1045.
27. Uomoto, T. and T. Nishimura. "Deterioration of Aramid, Glass, and Carbon Fibers Due to Alkali, Acid and Water in Different Temperatures" American Concrete Institute Special Publication SP 188 (2000).
28. Belarbi A., Chandrashekara K., Watkings, S.E., "Performance Evaluation of Fiber Reinforced Polymer Reinforcing Bar Featuring Ductility and Health Monitoring Capability" American Concrete Institute Special Publication SP 188 (2000)
29. Sasaki, I., I. Nishizaki, H. Sakamoto, K. Katawaki and Y. Kawamoto. "Durability Evaluation of FRP Cables by Exposure Tests" Non-Metallic (FRP) Reinforcement for Concrete Structures: Proceedings of the Third International Symposium, 2 (1997). pp 131-137.
30. Kumahara, S., Y. Masuda, and Y. Tanano. "Tensile Strength of Continuous Fiber Bar Under High Temperature" International Symposium on Fiber-Reinforced Plastic Reinforcement for Concrete Structures, SP-138. American Concrete Institute. Farmington Hills, MI. (1993) pp 731-742.
31. Saafi, M. "Effect of fire on FRP reinforced concrete members" Composite Structures v 58 (2003) pp11-20.
32. Takewaka, K., and Khin, M., 1996, "Deterioration of Stress-Rupture of FRP Rods in Alkaline Solution Simulating as Concrete Environment," Advanced Composite Materials in Bridges and Structures, M.M. El-Badry, Ed., Canadian Soc. for Civil Engineering, Montreal, Quebec, pp. 649-664.
33. Neild, S. A., M. S. Williams and P. D. McFadden. "Measurement of low-amplitude hysteresis behaviour of concrete by high-precision vibrating wire strain gauges." Key Engineering Materials Vols. 245-246 (2003) pp 315-322.
34. Belarbi, A. et al. "Smart fiber-reinforced polymer rods featuring improved ductility and

health monitoring capabilities." Smart Material Structures 10 (2001) 427-431

35. Tennyson, R. C. "Structural health monitoring of innovative bridges in Canada with fiber optic sensors." Smart Materials and Structures 10 (2001) 560-573
36. Rizkalla, S. H., A. A. Mufti and G. Tadros "Recent Innovation for Concrete Highway Bridges in Canada" Proceedings: 24nd International SAMPE Symposium May 4-8, 1997 pp 281-287.
37. Dr. M. Saatcioglu. Professor of Civil Engineering, University of Ottawa. Personal communication.
38. Bakis, C.E., Nanni, A. Terosky, J.A., Koehler, S.W., " Self-monitoring, pseudo-ductile, hybrid FRP reinforcement rods for concrete applications" , Composites Science and Technology 61 (2001) pp. 815-823
39. Bunsell, A.R., Harris, B., "Hybrid carbon and glass fibre composites", Composites, 1974 pp 157-164
40. Somboonsong, W., Ko, F.K., and Harris H.G., "Ductile Hybrid Fiber Reinforced Plastic Reinforcing Bar for Concrete Structures: Design Methodology", ACI Materials Journals, 95, No.6, (1998) pp 655-666
41. Tamuzs, V. and R. Tepfers. "Ductility of Nonmetallic Hybrid Fiber Composite Reinforcement for Concrete" Mechanics of Composite Materials 32 No 2 (1996) pp113-121.
42. Manis, Peter Angelo. "Manufacture and performance evaluation of FRP rebar featuring ductility" M.Sc. Thesis. University of Missouri-Rolla (1998) 88 pages.
43. Halpin, J.C. "Revised Primer on Composite Materials: Analysis" Technomic Publishing Co., Inc. Lancaster, PA: 1984. pp 130-145.
44. Pillai, S. U., D. W. Kirk and M. A. Erki. "Reinforced Concrete Design" 3rd ed. McGraw-Hill Ryerson, Toronto: . pp 268-269.
45. Uomoto, T. "Durability of FRP as Reinforcement for Concrete Structures" in Advanced Composite Materials in Bridges and Structures. Humar, J. And A. Razaqpur, eds. Canadian Society for Civil Engineering. Carleton University. Ottawa, ON: 2000. pp. 3-17.

46. http://www.nist.gov/public_affairs/factsheet/ebert2.htm. Accessed 15-March-2003